Application of Particle Image Velocimetry to the Measurement of Non-Linear Effects generated by High-Intensity Acoustic Fields

Dawn Rockliff

A thesis submitted in fulfilment of the requirements

for the degree of Doctor of Philosophy

to the

University of Edinburgh

2002

TO MY FAMILY

Abstract

Non-linear effects are known to occur in high intensity sound fields and have important consequences in the study of a diverse range of applications from medical imaging to musical instruments. Particle Image Velocimetry (PIV) is used to obtain full-field instantaneous velocity information without physical intrusion into the acoustic field. After a review of the theory of PIV, the technique is applied to the investigation of non-linear effects on acoustic streaming in a closed-end cylindrical tube. A distortion of the streaming motion is observed with increasing sound intensity and a comparison to theoretical work is presented. PIV is then used in conjunction with pressure measurements to examine the non-linear behaviour at the termination of an open-ended cylindrical tube. The results are compared to acoustic measurements of the non-linear radiation impedance using conventional techniques. The work is then extended through the introduction of side holes into the open tube. PIV measurements of the streaming motion as a function of frequency and intensity are made and used to draw comparisons with the streaming behaviour present at the tone holes of a modern Boehm flute under normal playing conditions. The results from this work clearly show that PIV has the potential to provide a better understanding of acoustical fields in situations where non-linear effects can have a significant influence, such as that found on musical instruments.

Acknowledgements

I would first like to thank Murray Campbell and Clive Greated, my two supervisors for their help and enthusiasm throughout the course of this study. In addition, I'm also grateful to Joël Gilbert, Ludovic Menguy and Jean-Pierre Dalmont of the research group at the University of Maine in Le Mans, France for their helpful discussions.

I am indebted to Frank Morris, the technician, for his constant help, humour and ability to construct experimental apparatus, no matter how bad the drawing.

I would also like to thank members of the Fluids & Acoustics group for their support, particularly Ted Schlicke for programming advice, David Skulina for assistance with the side hole measurements, and the rest of the gang: Alan, Mark, Jonathan, Tom, Scott, Orlando, Jim, John, Dave, Susan, Alix, Calum, Steven and Sandra for making the last four years enjoyable (and allowing an English lass into their midst).

The financial support of EPSRC is gratefully acknowledged.

A big thank you goes out to Craig & Karen, and many close friends around the country who have given their continual moral support throughout my PhD.

Finally, I would like to thank my Mum and Dad, and my fiancé Julian for their unending support, love and patience throughout my studies. This thesis is dedicated to them.

Contents

List of Figures

List of Tables

List of Symbols and Abbreviations

a	inner tube radius
b	radius of tone hole
c	speed of sound
c_s	propagation speed of sound wave
d	tube diameter
Δd	local displacement vector of tracer particles
d_{diff}	diffraction-limited particle image diameter
d_I	particle image diameter
d_p	seeding particle diameter
$f^{\#}$	numerical aperture of an imaging lens
f^*	pressure gradient force transition frequency
$\mathcal{F}$	Fourier Transform
f_c	cut-off frequency of a tube
I	acoustic intensity
k	wavenumber
L	tube length
M	acoustic Mach number
M_I	image magnification
m_p	mass of the seeding particle
p	sound pressure
p_0	equilibrium pressure in the absence of the sound field
r	radial distance from the tube axis
R	acoustic resistance
$\triangle$R	spacings between PIV grid points on the velocity maps
Re_{nl}	Reynolds number
R_{fg}(x,y)	cross-correlation function

R_p	relative magnitude response of probe microphone
R_r	frequency-dependent constant representing relaxation effects
S	cross-sectional area
Sh	Shear number
Sr_{ac}	Strouhal number
2s	centre-to-centre hole separation
T	period of one acoustic cycle
t	chimney height
t_e	open hole effective length
Δt	time separation between first and second illumination
u	acoustic particle velocity
$\mathbf{u}$	fluid velocity vector
U	volume velocity
u_a	acoustic fluid particle velocity
$\|u_a\|$	acoustic fluid particle velocity amplitude
u_{ac}	acoustic velocity amplitude through tube exit
u_{exit}	mean acoustic velocity amplitude through tube exit
u_p	seeding particle velocity
$\|u_p\|$	seeding particle velocity amplitude
$\mathbf{U}_p$	particle velocity vector
$\angle u_a$	phase angle of the acoustic particle velocity
$\angle u_p$	phase angle of the seeding particle velocity
U_r	acoustic velocity value found at each grid point
u_s	streaming velocity
u_{sr}	radial component of the streaming velocity
u_{sx}	axial component of the streaming velocity
V_p	RMS amplitude of probe output voltage signal
V_r	RMS amplitude of reference microphone output voltage signal
V_{st}	superimposed steady flow velocity
X	acoustic reactance

z	specific acoustic impedance
Z	acoustic impedance
$\|Z\|$	amplitude of acoustic impedance
Z_c	characteristic impedance
z_r	specific radiation impedance
Z_r	Radiation Impedance
$Re(Z_{r\,nl})$	non-linear component of the acoustic resistance
Δz	light sheet thickness

List of Greek symbols

α_p	measured phase of the probe microphone
α_r	measured phase of the reference signal
δ_0	length correction (thin-walled unflanged tube)
δ_∞	length correction (tube with infinite flange)
δ_v	thickness of the viscous boundary layer
δ	internal interaction parameter
ϵ	external interaction parameter
θ	phase change of sound wave on reflection
λ	acoustic wavelength
μ	coefficient of shear viscosity
μ'	coefficient of bulk viscosity
ρ_0	equilibrium fluid density
ρ_p	seeding particle density
ρ_a	fluid density
τ_p	relaxation time of the particle
ϕ_{in}	phase angle of reference signal relative to pulse generator time base
ϕ_p	phase angle of pressure signal
ϕ_{ref}	phase angle of reference signal
ϕ_u	phase angle of velocity signal
ω	angular frequency
$\vec{\omega}$	vorticity of fluid motion

List of abbreviations

A/D	analogue to digital
CCD	Charged Coupled Device
CW	Continuous Wave
DLS	Dynamic Light Scattering
HWA	Hot Wire Anemometry
FT	Fourier Transform
FFT	fast Fourier Transform
IL	Intensity Level
LDA	Laser Doppler Anemometry
LSV	Laser Speckle Velocimetry
mf	mezzo forte
Nd:YAG	Neodymium Yttrium Aluminium Garnet
PC	Personal Computer
PIV	Particle Image Velocimetry
PTV	Particle Tracking Velocimetry
RMS	root mean square
S/N	signal to noise ratio
SPL	Sound Pressure Level
SWR	Standing Wave Ratio

Chapter 1

Introduction

The study of non-linear phenomena in acoustics has been of interest for many years, both on a theoretical and experimental basis. In weakly non-linear situations, conventional acoustic relationships adequately describe the acoustic behaviour. However, in the presence of high intensity acoustic fields non-linear effects become more significant, and this basic linear approach is no longer sufficient. Non-linear phenomena play an important role in a diverse range of practical situations, ranging from aero-acoustics to medical imaging and the study of woodwind instruments.

This work considers phenomena related to the last of these applications. Normal playing pressures within woodwind instruments are sufficiently high to produce significant non-linear effects. These have been correlated with the generation of higher harmonics and a change in the timbre produced by the instrument.

The difficulty in studying non-linear effects is that although their magnitude can be significant, it is small in relation of that of the acoustic velocity field. The use of intrusive measurement techniques such as those with probe microphones will disturb the sound field and distort the flow. For this reason, the

method of Particle Image Velocimetry (PIV) was chosen, whereby not only can the non-linear effects be investigated non-intrusively, but both quantitative and qualitative information about the acoustic field can also be obtained.

PIV is a well established technique for obtaining full-field instantaneous velocity measurements. The fluid is seeded with small particles and illuminated with a pulsed light source. Light scattered by each particle in the illuminated plane is then captured by a camera, and the resulting images analysed to determine the particle velocity. A more detailed description of PIV is given in chapter 3.

Previous PIV studies have investigated both the acoustic particle velocity and the slower mean motion of acoustic streaming [8, 45, 91] which results from the viscous interaction between the sound field and a solid boundary. These studies were performed using a conventional camera with wet film; while this provides a high resolution, it results in a lengthy analysis process. The introduction of a digital camera, although having a lower spatial resolution than wet film, provides a significantly higher acquisition rate and quicker analysis.

Although PIV is a widely used technique, it has had very little application to the study of acoustic fields. In particular, PIV has not been used to investigate non-linear effects induced by high intensity fields at the tone holes of a musical instrument.

1.1 Aim and contents of thesis

The work described in this thesis has several objectives which concern the application of the velocity measurement technique of PIV to acoustic fields. These objectives are:

1. to verify the suitability of PIV to investigating both the oscillatory acoustic velocity, and the mean streaming motion resulting from interaction of the acoustic field with a solid boundary.

2. to demonstrate that this technique is capable of measuring small scale non-linear effects induced by high-intensity sound fields in a closed tube, and to compare the measured behaviour with existing theoretical predictions.

3. to examine the acoustic behaviour at tube terminations, and establish the non-linear effects present in this configuration.

4. to qualitatively examine the streaming motion at side holes under realistic playing conditions.

This thesis is split into two parts. The first part, consisting of chapters 2, 3 and 4 firstly lays the foundation of the work, discussing basic acoustic theory, before introducing PIV and the specific experimental configurations used in subsequent chapters. The second part of the thesis (chapters 5, 6 and 7) then presents the experimental methods and results, starting with measurements in a simple closed system, and ultimately extending this to an open tube with multiple side holes.

Chapter 2 begins by introducing some basic acoustic parameters used in this study, before developing relationships for a standing wave in both a closed and

open-ended tube configuration such as those used for this study.

In chapter 3, the basic principle of PIV is outlined. This is then followed by a detailed discussion of the technique, including methods for optimising the various parameters and reducing errors.

Chapter 4 describes the three different PIV configurations used in this study, with a discussion of the procedures and limitations associated with each one. Preliminary calibration measurements are presented together with an examination of the effect of microphone orientation. The response of the different seeding particles with respect to the theoretical flow velocity is also considered.

Chapter 5 examines the influence of high intensity fields on acoustic streaming motion in a closed-end tube. The chapter starts by reviewing existing theoretical and experimental work. Experimental results from acoustic streaming measurements are then compared to theoretical models. This comparison identifies a number of differences. Several alterations made to the experimental method in an effort to ascertain the source of these discrepancies are discussed in detail.

Chapter 6 investigates the non-linear acoustical behaviour at the exit of an open-ended tube with increasing sound intensity. A technique to obtain the acoustic impedance using PIV in conjunction with pressure measurements is presented, and initially validated by measurements in a simple acoustic system. Then, using a similar experimental configuration to previous authors, the acoustic resistance is measured as a function of sound intensity at the tube exit and the results compared with existing data. Finally, the PIV velocity maps are processed further to examine the vorticity at the tube end. This demonstrates the versatility of PIV in obtaining further acoustical parameters.

This work is then extended in chapter 7, with the introduction of side holes in the open tube. Qualitative PIV measurements are taken to investigate the acoustic streaming at each hole, and the inter-hole interaction at high intensities. Comparisons are drawn with a modern Boehm flute to illustrate one application of this work.

Finally, in chapter 8, the main conclusions of the study are summarised, and recommendations for further work are made.

Chapter 2

Acoustic field characteristics

The aim of this chapter is to define some of the basic equations which describe acoustic fields and parameters taken in experimental measurements.

2.1 Introduction

The study of acoustic fields is generally concerned with the generation and propagation of waves through a medium. A sound wave is generated when a surface is set into vibration, disturbing local fluid particles and causing them to oscillate back and forth about a mean position. The sound wave then propagates through the fluid by transferring kinetic energy from one particle to the next.

A complete definition of the acoustic field requires knowledge of the spatial and temporal dependence of at least two acoustic variables such as pressure (p), density (ρ) or acoustic velocity (u): usually pressure and velocity are chosen. Sound pressure levels can easily be measured using a microphone, which is a reliable device and highly accurate. However, at high intensity acoustic levels, the presence of a microphone in an acoustic field can severely distort the field in the

near vicinity, hence affecting the reliability of the measurement. This is discussed further in section 4.6. Accurate velocity measurements are harder to record; a sound field causes fluid particles to oscillate with acoustic velocity u, whose amplitude at high intensities can be very large and hence difficult to measure. A number of methods have been successfully used to measure acoustic field velocities over the last few years. These include direct measurement techniques such as using Rayleigh Discs and Hot Wire anemometers, as well as more recent indirect measurement techniques using lasers, such as Laser Doppler Anemometry (LDA) and Particle Image Velocimetry (PIV). These are discussed in Chapter 3.

This study is primarily concerned with the investigation of acoustic fields in and around cylindrical tubes; this is achieved by measuring the pressure and acoustic velocity. Two acoustic parameters of importance in this situation are the acoustic intensity and impedance.

2.1.1 Acoustic intensity

The acoustic intensity, which quantifies the average rate of energy transmitted through a unit area, is defined as:

$$I = < p\,u >_t = \frac{1}{T}\int_0^T pu\,dt, \tag{2.1}$$

where the integral is evaluated over the time taken for one complete acoustic cycle.

For a plane wave propagating in the positive x direction, the sound pressure and acoustic velocity (both taken as RMS quantities) are related by

$p_{rms} = \rho_0 c u_{rms}$, where ρ_0 is the fluid density and c is the speed of sound. Hence:

$$I = \frac{p_{rms}^2}{\rho_0 c}. \tag{2.2}$$

Conventionally, intensity and pressure measurements are compared to a reference signal and expressed using a logarithmic scale due to the large range of values encountered in acoustics. For sound intensity levels, measured in decibels (dB),

$$\text{Intensity Level } \mathbf{IL} \text{ (dB)} = 10 \log \left(\frac{I}{I_{ref}} \right), \tag{2.3}$$

where the reference intensity I_{ref} for air is usually given as $10^{-12} \mathrm{W\,m^{-2}}$, corresponding approximately to the threshold of human hearing at a frequency of 1kHz. Hence, using the relationship between intensity and pressure in equation 2.2, the sound pressure level can be expressed as:

$$\text{Sound Pressure Level } \mathbf{SPL} \text{ (dB)} = 20 \log \left(\frac{p_{rms}}{p_{ref}} \right), \tag{2.4}$$

where the reference pressure p_{ref} is defined as 20μPa.

2.1.2 Impedance

Another important acoustical quantity is the specific acoustic impedance, z, defined as the ratio of acoustic pressure to acoustic particle velocity

$$z = \frac{p}{u}. \tag{2.5}$$

For a propagating plane wave, the pressure and velocity are in phase, giving

$$z = \pm \rho_0 c, \tag{2.6}$$

where z is positive and negative for positively and negatively propagating waves respectively, and $\rho_0 c$ is the characteristic impedance of the medium. The characteristic impedance of air at standard temperature and pressure, assuming ρ_{air}=1.21 $\mathrm{Kg\,m^{-3}}$ and c=343 $\mathrm{m\,s^{-1}}$, is $\rho_0 c$=415 $\mathrm{Pa\,s\,m^{-1}}$.

When considering the interaction of sound waves at the interface between two dissimilar media or volumes of differing size, for example at the open end of a pipe, it is more conventional to consider the acoustic impedance Z, described as the pressure at a surface of a cross-sectional area S divided by the volume velocity at the surface:

$$Z = \frac{p}{U}, \tag{2.7}$$

also expressed as

$$Z = |Z| e^{i\phi}, \tag{2.8}$$

where $|Z|$ is the impedance amplitude, ϕ is the phase difference between the pressure and acoustic velocity, and the volume velocity U is $S \times u$. The concept of impedance refers to the relationship between the pressure and acoustic velocity at a specific frequency, i.e. for a particular harmonic component of both the pressure and velocity signals.

2.1.3 Relationship between acoustic pressure and velocity

For a plane wave in air, the RMS pressure and RMS acoustic particle velocity are related by p_{rms}=zu_{rms}. Substituting this into equation 2.4 with z=415Pa s m^{-1} and p_{ref}=20μPa gives:

$$\mathrm{SPL} = 20\log\left(\frac{415.u_{rms}}{20\times10^{-6}}\right) \tag{2.9}$$

and therefore

$$u_{rms} = \frac{20\times10^{-6}}{415}10^{\frac{SPL}{20}}. \tag{2.10}$$

As the acoustic velocity amplitude $|u_a|$ and u_{rms} are related through $|u_a|$=$\sqrt{2}$u$_{rms}$, $|u_a|$ can then be written

$$|u_a| = 0.0682\times10^{0.05SPL-6}. \tag{2.11}$$

Hence, it is possible to establish the amplitude of the acoustic particle velocity from pressure measurements or vice versa. Once $|u_a|$ is known, the acoustic particle velocity at a point x in the sound field can be found using the relationship:

$$u(x,t) = |u_a|\sin\left(\frac{2\pi x}{\lambda} - \omega t + \phi\right), \tag{2.12}$$

where λ is the acoustic wavelength, ω is the angular frequency and ϕ is the phase angle.

Although the previous equations have been derived assuming the sound field is a progressive plane wave and therefore the pressure and acoustic velocity are

in phase, the equations can be applied to more complex acoustic fields provided the phase relationship between the pressure and velocity is known.

2.2 Theory of acoustic waves in tubes

2.2.1 Standing wave in a closed-end tube

In the case where a transmitted wave is partially or wholly reflected back, a standing wave is formed due to interference of the transmitted and reflected waves [60]. Consider an air-filled tube of internal radius a and length L, acoustically excited at x=L by a loudspeaker and terminated at x=0 by a semi-rigid metal plate, as illustrated in figure 2.1. When driven by a sinusoidal input voltage, the loudspeaker generates an acoustic wave of angular frequency ω which propagates as a plane wave along the tube towards $x = 0$.

Assuming that any attenuation during propagation is negligibly small, the incident pressure wave takes the form

$$p_i = Ae^{j(\omega t+kx)} \tag{2.13}$$

with amplitude A and wavenumber k, where k=ω/c. Upon reflection at $x = 0$, the wave undergoes a small phase change θ and propagates back towards the loudspeaker with attenuated amplitude B described by

$$p_r = Be^{j(\omega t-kx+\theta)}. \tag{2.14}$$

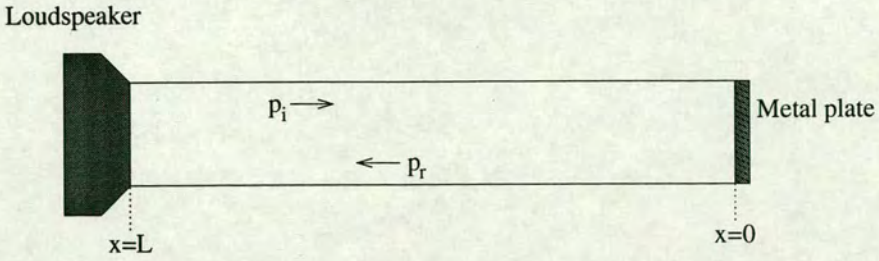

Figure 2.1: Loudspeaker-tube configuration.

It is clear from equations 2.5 and 2.6 that the incident and reflected acoustic velocity waves u_i and u_r respectively are

$$u_i = \frac{p_i}{\rho c} \tag{2.15}$$

$$u_r = \frac{-p_r}{\rho c}. \tag{2.16}$$

The interference of the incident and reflected waves results in the formation of a standing wave in the tube. The relationship between the pressure and acoustic velocity can be established by considering the interaction between the incident and reflected waves.

The total sound pressure at position x along the tube is given by the sum of the incident and reflected waves:

$$p(x,t) = p_i + p_r \tag{2.17}$$

$$= e^{j(\omega t+\theta/2)}\left[Ae^{j(kx-\theta/2)} + Be^{-j(kx-\theta/2)}\right] \tag{2.18}$$

$$= e^{j(\omega t+\theta/2)}\left[(A+B)\cos(kx-\theta/2) + j(A-B)\sin(kx-\theta/2)\right] \tag{2.19}$$

$$= (A+B)e^{j(\omega t+\theta/2)}\left[\cos(kx-\theta/2) + \frac{j}{SWR}\sin(kx-\theta/2)\right], \tag{2.20}$$

where the standing wave ratio SWR, defined as the ratio of pressure amplitudes

at the pressure antinode to node is

$$SWR = \frac{A+B}{A-B}. \tag{2.21}$$

The corresponding expression for the total acoustic velocity at position x is

$$\begin{aligned} u(x,t) &= \frac{1}{\rho c}(p_i - p_r) && (2.22) \\ &= \frac{(A+B)}{\rho c} e^{j(\omega t+\theta/2)} \left[\frac{1}{SWR}\cos(kx-\theta/2) + j\sin(kx-\theta/2)\right] && (2.23) \end{aligned}$$

From equation 2.20 and equation 2.23, the amplitudes of the pressure wave and acoustic velocity wave are, respectively:

$$\begin{aligned} |p(x)| &= (A+B)\sqrt{\cos^2(kx-\theta/2) + \frac{1}{SWR^2}\sin^2(kx-\theta/2)} && (2.24) \\ |u(x)| &= \frac{(A+B)}{\rho c}\sqrt{\frac{1}{SWR^2}\cos^2(kx-\theta/2) + \sin^2(kx-\theta/2)}. && (2.25) \end{aligned}$$

From equations 2.24 and 2.25, when $kx - \theta/2 = n\pi$ where $n = 0, 1, 2, \ldots$, the pressure amplitude is at a maximum and the acoustic velocity at a minimum. Conversely, when $kx - \theta/2 = (n + 1/2)\pi$, the velocity amplitude is a maximum and the pressure a minimum. The pressure and acoustic velocity are shifted in phase with respect to time by $\pi/2$ from each other. If the termination at $x = 0$ is rigid, the velocity is zero and the pressure is a maximum. The first pressure node occurs at position $x = \lambda/4$, where λ is the acoustic wavelength, with subsequent antinodes and nodes displaced at intervals of $\lambda/4$ from the end. The positions of the velocity nodes and antinodes are displaced by $\lambda/4$ with respect to those of the pressure, as illustrated in figure 2.2(a).

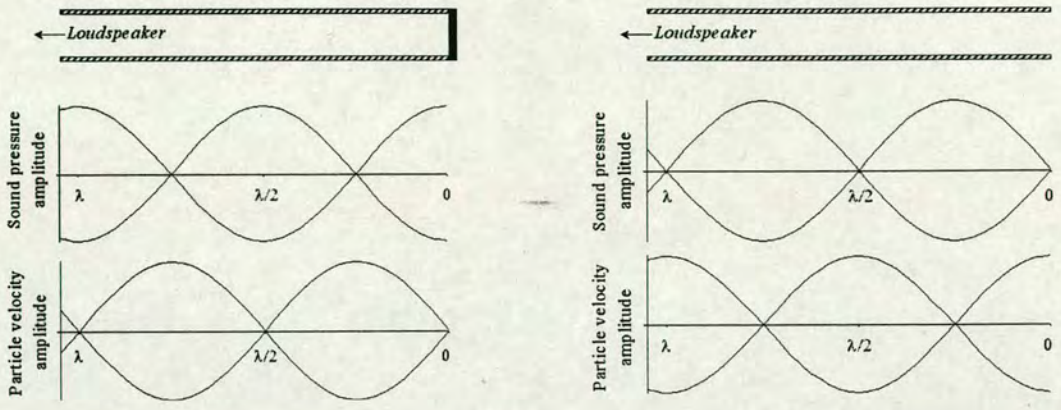

(a) (b)

Figure 2.2: Amplitudes of the acoustic pressure and particle velocity as a function of distance from the end of the tube opposite the loudspeaker for a standing wave in (a) a closed-end tube and (b) an open-end tube.

2.2.2 Standing wave in an open-ended tube

Consider a similar air-filled tube of length L but with an open end at x=0 terminated by impedance Z_0. When the propagating wave reaches x=0, the change in acoustic conditions results in part of the wave leaving the tube as radiated sound and the remaining part being reflected along the pipe, where the amount of wave energy reflected depends on the ratio of the wavelength, λ, to the diameter of the tube, d. When the ratio λ/d is large ($ka \ll 1$), the wave is diffracted from the end (as a spherical wave) resulting in a substantial change in acoustic conditions and hence reflection of most of the wave energy back into the tube. When λ/d is small ($ka > 2$), the acoustic conditions outside and inside the tube remain fairly similar and hence most of the wave energy is transmitted out of the tube into the surrounding medium [18].

For the case $ka \ll 1$, which is of main relevance in this study, $Z_0 \ll Z_c$, (where Z_c is the characteristic impedance) and hence the pressure at the tube termination will be very small. Assuming the ideal case where Z_0=0, there will be a pressure node at the tube termination. Hence, from equations 2.24 and 2.25, the velocity and pressure are still $\pi/2$ out of phase (with respect to time) from each other, but with a velocity antinode and pressure node at x=0 as illustrated in figure 2.2(b). However, in the physical case of an open pipe, the acoustic impedance at the open end of the pipe will always have some finite value due to acoustic motion just outside the tube, which can be compensated for by adding a length correction to the tube. As will be described in section 6.1.1, this means that the effective end of the tube, and hence the position of the pressure node, lies outside the tube at a distance of $\approx 0.61a$ for an unflanged tube ($\approx 0.82a$ for a flanged tube).

Using equations 2.13, 2.14, 2.17 and 2.22, the specific acoustic impedance at a distance x from the open end of the tube is:

$$
\begin{aligned}
z(x) &= \rho c \frac{p_i + p_r}{p_i - p_r} && (2.26)\\
&= \rho c \frac{A e^{jkx} + B e^{j\theta} e^{-jkx}}{A e^{jkx} - B e^{j\theta} e^{-jkx}} && (2.27)\\
&= \rho c \frac{(A + B e^{j\theta}) \cos kx + j(A - B e^{j\theta}) \sin kx}{(A - B e^{j\theta}) \cos kx + j(A + B e^{j\theta}) \sin kx} && (2.28)\\
&= \frac{z_r + j\rho c \tan kx}{1 + j(z_r/\rho c) \tan kx}, && (2.29)
\end{aligned}
$$

where the specific radiation impedance of the tube termination is

$$
z_r = \rho c \frac{A + B e^{j\theta}}{A - B e^{j\theta}}. \qquad (2.30)
$$

In order to obtain the acoustic impedance, it is then only necessary to divide the specific acoustic impedance by the cross-sectional area of the pipe.

2.3 Attenuation in a tube

In the previous sections, it has been assumed that the walls of the tube are rigid, perfectly smooth and thermally insulating, such that attenuation of the propagating wave can be ignored. However, it is well known that fluid flow adjacent to a solid boundary will suffer attenuation due to interactions between the fluid and the boundary [97]. In the case of sound waves propagating along a tube, acoustic energy is dissipated in a region close to the walls, mainly due to viscous forces and heat conduction [13, 40, 60]. The dissipation is confined to a boundary layer next to the walls, outside of which the sound wave propagates as a plane wave. The thickness of the viscous boundary layer is given by

$$\delta_v = \left(\frac{\mu}{\omega\rho}\right)^{1/2}, \tag{2.31}$$

with coefficient of viscosity μ. From equation 2.31, boundary layer effects dominate at very low frequencies, and their significance therefore depends on the frequency of excitation and ratio of their thickness to the tube radius. For an air-filled tube at standard temperature and pressure, with viscosity $\mu = 1.81\times\ 10^{-5}$ Pa s and density ρ =1.21 Kg m^{-3}, the boundary layer thickness at a frequency of 100 Hz is 0.15mm. Hence, for a typical air-filled tube used in this study of radius a=10mm, attenuation due to wall effects can be assumed negligible for frequencies above f_{min} =250 Hz, when the boundary layer thickness is less than

1% of the tube radius. An upper limit on the frequency for plane-wave propagation is defined by the cut-off frequency of the tube, above which higher mode propagation occurs [60]. This takes the value f_c=10.1 kHz. Hence, for this study, lossless plane wave propagation can be assumed providing frequencies within the range 250 Hz< f <10.1 kHz are used.

A specific case when the presence of the boundary layer becomes significant is when high intensity sound fields are present. The dissipation of the acoustic wave in the boundary layer generates a non-zero mean motion called acoustic (Rayleigh) streaming [64]. This effect is discussed in more detail in chapter 5.

2.4 Non-linearity

At low sound intensity levels, when the acoustic variables p, ρ and u are considered small in comparison with the equilibrium pressure, density and speed of sound respectively, a propagating sound wave can be treated using a linear approach. However, this linear acoustic approximation is not valid for high intensity sound fields. It therefore becomes necessary to consider first and second-order terms to obtain an adequate description of the acoustic behaviour. Examples of non-linear phenomena include shock waves, which result from the progressive deformation of a propagating acoustic wave, cavitation, when gas bubbles form in a liquid, and the formation of ultrasonic fountains [70].

This study considers two well known phenomena concerned with nonlinear acoustics;

1. **Acoustic streaming** : a mean streaming motion caused by viscous interaction between the sound wave and a solid boundary. This occurs in addition to the oscillatory motion of the acoustic wave.

2. **Vortex shedding and jet formation** : these effects typically occur at the open end of a cylindrical tube where the flow separates, resulting in distortion of the acoustic field around the tube exit.

At the sound intensities considered in this work, the non-linear distortion is generally small. It is therefore imperative that a suitable method is chosen to observe and measure the non-linear phenomena and resulting effects without disturbing the acoustic flow in any way. One such method, chosen for this study, is the non-intrusive method of Particle Image Velocimetry. This technique is described in the next chapter.

Chapter 3

Particle Image Velocimetry

3.1 Introduction

The ability to obtain qualitative and quantitative information about the motion of a fluid, particularly in the case of complex flow situations where fine spatial structures are present, is an important issue in fluid mechanics and other scientific and engineering fields. Early visualization techniques such as particle-tracking velocimetry (PTV) and laser speckle velocimetry (LSV), which use small tracer particles in the fluid to visualize the flow, mainly provide qualitative information about the nature of the motion. Quantitative measurements of the flow can be obtained by flow measuring devices such as the Pitot tube and Hot-Wire Anemometer (HWA). Such devices provide highly accurate velocity information with good spatial resolution at a single point in the flow, but with the disadvantage that the intrusion of the probe into the field disturbs the flow.

The introduction of the laser in the 1960's enabled the development of optical techniques for both the visualization and measurement of flow fields without physical intrusion into the flow. Laser Doppler Anemometry (LDA), a non-intrusive

single-point measuring technique, allows highly accurate measurement of the velocity at a given point in the flow. Particle Image Velocimetry is a non-intrusive technique for the simultaneous measurement of flow velocities at many points in a plane of a fluid. Unlike flow-measuring techniques such as HWA and LDA, it captures whole velocity fields effectively instantaneously, allowing both large and small scale spatial structures to be detected; this is particularly valuable in the study of unsteady flows. PIV has previously been used to measure the oscillating particle velocities and steady flows generated by acoustic fields [47, 91].

The work described in this thesis is concerned with the use of PIV to investigate acoustic fields. In this chapter, following a brief review of alternative measurement techniques for measuring acoustic velocities, the principle of PIV is discussed, focusing specifically on aspects of the technique which are relevant to this study.

3.2 Alternative measuring techniques

In addition to PIV, a number of other techniques have been successfully used to measure velocities in acoustic fields, either directly or indirectly. Direct methods, which often require probes suspended in the flow, include older devices such as the Rayleigh Disc and Hot Wire Anemometers, as well as the 'Microflown', a new acoustic particle velocity sensor developed by van der Eerden et al. [100]. Indirect techniques include the two-microphone method, whereby velocities are inferred from pressure measurements assuming a simple relationship between the pressure and velocity, and more commonly used optical techniques such as LDA.

3.2.1 Direct methods

The oldest direct technique for measuring particle velocities involves the Rayleigh Disc [86], a thin disc of typical diameter $\sim$ 1cm. When the disc is suspended in a sound field, the action of the field exerts a torque on it with magnitude proportional to the mean square of the acoustic particle velocity. The device, which cannot measure flow direction, is difficult to use and requires numerous corrections due to, for example, diffraction effects [84]. The size of the disc can also produce significant distortion in the sound field, making it an unpopular choice of measurement technique.

The Hot Wire Anemometer (HWA) is a well-established device for the measurement of velocity and temperature fluctuations in fluid flows, which has been successfully used to measure acoustic particle velocities in a trombone by Pratt et al. [80]. The hot wire probe consists of a sensor, in the form of a piece of wire typically 1mm long and of diameter 5μm soldered to the tips of two support needles. An electronic control unit, containing a Wheatstone bridge circuit, feeds a heating current to the wire which then acts as one of the arms of the bridge. When placed in a fluid flow, the sensor is convection cooled by the passing fluid, unbalancing the bridge. The feedback amplifier brings the bridge back into balance by increasing the current to the wire. The fluid velocity, which is proportional to the resulting voltage difference across the bridge, can then be found. Compared to optical techniques such as LDA and PIV, the HWA is a very cheap method for obtaining highly accurate velocity measurements without the requirements of transparent containers surrounding the flow or measurement involving seeding particles. However, the device requires calibration, and the

intrusion of the probe will inevitably affect the flow to some degree. Also, the direction of the flow cannot be ascertained unless two or more probes are present in the flow.

The Microflown is a specific sensor for the measurement of particle velocities. It consists of two parallel silicon sensors of length 0.8mm, placed 40μm apart, which are heated by a DC current [100]. When placed in an acoustic field, the air flow causes conduction of heat from the first sensor to the second sensor. This results in a temperature difference, and hence a difference in resistance, between the two sensors. The differential resistance, which can be measured using a specifically designed electronic circuit, is proportional to the fluid velocity provided the sound level does not exceed 135dB. The device can determine the direction of the flow but, like the HWA, intrudes on the flow. It also has an upper velocity limit lower than those considered in this study.

3.2.2 Indirect methods

The velocity can be indirectly measured using the two-microphone method, whereby two closely spaced microphones are used to estimate the pressure gradient in a sound field. Using equations of motion to relate the pressure and velocity for the sound field, the velocity can then be inferred [38]. This technique is frequently extended to the direct measurement of impedance and absorption [21]. Like many of the direct measurement methods, this technique is difficult to calibrate and requires numerous corrections. The presence of microphones in the field can also distort the field being investigated.

An increasingly popular alternative is to use non-intrusive optical techniques such as Laser Doppler Anemometry. In LDA, the fluid velocity at a specific point in a flow field is ascertained from light scattered by particles suspended in the flow. When a moving particle crosses a plane wave light beam in the flow, it scatters light with a frequency shifted proportional to the velocity of the particle. Hence, by measuring the Doppler frequency shift, the velocity can be obtained.

One of the most commonly used LDA configurations is the dual beam system. In this particular system, two parallel light beams are focused at a point, forming interference fringes. As the particle crosses this region, it scatters light from the two beams with slightly different frequencies. The scattered light then combines at the surface of a detector, producing a signal with a number of frequency terms from which the Doppler frequency and hence the particle velocity can be obtained [32]. The main disadvantage with LDA is its restriction to single point measurement. These point measurements can be repeated over an area of the flow field to build up a velocity profile, but this process is time-consuming and therefore not suitable unless the flow field is steady state. In particular, this means that it is not suitable for extracting information about temporally varying structures in the flow.

3.3 Principle of PIV

PIV is a well-established method for determining instantaneous full-field velocity maps of a flow. The velocity field of a region of fluid flow is obtained without disturbing the flow by recording the displacements of seeding particles suspended in and moving with the flow. The technique comprises two sections, *image ac-*

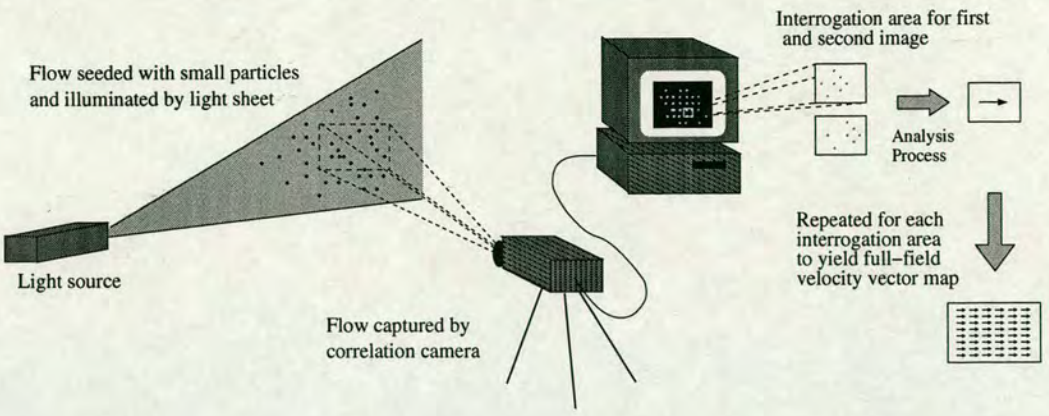

Figure 3.1: Process for obtaining a PIV velocity vector map.

quisition and *image analysis.* In a typical experimental set-up, as illustrated in figure 3.1, the fluid is seeded with small tracer particles and a thin light sheet is projected through the flow which illuminates a plane at a specific region of interest twice in a short time interval Δt. Light scattered by each particle in the illuminated plane at times t and $t + \Delta t$ is imaged by a digital cross-correlation camera placed perpendicular to the light sheet, and recorded on two separate frames. Once all the data has been acquired, the images are analysed to produce a 2-D map of velocity vectors. To achieve this, each image is divided into a grid of smaller areas known as *interrogation areas.* Using the statistical methods of auto or cross-correlation, the local displacement vector Δd of the tracer particles in each interrogation area is separately calculated. Knowing the magnification of the image, M_I, and the time separation Δt between the first and second illumination, the corresponding velocity vector is obtained by the relation:

$$\mathbf{U}_p = M_I \frac{\Delta d}{\Delta t}. \tag{3.1}$$

The procedure is repeated over the entire image to give a velocity vector map of the fluid motion. Once the initial velocity map has been obtained, the information

can be used to calculate other flow quantities such as vorticity, shear rate and kinetic energy.

The technique of PIV is well-documented in numerous journal papers, textbooks and theses. Reviews of the development of particle-imaging techniques are given by Lauterborn and Vogel [61], and Adrian [2]. A more comprehensive guide to PIV can be found in two specific textbooks on PIV by Raffel et al. [83] and Westerweel [104]. A number of prominent papers on PIV, covering all aspects of the technique from development through to the methods of analysis and applications of the technique, can also be found in a special collection edited by Grant [34].

Over the last few years, technological advances in computational and image acquisition disciplines have aided the rapid development of PIV into a successful and extremely versatile flow measurement technique. The implementation of digital image acquisition and analysis techniques [27, 104], now commonplace in most PIV systems, has substantially reduced image processing times and increased the range of velocities and flow regimes which can be measured. This has undoubtedly contributed to the continuing success and wide-spread use of the technique. PIV has been applied to a wide range of flows from water wave motion to aeroacoustics, medical imaging and, most recently, to the field of acoustics and the measurement of sound fields [17]. PIV has been used successfully to measure acoustic particle velocities [31, 45, 46, 47] and the slower mean flows of acoustic streaming [8, 91]. Using a stereoscopic approach, Arroyo and Greated [8] modified the standard PIV set-up to measure all three components of the acoustic streaming velocity, hence demonstrating the possibilities for the investigation of three dimensional flows using PIV. Other 3-D PIV techniques, such as Dual

plane and Holographic PIV, exist which have been applied particularly to the investigation of turbulent flows [49]. Further details of these three techniques can be found in [83].

In the following sections, the two components of the technique, image acquisition and image analysis, are described.

3.4 Image acquisition

As mentioned in section 3.3, in contrast to the flow measuring techniques such as hot-wire anemometry and Rayleigh Discs, which intrude on the flow being investigated, PIV provides a non-intrusive measurement of the fluid motion by recording the movement of tracer particles in the flow. In order to produce images which represent the flow to a high degree of accuracy, careful consideration must be given to the method of illuminating the flow, the choice of seeding particles and the medium for recording the images.

3.4.1 Flow illumination

The choice of light source and method for illuminating the flow depends largely on the velocity range and size of the area under investigation. In order to produce accurate results, PIV requires that the seeding particles do not move a significant distance during an illumination pulse so that the particle images are sharp and individually resolvable. Also, the particles must scatter sufficient light to be detected by the recording medium. Thus, a light source which can deliver short bursts of very intense light is required. Although a variety of light sources have

been used in PIV [83], lasers offer high energy pulses and ease of beam manipulation to illuminate areas of varying sizes, thus making them the obvious choice. Typically, either a pulsed laser system or a continuous wave (CW) laser pulsed by a mechanical shutter or scanning beam system are used [93].

Pulsed lasers

Pulsed lasers, such as the Nd:YAG or Copper Vapour laser, generate very short pulses of light at a high repetition rate. Hence, they are primarily used for capturing high-speed flows ranging from a few metres per second to supersonic flows of $\sim$ $600\mathrm{m\,s^{-1}}$ or greater, where the pulse duration is short enough to effectively freeze the motion of the particles. Pulsed lasers are required to investigate acoustic particle velocities which, for the range of frequencies and sound intensity levels used in this study, give velocities in the magnitude of $0.1\text{-}10\mathrm{m\,s^{-1}}$. As will be described in chapter 5, for a pulsed laser of fixed repetition rate, careful choice of frequency allows the investigation of acoustic particle velocities at specific points within an acoustic cycle. In a typical pulsed laser system, the beam is directed through a combination of lenses to adjust the beam diameter, finally passing through a cylindrical lens which expands the beam in one direction into a thin light sheet of thickness Δz [83], as shown in figure 3.2. The main problem with this method of illumination is the reduction in light intensity due to the distribution of light across the width of the light sheet, restricting its application to relatively small areas. In addition, the laser beam has a Gaussian profile which, when expanded, produces a variation in intensity across the light sheet. In particular, this can result in loss of data at the edges of the images because of insufficient illumination.

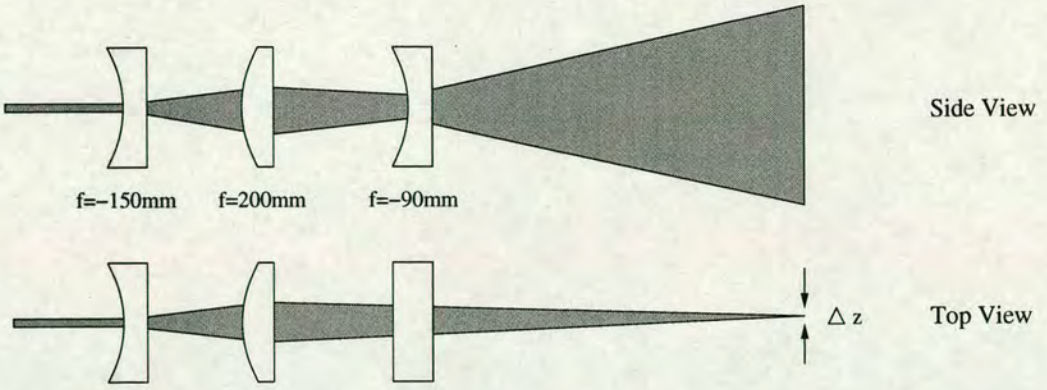

Figure 3.2: Conventional optical configuration for focusing and expanding a pulsed laser beam. The focal lengths given correspond to the optics used for the Nd:YAG laser described in section 4.3.1.

Continuous Wave lasers

For the investigation of acoustic streaming (detailed in Chapter 5) and other slow flows ranging up to about $1\,\mathrm{m\,s^{-1}}$, it is sufficient to use a Continuous Wave (CW) laser in conjunction with an external pulsing or shutter system. For investigating small areas, of the order of a few square centimetres, the laser beam can be pulsed using a mechanical shutter prior to being optically expanded into a light sheet (as for the pulsed laser). Alternatively, either a mechanical shutter can be placed in front of the camera, which requires working in a completely dark environment to ensure pairs of exposures of equal intensity, or a high speed camera can be employed. For larger areas, a scanning beam illumination system is more appropriate. The technique uses a multi-sided rotating mirror to form the laser beam into a pseudo light sheet, sweeping the light across a large area with a repetition rate proportional to the rate of rotation of the mirror. Hence, it produces light sheets of uniform intensity with very efficient use of the laser power, but has a limited repetition rate due to the rotation speed of the mirror. This system, which was developed at Edinburgh University by Gray [42], is used extensively to study waves in water [35, 90].

3.4.2 Seeding particles

As discussed in section 3.3, PIV ascertains velocity information about a flow from seeding particles suspended in the fluid rather than by direct measurement of the fluid itself. Hence, the accuracy of the flow field measurements is limited by the ability of the particles to follow the flow faithfully [67]. This depends on a number of parameters, including the particle size, shape, density and concentration.

Fluid mechanical properties of tracer particles

In air, the unavoidable difference in densities between the seeding particles and the fluid particles in the surrounding medium can result in a delayed response to any acceleration in the fluid. Hence, it is necessary to establish how well the motion of the tracer particles represents the fluid motion.

Consider a seeding particle of diameter d_p and density ρ_p suspended in a sinusoidal acoustic field with acoustic fluid particle velocity u_a and frequency f. The particle is acted upon by two main forces: a Stokes viscous drag force, and a pressure gradient associated with the acceleration of the fluid immediately surrounding it. Vignola et al. [101] derived a model for the motion of tracer particles suspended in an acoustic field, including the effects due to both the viscous drag and pressure gradient forces. Assuming the particles are spherical, the equation of motion for each particle can be written as [32]:

$$\frac{\pi}{6}d_p^3\rho_p\frac{du_p}{dt} = -3\pi\mu d_p(u_p - u_a) + \frac{\pi}{6}d_p^3\rho_a\frac{du_a}{dt}, \tag{3.2}$$

where u_p is the seeding particle velocity, ρ_a is the fluid density, μ is the viscosity of the fluid, and the mass of the particle is $m_p = (\pi/6)d_p^3\rho_p$. The second and

third terms in equation 3.2 represent the viscous drag force and pressure gradient force respectively. Vignola et al. [101] found that at low frequencies, the force exerted by the pressure gradient is very small and the resulting particle response follows the fluid motion very closely. At frequencies above a transition frequency $f^* = 1/(2\pi\tau_p)$, the pressure gradient force dominates resulting in a decrease of particle displacement amplitude relative to the fluid displacement, where τ_p, the relaxation time of the particle, is given by

$$\tau_p = \frac{d_p^2 \rho_p}{18\mu}. \tag{3.3}$$

For frequencies below f^*, the pressure gradient term in equation 3.2 can be neglected and it can be shown [67] that the relationship between the amplitude of the seeding particle velocity $|u_p|$ and the acoustic particle velocity amplitude $|u_a|$ is:

$$|u_p| = \frac{|u_a|}{\sqrt{1 + 2\pi f \tau_p}} \tag{3.4}$$

and the phase angle of the seeding particle velocity is:

$$\angle u_p = \angle u_a - \tan^{-1}(2\pi f \tau_p). \tag{3.5}$$

As indicated by equations 3.4 and 3.5, the particle response relative to the fluid becomes more precise with decreasing particle diameter. However, for health reasons, there are limitations to the smallest particle size usable unless the experiment has a built-in particle extraction system. A list of particles typically used to seed PIV flows in various mediums is given in table 3.1.

Medium	Particle	Diameter (μm)
Gas	Incense Smoke	<0.5
	Oil (Atomised)	0.5-10
Liquid	Silver-coated hollow glass spheres	40
	Conifer Pollen	50-70
	Gas Bubbles	50-1000

Table 3.1: Typical particles used in PIV to seed gas and liquid flows.

Light scattering characteristics

In addition to closely tracking the motion of the fluid, the particles must scatter sufficient light to be detected by the recording medium. The intensity of light scattered depends strongly on the particle size and angle of observation of the scattered light. In the case of particles used to seed gas flows for PIV, which typically have a diameter greater than the wavelength of the incident light, Mie's scattering theory can be applied. This shows that the average intensity of scattered light observed at an angle between 0 and 180 degrees from the incident beam approximately scales with the square of the particle diameter [99]. Brighter images can therefore be produced using larger particles, but at the expense of the particle response to the fluid motion. Alternatively, the concentration of particles can be increased, but this increases the background noise. Hence, it is necessary to reach a compromise between these two size requirements. The advantage of PIV experiments in air is that the seeding particles have a high refractive index relative to air and hence scatter light more efficiently than seeding particles used in liquid media.

Seeding particle concentration and distribution

The density of seeding particles in the region of investigation of an image is also an important consideration. If the seeding density is so high that particles start to overlap, individual particle images will be replaced by a speckle pattern due to interference of the light scattered from local groups of particles [2]. The displacement of the clusters of particles can be found by statistical analysis of the speckles, a technique known as Laser Speckle Velocimetry (LSV). However, high particle concentrations can interfere with the motion of the flow, causing, for example, two-phase flow effects.

Conversely, if the seeding density is so low that the average particle displacement between images is less than the mean distance between particles, the motion of each particle is tracked using a technique called Particle Tracking Velocimetry (PTV). The disadvantage of working with such a low particle concentration is that some areas of the image may not contain particles, resulting in places where velocity information is not available.

For optimal spatial resolution of a region of flow using PIV, the concentration of particles should be low enough to individually identify each particle but high enough to provide many data points in each interrogation area without interfering with the flow characteristics; thus, a seeding density lying between these two extremes is required. For PIV measurements using double pulsed systems such as employed in this study, a concentration of at least 15 particles per interrogation area is recommended [54]. In addition, the particle distribution should be homogeneous throughout the area of investigation.

Imaging of seeding particles

The size of a particle image is determined by the seeding particle diameter, d_p, the magnification, M_I, and the resolution of the lens. Assuming an aberration-free lens, due to diffraction the minimum particle image diameter corresponds to an Airy disk of diameter d_{diff} [4, 83] given by

$$d_{diff} = 2.44(1 + M_I)f^{\#}\lambda, \tag{3.6}$$

where the f-number of the lens, $f^{\#}$, is defined as the ratio of the focal length of the lens to its aperture diameter. For a typical camera lens system, the minimum image diameter is typically of the order of a few microns. For larger particles or magnifications, where the geometrical diameter of the particle becomes important, the particle image diameter d_I is approximated by

$$d_I = \sqrt{(M_I^2 d_p^2 + d_{diff}^2)}. \tag{3.7}$$

It is clear from equations 3.6 and 3.7 that the aperture diameter can significantly affect the quality of the particle images. In order to obtain accurate PIV measurements, the particle images must be focused which requires a large aperture (small f-number) to maximise the amount of light collecting on the recording medium from the illuminated particles, as well as reducing the size of the diffraction pattern. However, this decreases the depth of field which makes focusing of the particles much harder. The problem can be resolved by increasing the distance between the camera and illuminated plane, but this can be undesirable when examining small areas and often requires an increase in illumination intensity.

3.4.3 Recording medium

There are two basic methods for recording PIV images; exposures of the particles are either separately recorded on individual frames (*multi frame - single exposure*) or multiply recorded on one frame (*single frame - multi exposure*).

The main disadvantage with the second method is that, because it is difficult to ascertain which particle images belong to which exposure, the direction of flow cannot be directly determined. Although this can sometimes be resolved from prior knowledge of the flow, in situations where flow reversal occurs e.g. alternating acoustic fields, additional techniques such as image shifting are required (see section 3.5.2).

Significant development in computer processing speeds and charge coupled device (CCD) cameras have led to the almost exclusive use of digital processes in commercial PIV systems today. Originally, images stored on wet film were subsequently developed and optically correlated to find the particle displacements. Whilst providing velocity measurements with a high spatial resolution and wide dynamic velocity range (defined as the ratio of the maximum velocity range to the minimum resolvable velocity measurement [3]), the process of analysing each image was slow, making it impractical as a technique where hundreds of images were involved. Also, limitations on film wind-on rates mainly restricted recordings to multiple-exposure images and hence directional ambiguities arose.

CCD (digital) cameras have a number of significant advantages over wet film. Firstly, they store digital images direct to computer where all analysis is performed computationally, eliminating the need for photographic processing and optical interrogation. Fast frame rates allow the storage of sequential particle ex-

posures on separate frames, removing the directional ambiguity associated with multi-exposure images. Current camera systems have image acquisition rates of at least 10,000 frames per second, allowing high speed flows to be measured comfortably. In addition, most systems allow real-time viewing which is particularly advantageous for system alignment and optimisation of experimental parameters such as seeding density, pulse separation and light intensity.

The most notable difference is in the reduced spatial resolution of digital cameras compared to traditional wet film. The sensor in a CCD camera consists of a rectangular array of individual CCD elements called pixels, with typical arrays of the order of 1000×1000. Photographic film, on the other hand, has a spatial resolution of 100-300 lines/mm, which for a 35mm film corresponds to a CCD array a factor of at last 2-3 times larger. The aim of a PIV image is not to exactly reproduce the flow, but instead provide adequate samples of the motion in order that a statistical analysis can be applied. Work by Westerweel [104] showed that for PIV images, the minimum required sampling rate is only approximately 25% of the optical bandwidth. Hence, the reduced resolution offered by a CCD camera does not have a detrimental effect on the accuracy of the measurements.

A detailed description of CCD sensors is given by Raffel et al.[83] and Dewhirst [27]. Two different camera systems were used in this study to examine the two acoustic velocity regimes, and their specifications are given in table 3.2.

Specification	PCO Super VGA Sensicam	Kodak Megaplus ES 1.0
Pixel size	6.7μm $\times$ 6.7μm	9μm $\times$ 9μm
Array Size	1280(H) $\times$ 1024(V) pixels	1008(H) $\times$ 1018(V) pixels
Scan Area	8.6mm $\times$ 6.9mm	9.1mm $\times$ 9.2mm
Frame Rate	15 frames/sec	15 frames/sec

Table 3.2: Specifications of the two cameras used to obtain PIV images in this study.

3.5 Image analysis

As mentioned in section 3.3, in order to determine velocities from PIV images, each image is divided into a grid of smaller interrogation areas. Each area is then analysed by a statistical correlation procedure to obtain the average particle displacement within each area. This is then converted to an average velocity vector using equation 3.1, and the process repeated for each interrogation area over the whole image to produce a velocity vector map. Since the particle displacement is averaged within each interrogation area, the size of this area therefore limits the spatial resolution of the flow which can be obtained. Typically, an interrogation area size of 32 $\times$ 32 pixels is used.

All of the PIV analysis in this study is carried out using analysis software developed by Schlicke [90]. The Unix-based software, called "TedPIV", is discussed in detail in [90]. There are two basic correlation routines used to analyse PIV images, depending on the method of image acquisition: *cross-correlation* and *auto-correlation*.

3.5.1 Cross-correlation

For PIV images captured as double frames of singly-exposed particle images, corresponding interrogation areas from each frame are cross-correlated to obtain the displacement information. If the sampled images in corresponding interrogation areas of sequential frames 1 and 2 are described by functions $f(x,y)$ and $g(x,y)$ respectively, the cross-correlation function $R_{fg}(x,y)$ is defined as:

$$R_{fg}(x,y) = f(x,y) \otimes g(x,y) = \int_{-\infty}^{\infty}\int_{-\infty}^{\infty} f(\alpha,\beta)g^*(\alpha - x, \beta - y)d\alpha d\beta, \quad (3.8)$$

where $\otimes$ represents a correlation and $g^*(x,y)$ denotes the complex conjugate of $g(x,y)$. For digitally recorded images, functions $f(x,y)$ and $g(x,y)$ are discrete rather than continuous and hence equation 3.8 becomes

$$R_{fg}(x,y) = \sum_{i=0}^{M}\sum_{j=0}^{N} f(i,j)g(i-x, y-j), \quad (3.9)$$

where the interrogation areas are arrays of $M \times N$ pixels.

Alternatively, the calculation can be performed (in the frequency domain) using a fast Fourier transform (FFT) algorithm. From the correlation theorem,

$$R_{fg}(x,y) = f(x,y) \otimes g(x,y) \Leftrightarrow \mathcal{F}\{R_{fg}(x,y)\} = F(u,v)G^*(u,v), \quad (3.10)$$

where $\mathcal{F}$ denotes a Fourier Transform, F(u,v) and G(u,v) are the Fourier transforms of functions f(x,y) and g(x,y) respectively, and * indicates the complex conjugate. Hence, the equivalent cross-correlation calculation given in equation 3.8 can be performed by taking the Fourier transforms of both interrogation areas, cross-multiplying them and then taking the inverse Fourier-transform to obtain

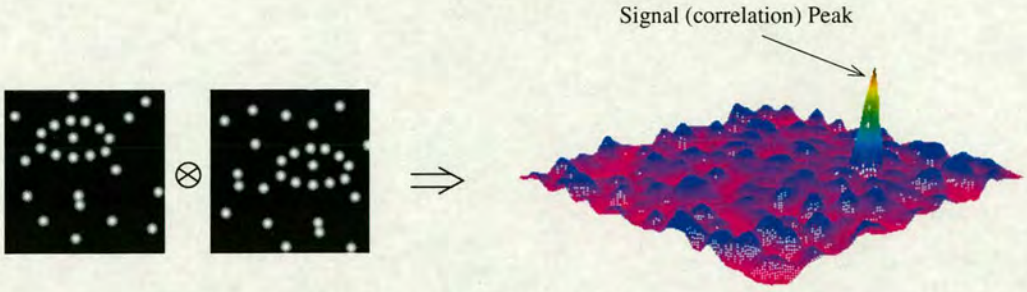

Figure 3.3: The correlation plane produced by cross-correlating two images, where $\otimes$ denotes the correlation.

the cross-correlation plane. This approach is simpler and much faster with regard to processing time than the calculation detailed in equation 3.9, especially for interrogation areas of the same size [108]. A typical cross-correlation plane is illustrated in figure 3.3. The plane contains a single main peak corresponding to the correlation of each particle image in the first frame with itself in the second frame. It also contains smaller peaks corresponding to random background noise, which result from correlations with other particles. The displacement of the main peak from the centre of the plane corresponds to the average displacement of the particle images, and its height is determined by the number of particle pairs with that displacement.

3.5.2 Auto-correlation

If the flow is captured as multiple exposures on a single frame, the displacement information is obtained by correlating each interrogation area with itself, a technique known as auto-correlation. As can be seen in figure 3.4, the auto-correlation plane consists of a peak in the centre of the plane due to the correlation of the image with itself, and two identical peaks equally spaced either side of this peak which correspond to the average particle displacement. Like the cross-correlation

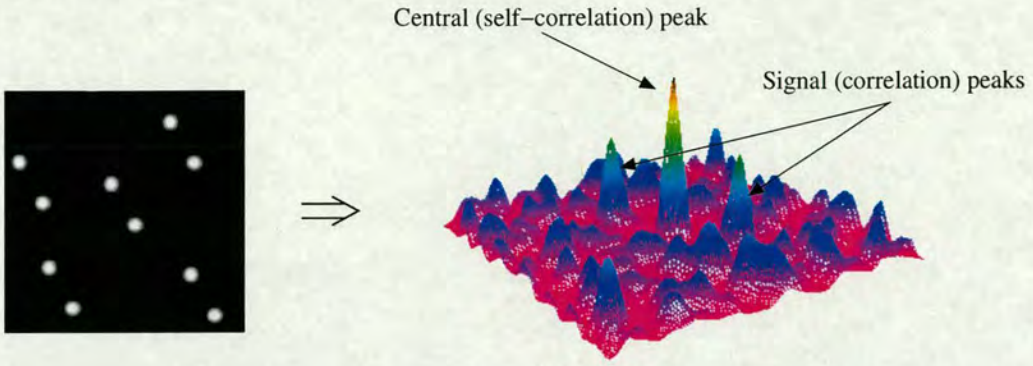

Figure 3.4: The correlation plane produced by auto-correlating a multiply-exposed image.

plane, a number of smaller peaks also arise due to random correlations. Two displacement correlation peaks occur due to the inability to distinguish which images correspond to which exposure, hence resulting in a directional ambiguity of 180° of the final velocity vector. This can particularly cause problems when observing complex flows where the direction of flow reverses, such as at solid boundaries or in the case of time-dependent flows. Additionally, for small or zero particle velocities where particle pairs overlap, it becomes difficult to separate the displacement peaks from the central self-correlation peak. This ultimately results in inaccurate velocity measurements, and limits the dynamic range achievable with the technique. The probability of an increased number of overlapping particles also results in a higher number of random correlations between different particles, hence decreasing the signal-to-noise (S/N) ratio. This is undesirable, as it decreases the likelihood of detecting the signal peak. It was found that analysis using auto-correlation produced approximately twice the number of random noise peaks found by analysis using cross-correlation [55].

The direction of the flow can be resolved by a number of techniques. The most common method is *Image shifting*, where the particle images in the second

exposure are displaced a constant distance during image acquisition by moving the camera or using a rotating mirror. This shift is then removed as part of the analysis process [1]. However, although removing the directional ambiguity, the method complicates the experimental set-up and introduces additional errors which need to be considered during analysis.

Comparing the two techniques, the wider dynamic range of velocity measurements coupled with the ability to resolve the direction of flow directly makes cross-correlation the favoured choice.

3.5.3 Peak detection

An important consideration in image analysis is how accurately the location of the correlation peak, and hence the particle image displacement, can be measured. The discrete (i.e. pixelised) format of digitally recorded images allows displacements to be measured to within an error of $\pm$ 0.5 pixels. Although this may be acceptable for large displacements within the interrogation area, for smaller displacements or investigation of turbulent flow a more accurate measurement is required.

The location of the peak can be measured to sub-pixel accuracy by applying peak-fitting functions to the nearest neighbouring points of the peak. Two of the most widely used routines, referred to as *three-point estimators*, are the parabolic-fit and Gaussian-fit estimators [104]. These estimators produce the most accurate results for narrow correlation peaks. In general, fitting a Gaussian curve to the points has been found to yield better results than fitting a parabolic curve. This can be explained by the fact that particle images essentially have a Gaussian

intensity profile, and hence correlating these two Gaussian functions produces a correlation peak with a similar Gaussian distribution. The analysis software used in this study implements the Gaussian-fit estimator for peak detection, achieving a measurement error of ± 0.1 to 0.05 of a pixel [83].

3.5.4 Errors in image analysis

In order to obtain accurate velocity measurements, it is obviously desirable to maximise the main peak amplitude compared to the random correlations, thus increasing the number of valid correlated pairs and reducing the random correlations; this is dependant on a number of factors [54].

In-plane and out-of-plane motion

The height of the correlation peak will decrease due to particles entering or leaving the interrogation area (*in-plane motion*) or light sheet (*out-of-plane motion*) between the first and second exposures. One solution is to choose the time separation Δt between the two exposures such that the majority of particles remain within the sampled area for both exposures, but are displaced far enough to be accurately resolved. Nyquist's sampling theorem restricts the maximum resolvable spatial displacement of the flow to half the interrogation width, corresponding to an overlap in interrogation areas of 50% [27]. In reality, such a large average displacement results in a decrease in the number of correctly paired particles and hence the height of the correlation peak. Keane and Adrian found that, for auto-correlation, optimal results are obtained provided the image displacement does not exceed 30% of the interrogation width [54]. In the case of cross-correlation, a larger interrogation window can also be used for the second image to ensure all

the particles are captured in the second exposure, but this requires longer computational time and reduces the pixel resolution in the first interrogation area [55].

Seeding particle concentration

The seeding particle concentration should be high enough to generate sufficient correlated image pairs, which increase the signal-to-noise ratio and hence the probability of obtaining a velocity vector which accurately represents the average motion in that area. However, too much seeding can result in particle images overlapping, distorting the displacement peak. Keane and Adrian recommended a minimum image density of 7 particles per interrogation area for optimal cross-correlation results (95% valid detection rate) [55], and greater than 15 particles for auto-correlation (for the same detection probability of 95%) [54]. Due to the statistical method of analysis, the particle distribution should also ideally be homogeneous throughout the area.

Particle image size

The diameter of the particle image has a significant effect on the resolution of the correlation peak. If the image diameter is too small, the correlation peak will be very narrow. This results in low values at neighbouring points to the peak, and hence the three-point estimator will yield displacement measurements which tend towards integer values in pixel units, an effect known as *peak-locking.* If, on the other hand, the image diameter is too large, the correlation peak will broaden and decrease in amplitude, resulting in a lower signal-to-noise ratio and hence smaller probability of a valid displacement value. For cross-correlation analysis, the optimal image diameter for good correlation peak measurements has been

shown to be approximately 2 pixels [83]. If the particle images are lower than this value, peak-locking can be avoided by slightly defocusing the image.

Interrogation area size

The size of the interrogation area depends on the nature of the flow under investigation; it should be large enough to contain sufficient particle images for good cross-correlation, but not so large that detailed flow information is lost through averaging. Ideally, the velocity gradient across each area should also be very small (such that the velocity variation is less than 5% of the mean velocity) [54]. Velocity gradients broaden the width and diminish the amplitude of the main cross-correlation peak, reducing the signal-to-noise ratio which can result in poor or unsuccessful measurements.

A bias towards smaller velocities, known as *bias error*, also arises due to the finite width of the interrogation area. This effectively weights the correlation function by a window function, which is determined by the correlation (i.e the overlap) of the two interrogation areas. Hence, for the case of two identically

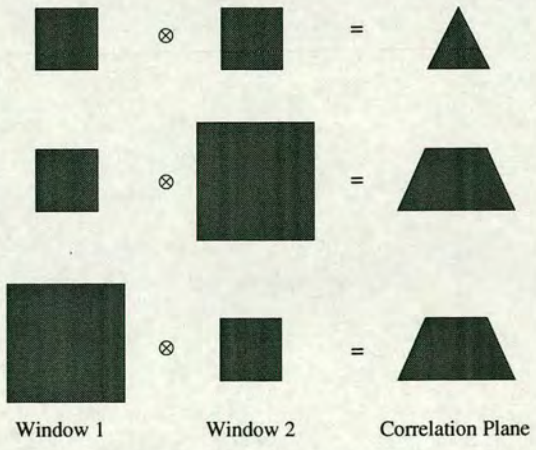

Figure 3.5: The effect of different interrogation area sizes on the window function, where ⊗ denotes the correlation (adapted from [106]).

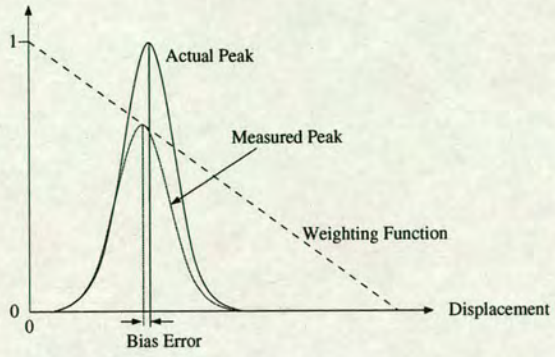

Figure 3.6: Modification of the displacement-correlation peak as a result of the triangular window function shown in figure 3.5 (adapted from [106]).

sized interrogation areas, the correlation peak is modified by a triangular function [106] as shown in figure 3.5. This not only broadens and lowers the peak but shifts its displacement to a lower value, as illustrated in figure 3.6. This bias is enhanced further when velocity gradients are present because this broadens and lowers the peak, an effect known as *gradient bias*. For a 32 $\times$ 32 pixel interrogation area, the bias error has a typical value of 0.1 pixels, a significant value when examining small displacements. The bias error can be reduced in a number of ways. Since the mathematical form of the weighting function is known, *weight kernels* can be applied to it to correct the values. Alternatively, two differently sized interrogation areas can be used. This effectively broadens the window function, hence reducing the size of the error, as illustrated in figure 3.5. As can be seen from this figure, it is not important which interrogation area is smaller.

The third method which can be used to eliminate bias error is a process called *re-interrogation*, which is discussed in the next section.

3.5.5 Further correlation techniques

Re-interrogation

Re-interrogation is a technique which is frequently employed to improve the accuracy of the initial displacement measurement. Its principle follows from a study by Westerweel et al. [107], who showed that the RMS error in the displacement value rapidly decreases for displacements less than 0.5 pixels. Hence, once the displacement of the peak has initially been evaluated using cross-correlation, shifting the interrogation area in the first image by the nearest integer value of this displacement should reduce the new correlation peak displacement to less than ± 0.5 pixels. Repeating the cross-correlation routine will then greatly reduce the error involved with the final displacement value. The additional advantage with this technique is that decreasing the particle displacement increases the probability of more particles being present in both image exposures, therefore increasing the S/N ratio and significantly reducing biasing effects. This also means that the size of the interrogation area can be reduced further, increasing the spatial resolution of the final measurement.

Vector validation

In any analysed PIV image there will be a certain number of spurious vectors, known as *outliers*, which are non-physical. These outliers, which usually deviate wildly both in magnitude and direction from the valid vectors and are therefore easy to spot, result from random correlations, large velocity gradients and areas of low seeding density or illumination intensity, as well as effects such as glare

and reflections from surfaces. As well as being visually detractive, they can obscure small spatial structures in the flow and cause problems when calculating turbulence parameters such as vorticity and shear. Investigation of flows using PIV usually requires taking many images, making it unrealistic to attempt to validate each image by eye and remove erroneous vectors. It is therefore desirable to use a validation algorithm which will detect and remove these outliers and replace them with more realistic velocity vectors.

The validation technique used in this study, incorporated into the PIV analysis software by Schlicke [90], is based on the *local median* filtering method [83, 105]. For each velocity vector, the velocities of its nearest neighbouring points (typically restricted to the eight nearest neighbours) are placed in order of increasing magnitude and the central, or median, value found. The original velocity vector is then compared to this median value, and rejected and subsequently removed if the difference between the two values exceeds a critical value specified by the user. This critical value is chosen to suit the flow under investigation.

Once the entire vector map has been validated, a number of gaps will exist where vectors have been rejected. In order to avoid problems with further processing algorithms, particularly when calculating quantities such as vorticity and other turbulent quantities, it is often desirable to fill in the gaps. Numerous methods exist which use interpolation algorithms to replace the outliers with more suitable vectors [83]. An example of a PIV velocity map before and after validation and interpolation is shown in figure 3.7. However, the replacement vectors have to be estimated from the values of neighbouring vectors and are therefore not statistically independent. As this study involves investigation of small non-linear effects, where interpolation due to vector replacement could have a significant ef-

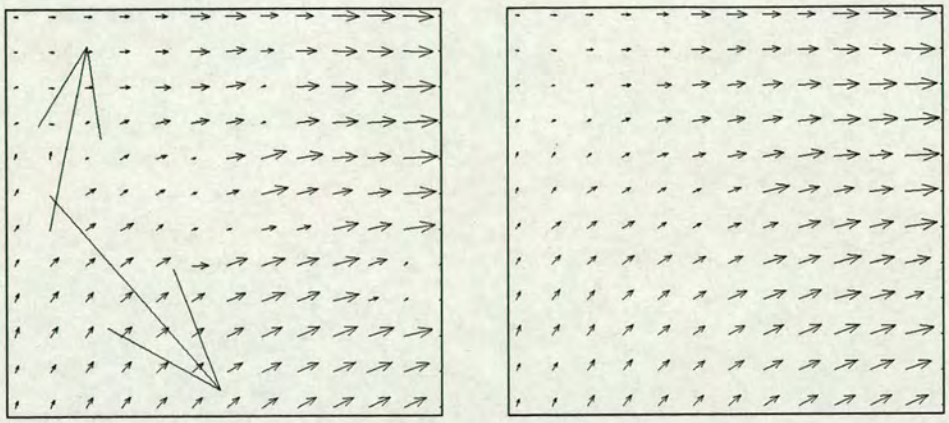

(a) (b)

Figure 3.7: Typical vector map (a) before and (b) after validation.

fect, interpolation routines have not been employed unless specifically described. Instead, if a cluster of outliers were observed during the initial analysis procedure, the experiment was repeated.

3.6 Summary

In this chapter, the technique of Particle Image Velocimetry (PIV) was introduced. Unlike many alternative techniques for measuring acoustic velocities, PIV allows instantaneous full-field velocity measurements of a planar cross-section of flow to be obtained, without the problems of calibration, directional ambiguity and, most importantly, physical intrusion into the flow.

The basic principle behind PIV was outlined, and the methods of obtaining and analysing images presented. The PIV systems used in this study are comprised completely of digital processes, with images acquired by a CCD camera and

analysed computationally. A number of important considerations with regard to the choice of parameters during the experimental set-up, image acquisition and analysis were discussed. Possible sources of error and techniques for minimising their effects were considered, and recommendations made for optimising the accuracy and reliability of the velocity measurements. Details of the PIV systems used in this study are given in the following chapter.

Chapter 4

Experimental apparatus and preliminary measurements

4.1 Introduction

In this chapter, the experimental apparatus used in this study is introduced. Initially, the basic loudspeaker-tube configuration is described in section 4.2. The three PIV systems used to measure the acoustic fields in chapters 5, 6 and 7 are then outlined in section 4.3, along with the methods for obtaining PIV images. The limitations associated with each experimental configuration are also discussed. Section 4.4 considers the characteristics of the seeding particles used in this study. Section 4.5 is then devoted to the calibration of the probe microphones and pressure transducer. Finally, the orientation of the probe microphone relative to the acoustic flow is discussed.

4.2 Acoustic signal

All the PIV measurements discussed in chapters 5-7 involve the investigation of acoustic fields inside or in the near vicinity of cylindrical tubes with a range of diameters from 22-31mm. The acoustic field was generated inside the tube using a JBL 2446H 8Ω compression driver driven by a high-precision Stanford sine-wave generator and amplifier. In order to attach the loudspeaker to the tube, an aluminium cylinder with a tapered bore was constructed as illustrated in figure 4.1. This was designed to channel the acoustic field from the 2 inch throat of the loudspeaker directly into the tube with minimum distortion of the field itself. A ledge was cut into the small end of the tapered bore to seat the tube such that the internal walls of the tube were flush with the bore of the cylinder. To ensure a good seal around the join, two o-rings were inset into the aluminium wall and additional vacuum grease was used when inserting the tube. With the tube in place, the acoustic field was investigated with the tube open at the opposite end to the loudspeaker, and closed by a metal plug, as illustrated in figure 4.2. In both cases, the pressure field at the end of the tube and at various points inside it were measured using a Brüel and Kjær (B&K) probe microphone.

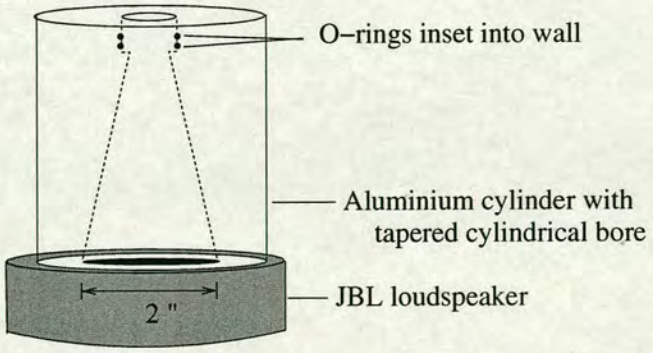

Figure 4.1: Apparatus for connecting the loudspeaker to the tube.

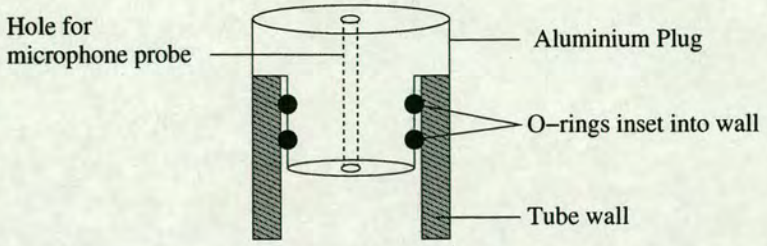

Figure 4.2: Metal plug used to terminate the tube.

4.3 PIV apparatus

The two velocity regimes of interest in this study are the oscillating acoustic particle velocity, and slower mean motion of acoustic streaming. Acoustic particle velocities were mainly investigated at low frequencies around 700Hz, with amplitudes in the order of 0.1 to 10m s^{-1}. Acoustic streaming measurements were made using sound fields in two frequency ranges; 1700-2200 Hz for the case of the closed end tube and 600-800 Hz for the side hole measurements. The amplitudes of these streaming velocities ranged from 0.01-0.3m s^{-1}. Due to the different requirements needed to measure these two velocity regimes accurately, different PIV set-ups were therefore used.

4.3.1 Apparatus for acoustic velocity measurements

The PIV apparatus used to measure the oscillating acoustic particle velocity is illustrated in figure 4.3. A Spectra-Physics Nd:YAG pulsed laser in Q-switching mode was used to generate double pulses of light of wavelength 532 nm, with a pulse duration of 6-7 ns and maximum pulse energy of 67 mJ. The pulsed beam was passed through an optical configuration consisting of a negative spherical

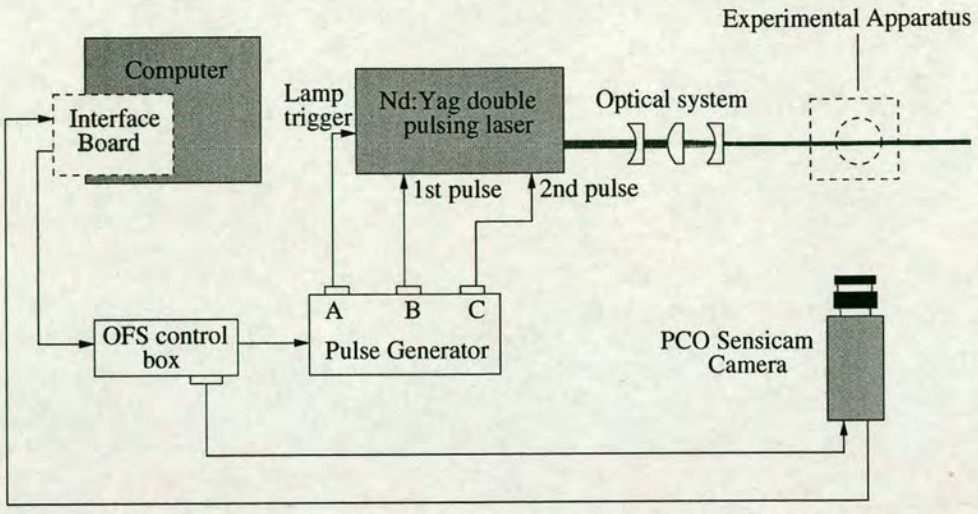

Figure 4.3: Apparatus for taking PIV measurements of the acoustic sound field using the Nd:YAG pulsed laser.

lens and a positive spherical lens, with focal lengths f=-150 mm and f=200 mm respectively, and finally a cylindrical lens which expanded the beam into a thin light sheet of height 50 mm, as illustrated in figure 3.2. This light sheet was then directed through the area of flow requiring investigation, with the beam focus situated approximately at the centre of the tube. The combination of two spherical lenses produces a beam whose thickness remains approximately constant over the diameter of the tube and can be altered by changing the relative position of the two lenses [36], whilst the choice of cylindrical lens influences the height of the light sheet. Due to the high power of the laser beam, it was necessary to keep the path of the beam up to and beyond the experimental apparatus enclosed at all times, with the path through the experimental apparatus also enclosed when the laser was on. Due to the inaccessibility of the beam alignment optics, as well as the problems associated with realignment, the position of the lenses remained fixed at all times. Hence, the experimental apparatus was moved relative to the fixed position of the light sheet.

A Kodak ES 1.0/SC CCD camera, used in conjunction with a 55mm Micro-Nikkor lens (with f-number set at $f^{\#}$=2.8), was placed normal to the illuminated plane at a distance of 40cm to allow an area of approximately 5cm × 5cm to be imaged. A Stanford timing box (DG535) was used to trigger the camera via a frame grabber card mounted in the computer, and to synchronise the subsequent camera exposures with the pulses of the flash lamp. Controlling the beginning of the image acquisition by purpose-written software (OFS VidPIV version 3.0), pairs of images 40μs apart were captured at a frequency of 10Hz and stored on the frame grabber memory. Each image was then transferred to the hard drive of the computer in bitmap format in preparation for analysis. A maximum number of 120 pairs of images (240 individual frames) could be acquired at any one time due to the finite size of the frame grabber memory.

The short intense pulses of light delivered by the Nd:YAG laser offer sufficient illumination to successfully image the small seeding particles used whilst effectively freezing the motion of the particle, two of the main requirements for valid PIV images. Unfortunately, the fixed time separation of 40μs between the two pulses limits the velocity range which can be investigated; this depends on a number of factors including the nature of the flow, the size of the area under investigation and the choice of interrogation area size, as discussed in chapter 3.

4.3.2 Apparatus for acoustic streaming measurements

The apparatus used to measure the slower mean motion of acoustic streaming inside a closed-end tube, described in Chapter 5, is illustrated in figure 4.4. A Laser Quantum Forte 530 solid-state diode pumped 300mW laser produced a

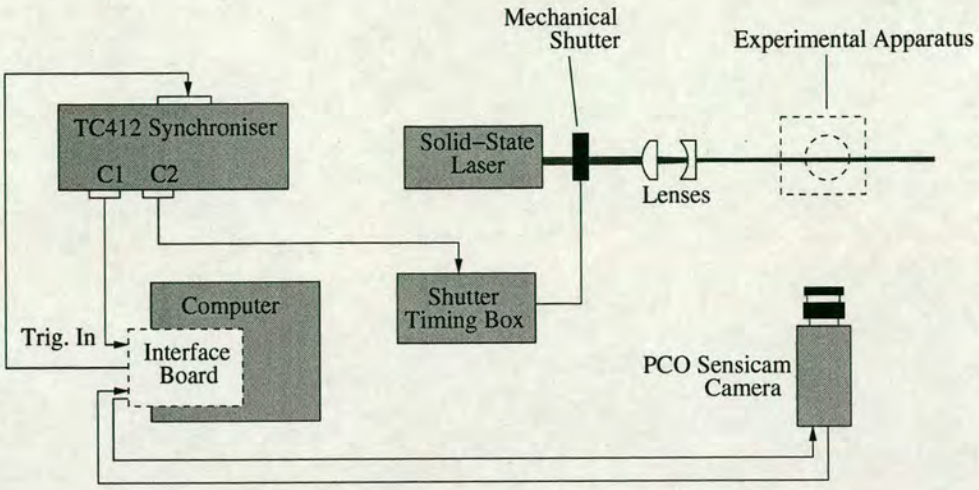

Figure 4.4: Apparatus for obtaining PIV measurements of the acoustic streaming using the Laser Quantum solid-state laser.

beam of wavelength 532nm and unfocused beam diameter of 0.4mm. The beam was directed through a 200mm focal-length plano-convex lens and a 10mm cylindrical lens which expanded the beam into a light sheet of thickness ≈0.6mm and width 50mm. This light sheet was then projected through the axis of a tube positioned close to the optical assembly. A small mechanical shutter, controlled by a separate timing box, was placed in front of the unfocused beam to generate light pulses. Unlike the optical system described in section 4.3.1, this configuration does not allow manipulation of the light sheet thickness. However, the unfocused beam diameter was considered small enough to yield an adequately thin light sheet for PIV measurements using just these two lenses, provided the area requiring illumination remained close to the optical system.

A PCO Sensicam CCD camera, positioned normal to the illuminated plane, imaged the light sheet with the aid of a 105mm Micro-Nikkor lens with f-number set at $f^{\#}$=2.8. With the assistance of a frame-grabber card and OFS electronics synchronising box, OFS VidPIV software (version 3.02) was used to trigger the camera in synchrony with the mechanical shutter. Pairs of single particle expo-

sures were taken with a typical pulse width of 6ms and separation of 30ms. Each image was then saved in bitmap format.

The main disadvantage with this set-up is that the light pulses produced are fairly weak; this problem was made worse by the unavoidable Gaussian profile of the beam and intermittent flickering of the beam due to instability. This ultimately results in fainter particles and hence lost or invalid data on the image, particularly at the edges. Although the particle exposure times can be increased, a compromise needs to be found between sufficient illumination of each particle and blurring due to the particle displacement being too great.

4.3.3 Apparatus for measuring both velocity regimes

The limited pulse separation times and frame repetition rates of the systems described in sections 4.3.1 and 4.3.2 restrict their application to the measurement of *either* slower streaming velocities *or* fast flows. For experiments where both velocity regimes are of interest, it is more advantageous to choose a system which can measure a much wider range of velocities, provided the accuracy of the PIV measurements is not compromised.

The experimental apparatus illustrated in figure 4.5 offers one possible alternative. A Copper-Vapour laser was used to produce double pulses of light of wavelength 510.6nm, with a pulse duration of 2μs and maximum pulse energy of 6mJ. The pulsed light beam was transmitted through an optical fibre to the experimental set-up, where it was expanded into a light sheet of width 50mm and thickness 1mm using two cylindrical lenses of focal length 150mm. The PCO Sensicam camera, with a 55mm Micro-Nikkor lens set at an f-number of $f^{\#}$=2.8,

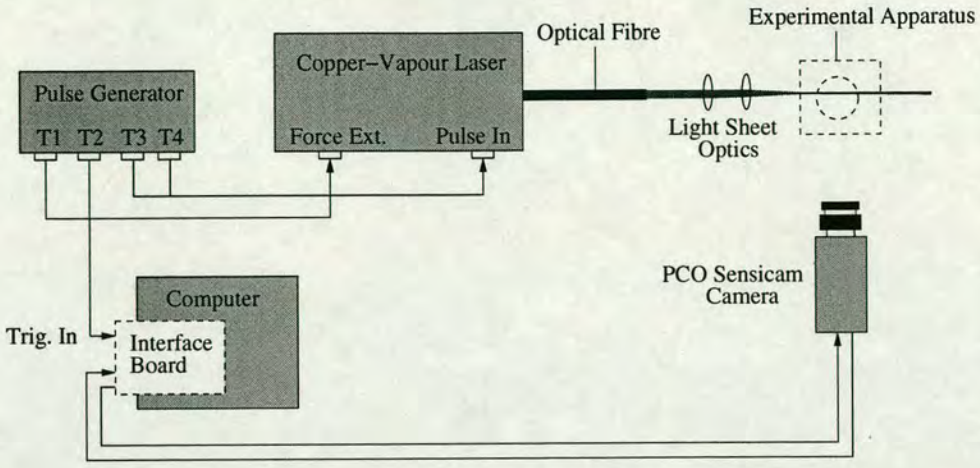

Figure 4.5: Apparatus for obtaining acoustic velocity measurements using PIV with the Copper-Vapour laser.

imaged the illuminated plane. A Berkeley Model 500 timing box was used to control the double laser pulses and simultaneously trigger the camera via a frame grabber card in the computer. Controlling the beginning of the image acquisition manually from the timing box, single pairs of images were recorded with each pulse lasting 2μs and a separation time between pulses of 1ms.

In double shutter mode, the PCO Sensicam camera system can record pairs of images with a minimum separation time of 200ns and exposure time of 1ms-1000ms, at a repetition rate of 12-15 frames per second. Hence, fast flows of the order of metres per second can easily be captured when used in conjunction with the Copper-Vapour laser. Unfortunately, the limited frame rate of the camera makes it impossible to obtain multiple pairs of images within one acoustic cycle. However, the system can be easily modified by replacing the PCO Sensicam camera system with a high-speed camera and corresponding software, enabling double images to be recorded at a repetition rate of 10kHz. For an acoustic field of frequency 700Hz, this corresponds to an image every 0.1ms and therefore 7 image pairs per acoustic cycle. The ability to investigate velocities of acoustic

Experiment	**Camera**	**Laser**	**Pulsing System**
Acoustic streaming (Chapter 5)	PCO Sensicam + Micro-Nikkor 105mm lens ($f^{\#}$=2.8)	Laser Quantum solid state	Mechanical shutter in front of beam
Acoustic particle velocity at open end of tube (Chapter 6)	Kodak Megaplus ES 1.0 + Micro-Nikkor 55mm lens ($f^{\#}$=2.8)	Nd:YAG	Pulsed laser
Acoustic streaming at side holes (Chapter 7)	PCO Sensicam + Micro-Nikkor 55mm lens ($f^{\#}$=2.8)	Copper Vapour	Pulsed laser

Table 4.1: Summary of the experimental apparatus used to obtain PIV measurements for the three situations discussed in this study.

fields within one cycle, whilst not considered in this study, may provide further insight into specific acoustic phenomena.

All three systems allow real-time viewing of the flow, which saves time when initially aligning the system and allows the optimisation of variable experimental parameters. The image acquisition program also contains analysis software, thus allowing images to be cross-correlated immediately. This can be an invaluable feature for checking experimental parameters before a large number of images are taken.

A summary of the individual components used for the three experiments is given in table 4.1.

4.4 Seeding particles

The two types of particles chosen to seed the flows in this study were incense smoke and neutrally buoyant bubbles. Cheng et al. [20] observed that incense particles have diameters less than 0.5μm and a density of approximately 1060 Kg m^{-3}.

Hence, from section 3.4.2, the pressure gradient force can be ignored at frequencies below $1/(2\pi\tau_p)$ which corresponds to 163kHz. For the maximum frequency used in this study of 2.2kHz, equations 3.4 and 3.5 suggest that the particles will lag the fluid flow by less than 1^o with an amplitude of oscillation of 99.3 % of the acoustic particle velocity amplitude. Therefore, the effect of the viscous drag and pressure forces on the particle response can be assumed to be negligible for the range of frequencies used here. However, as shown by Keith and Derrick [59], smoke particles coagulate into larger masses relatively quickly. This results in fewer particles, each with a larger mean diameter, which ultimately affects the particle response relative to the fluid. Hence, it is important to take all measurements within a few minutes of seeding the flow.

The neutrally buoyant particles were generated by a JEM Hydrosonic 2000 haze generator. The particles have diameters in the range 1μm to 4μm [53], a result confirmed by measurements made using a Dynamic Light Scattering (DLS) technique. This gives a value of $1/(2\pi\tau_p)$ from 2.7 kHz to 44 kHz, which is above the frequencies used in this study. Assuming a seeding density of $1000\mathrm{Kg\,m^{-3}}$, in a 2.2kHz acoustic field, bubbles with a diameter of 1-4μm will lag the fluid flow by approximately 3^o to 40^o and oscillate with an amplitude of 97.5% to 73.8% of the acoustic particle velocity amplitude. Although it is clear that the larger particles do not follow the flow closely, the results from the DLS and work by Valière et al. [98] suggest that most of the particles have $d_p \simeq 1\mu$m and hence will follow the flow closely below frequencies of 2.2kHz.

4.5 Microphone calibration

For this study, pressure measurements of the acoustic field were made using a Brüel and Kjær half-inch probe microphone, which consisted of a type 4192 microphone cartridge, preamplifier and a probe attachment. The voltage signal from the microphone was fed into a Brüel and Kjær type 2609 measuring amplifier which converted the measurement to pressure (in decibels). Throughout the experimental measurements, the microphone and amplifier were frequently calibrated using a Brüel and Kjær sound level calibrator. This outputs a 94.0 dB 1kHz sound, which allows the pressure reading on the measuring amplifier to be calibrated to within ±0.5dB.

For the majority of the experimental measurements, two different probes were used, depending on the position and accessibility of the point being measured; a short probe of length 3.8cm and a longer probe of length 23.5cm, both with an internal diameter of 1.5mm. The advantage of using a probe attachment is the ability to take measurements in spaces inaccessible to standard microphones. However, the addition of a probe changes the frequency response of the microphone, and hence calibration is required to compensate for this change.

4.5.1 Experimental method

The change in frequency response of the microphone due to the probe can be evaluated by measuring its response relative to a similar microphone without a probe attached using a closed coupler technique [16]. The experimental apparatus used to calibrate the probes is shown in figure 4.6. The reference microphone,

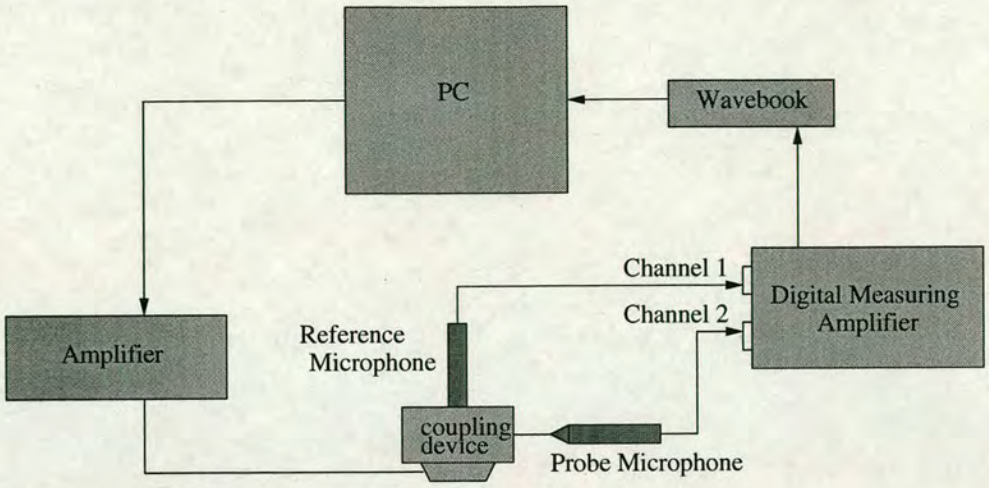

Figure 4.6: Experimental apparatus for calibrating the probe microphone.

a Brüel and Kjær type 4192 half-inch microphone, was screwed into the top of a Brüel and Kjær coupling device supplied with the probes specifically for calibration purposes (UA0040 probe microphone kit). An ear-piece inside the coupling device acted as the sound source. The end of the probe, attached to a second half-inch type 4192 Brüel and Kjær microphone, was inserted into the side of the coupling device. A sine wave signal generated by the PC was amplified and fed into the coupling device via the ear-piece. The voltage signals from the reference and probe microphones were fed into Channels 1 and 2, respectively, of a NEXUS conditioning amplifier. The amplified output voltages from the amplifier were then sampled simultaneously by a Wavebook 512 A/D converter connected to the PC. Stepping up the frequency of the input sine wave using software written by Cullen [23], the frequency response of the probe was measured in 5Hz intervals over the range 50Hz to 2500Hz. The frequency response of the probe relative to the reference microphone was then calculated for each frequency using a modified version of a program called auto.c, written by Cullen [23]. The magnitude response, R_p, of the probe microphone relative to the reference microphone

is given by:

$$R_p = 20 \log_{10} \left(\frac{V_p}{V_r} \right) \tag{4.1}$$

where V_p and V_r are the RMS amplitudes of the output voltage signals from the conditioning amplifier corresponding to the probe and reference microphones respectively.

As indicated in [16], the Brüel and Kjær half-inch microphones are reverse-biased. Hence, the actual phase of the reference microphone pressure equals the measured phase of the reference signal, α_r, minus π. The true phase response of the probe microphone is then obtained from the measured phase of the probe microphone, α_p, using $\alpha_p - \alpha_r + \pi$.

4.5.2 Results

The frequency responses of the long and short probes relative to the reference microphone are shown in figure 4.7. The magnitude response curve for the long probe contains four resonance peaks over the measured range at approximately equally spaced intervals. If the acoustic wavelength corresponding to the frequency of these four peaks is given by λ_i, where i=1-4 denotes the first to fourth peak respectively, the peaks occur when $\lambda_1/4$, $3\lambda_2/4$, $5\lambda_3/4$ and $7\lambda_4/4$ are marginally greater than the length of the probe. Hence, the long probe responds in a similar manner to the pressure response measured at the closed end of a cylindrical pipe with the opposite end open. The short probe, however, only has one pronounced resonance peak in the magnitude response curve. It therefore appears to act as a Helmholtz resonator, which is an expected result given that the length of the probe is small compared with the acoustic wavelength [60].

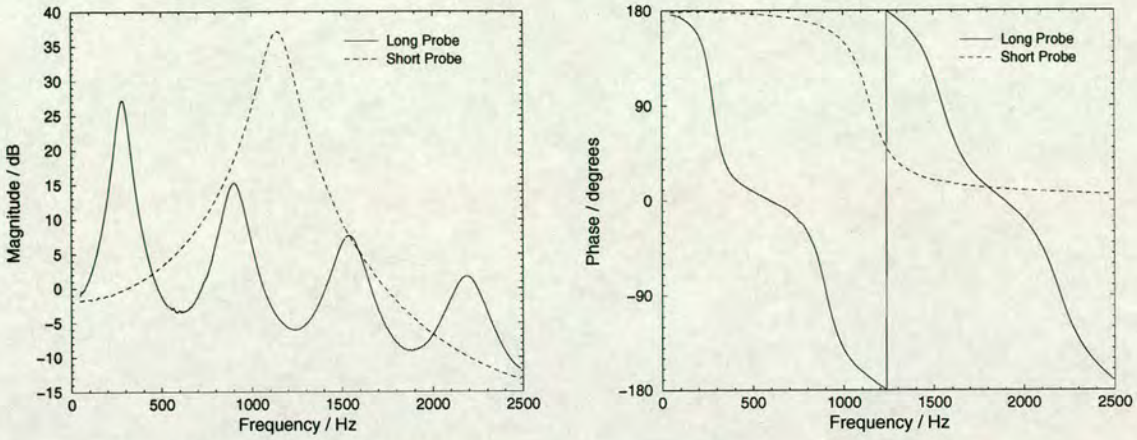

Figure 4.7: Frequency response of the long and short probe microphones.

4.5.3 Pressure transducer

For the study of acoustic flow in the vicinity of side holes presented in Chapter 7, the internal sound pressure level at the base of the tube was measured using a PCB Piezotronics pressure transducer, type 106B. The transducer, of external diameter 11mm, was mounted in a perspex block secured to a section of the tube such that the microphone face lay flush with the inner tube wall.

The transducer is specifically designed to measure high pressure levels (>140dB), to within an accuracy of less than 0.05dB. This is particularly useful for pressure measurements at intensities above 155dB, which is beyond the range of the probe microphones described above. The sensitivity of the transducer was 309.3mV/psi, equivalent to 0.00448mV/Pa. Although it would have been desirable to check the frequency response of the pressure transducer using a similar method to that used to calibrate the probe microphones, it was not possible to attain a sufficient intensity level inside the acoustic coupler to yield valid calibration measurements. Hence, in order to check the consistency between pressure measurements taken using the probe microphone and the transducer, the short probe microphone was

mounted in the same perspex block as the transducer, positioned directly opposite the transducer with the probe tip flush with the inner tube wall. Simultaneous pressure measurements were taken between 130dB and 150dB, in the operating range of both the probe microphone and PCB pressure transducer. Good agreement was found to within an error of 0.2dB. This was considered satisfactory for the qualitative measurements described in Chapter 7.

4.6 Microphone orientation

The introduction of any measuring device into a sound field will disturb the acoustic flow around the device to some degree, hence affecting the reliability of the measurement. In the case of the probe attachments used to take pressure measurements in this study, stationary eddies are clearly observed around the probe tip as illustrated in the photograph in figure 4.8. Observations show that this effect also depends on the orientation of the device relative to the tube; more prominent shedding is seen when the probe microphone is aligned along the tube axis than when placed normal to it. In order to evaluate the importance of the microphone orientation on the measured acoustic pressure level, and hence the degree of sound field distortion, pressure measurements were acquired using the long probe microphone orientated both parallel and at 90^o to the direction of the sound field.

A tube of length 30cm and diameter 2.2cm was connected to the loudspeaker as described in section 4.2, with the tube open at the end opposite the loudspeaker. The probe microphone was positioned parallel to the tube axis with the tip of the probe at a point 1.7mm outside the tube on the central axis. The position of the

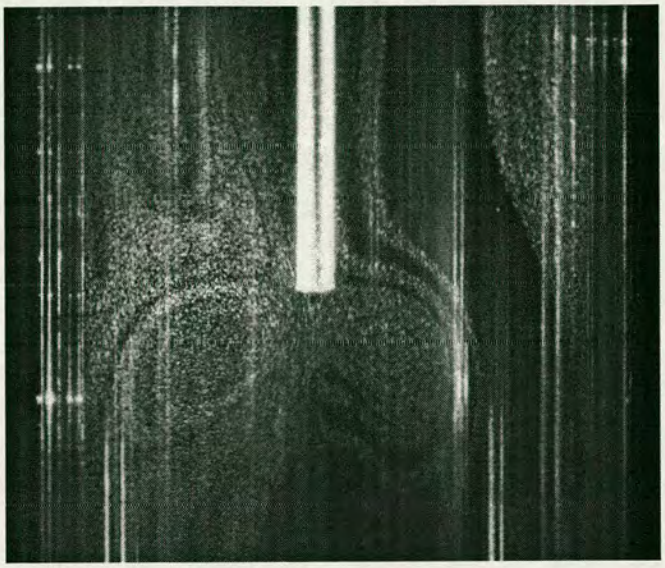

Figure 4.8: Photo of the acoustic field disturbance caused by a microphone probe.

microphone tip was aligned to within ±0.1mm using the Kodak ES 1.0 camera and 55mm Micro-Nikkor lens (see section 4.3.1) running in real-time viewing mode. A 560Hz standing wave was set up in the tube, and pressure measurements taken using the measuring amplifier at 5 points across the tube width. The probe was then positioned at 90° to the tube axis, with the centre of the probe tip in the same position as before, and the pressure measurements repeated. This was repeated at two sound intensity levels of approximately 120dB and 130dB.

As can be seen from the results in table 4.2, the pressure measured by the probe placed parallel to the sound field is higher than that measured when perpendicular to the tube axis, with a pressure difference of 1.6dB at an intensity level of 130dB. It therefore follows that the magnitude of the pressure field distortion due to the presence of the microphone will be at least as great as the pressure difference incurred by a change of probe orientation.

Measurement	Probe parallel to tube axis(dB)	Probe at 90° to tube axis(dB)
1	120.9	120
2	130.3	128.7

Table 4.2: Pressure measurements taken at a specific point outside a tube exit, for two intensity levels, by the long probe microphone orientated parallel to, and perpendicular to, the tube axis.

4.7 Summary

The experimental arrangement of the three PIV systems used in this study was presented, and the respective methods for obtaining PIV images described. The problems associated with each configuration were also discussed.

The attributes of the two types of seeding used in this study were considered. PIV obtains flow information from the velocity of seeding particles suspended within a fluid rather than the velocity of the fluid itself. Hence, the response of the particles relative to the flow determines the accuracy of the velocity measurements. For the range of frequencies pertaining to this study, only the viscous drag force should affect the particle motion. Calculations suggest that incense smoke particles should oscillate with an amplitude 99.3% of that of the acoustic velocity amplitude and lag the fluid motion by less than 1^o for frequencies less than 2.2kHz. Due to their larger diameter, the neutrally buoyant bubbles should oscillate with an amplitude of 73.8% of the acoustic velocity and lag the fluid motion by less than 40^o at frequencies less than 2.2kHz.

The probe microphones used in this study allow pressure measurements to be taken in confined spaces inaccessible to standard microphones, but the addition

of the probe attachment changes the frequency response of the microphone itself. The frequency response of the probe microphone, with both the long and short probe attachments, was measured relative to a reference microphone. This allowed the amplitude and phase components of subsequent pressure measurements to be corrected to compensate for the non-linear response incurred by the presence of the probe attachments.

The presence of a measuring device such as a probe microphone in a sound field has been observed to distort the acoustic flow. Measurements at a fixed position within an acoustic field showed that the pressure amplitude depends on the orientation of the microphone in relation to the acoustic flow, with a change in orientation of 90^o resulting in a pressure difference of 1.6dB for a sound field of intensity 130dB.

Chapter 5

Measurement of acoustic streaming using PIV

This chapter describes the application of PIV to the measurement of acoustic streaming. PIV is firstly used to investigate the influence of high intensity sound fields on acoustic streaming in a cylindrical air-filled tube, and the results compared to theoretical work by Menguy et al. [69]. The acoustic particle velocity inside the tube is also observed to clarify whether the propagation of the sound field itself is affected by non-linear effects.

5.1 Introduction

A sound field propagating through a fluid causes fluid elements to oscillate with acoustic particle velocity. Under certain conditions, it can also generate steady (non-zero time-averaged) motions in the form of vortices, known as acoustic streaming. Acoustic streaming is generally observed in two cases, when the sound field interacts solely with the fluid, and when it interacts with a solid boundary or obstacle suspended within the fluid.

Acoustic streaming can be classified into three types depending on the scale of the streaming motion (see Zarembo [109]):

1. **Schlichting streaming** : vortex motion in the viscous boundary layer surrounding an object suspended in a sound field. The scale of the motion, generally governed by the thickness of the boundary layer, is small relative to the acoustic wavelength.

2. **Rayleigh streaming** : vortex-like motion outside the boundary layer, generated when a standing wave field is present. The scale of the motion is comparable to the acoustic wavelength.

3. **Eckart streaming** : streaming motion induced in a free non-uniform sound field whose scale is large relative to the acoustic wavelength.

It is the study of Rayleigh streaming which is of interest in this present study.

5.1.1 History of acoustic streaming

The phenomenon of acoustic streaming was first noted by Faraday [39] in 1831, when he observed that fine particles lying on a vibrating plate collected at the regions of maximum vibration of the plate. His explanation was that this behaviour resulted from the vibrating plate setting the air near its surface into vibration, causing currents of air to ascend at the vibration antinodes of the plate and descend at the nodes and hence produce the pattern seen. Another early account of acoustic streaming was reported by Dvorak in 1876 (summarised in [5, 86]) when he observed that, in addition to the gas vibrations formed when a standing wave was generated inside a long tube (often referred to as Kundt's tube), non-zero

mean motions of the gas were also present. The gas travelled along the tube walls from the displacement antinode to displacement node, returning in the opposite direction down the centre of the tube from antinode to node to form a closed loop.

The first theoretical analysis of acoustic streaming was made by Rayleigh [85] in 1883, which he later reiterated in "The theory of sound" [86]. By taking successive approximations to the equations governing fluid motion for a viscous fluid, he showed that the streaming arises due to the generation of Reynolds forces, opposed by viscosity, when the sound field is attenuated at a solid boundary. In particular, he noted that the streaming is a second-order effect which occurs due to viscosity. Hence, it is not possible to obtain the acoustic streaming velocity if the acoustic equations are solved to the first approximation alone or the fluid is assumed inviscid. The streamlines predicted by Rayleigh described the streaming observations in Kundt's tube by Dvorak. Rayleigh's initial theoretical work provided a basis which has undergone subsequent development by Eckart [33], Schlichting [89], Westervelt [103], Nyborg [76], Rudenko and Soluyan [88], and others. A detailed experimental investigation of acoustic streaming in a gas-filled tube excited by a standing wave by Andrade [5] in 1931 verified the air circulations predicted by Rayleigh's theoretical work. He used smoke particles as tracing points to visualise the behaviour of flow in the tube, and from this ascertained the amplitude of air vibration. He also observed the vortex motion around cylinders and spheres of varying diameters placed in a cylindrical gas-filled tube acoustically excited by a standing wave. Streaming motion was seen near the surface of the object when the oscillation amplitude reached a critical value, dependent on the object's size. This streaming was later attributed to

boundary-layer effects by Schlichting [89]. Carrière also experimentally investigated the circulation around cylindrical objects, but for amplitudes of oscillation much stronger than those used by Andrade and therefore on a much larger scale relative to the dimensions of the object [19]. The circulations seen were similar to those identified by Andrade, but flowing in the opposite direction. Observations of the directional dependence of the streaming on sound intensity were also made some years later by Ingard and Labate [52] near to small orifices, and by West [102] for oscillating cylinders. Westervelt [103] later clarified that this streaming direction reversal occurs when the amplitude of oscillation is large relative to the dimensions of the object, confirmed in investigations at low and high Reynolds numbers by Andres and Ingard [6, 7].

Theoretical development of Rayleigh's work in 1948 by Eckart [33], and subsequent experimental work by Liebermann in 1949 [63], incited more interest in the phenomena. Eckart showed, by solving the equations of fluid motion through successive approximation with the inclusion of viscous forces, that the streaming motion observed in an acoustic field was generated by the formation of steady vortices. He found that, whilst the forces driving the streaming motion depended on both the coefficients of bulk and shear viscosities of the fluid, the opposing retarding forces depended only on the shear viscosity. He proposed that the bulk viscosity of a fluid, until that point unmeasurable, could be ascertained from measurement of the magnitude of the streaming velocities. Eckart also applied the theoretical analysis to the case of streaming resulting from a high-intensity beam of sound formed by an oscillating quartz crystal, known as "quartz wind", which had been observed by Meissner in 1926 (summarised in [96]).

Following Eckart's work, Liebermann [63] conducted a set of experiments to obtain the bulk viscosity in organic liquids from streaming generated by a beam of sound. Markham [65] extended Eckart's theoretical treatment to include the effects of relaxation, from which he concluded that the magnitude of the streaming does not depend solely on the bulk and shear viscosities, but on the coefficient of sound absorption, which includes effects from thermal relaxation, scattering and heat conduction. This was confirmed in subsequent theoretical and experimental work by various authors [66, 76, 103]. An experimental investigation of acoustic streaming in gases by Medwin [66] showed that, for the case of Argon, the majority of the streaming velocity observed (96 %) could be attributed to the effects of shear viscosity and thermal conductivity alone. Further reviews of acoustic streaming can be found in references [64, 77, 88, 109].

5.1.2 Recent work

Recent discussions of acoustic streaming have addressed two specific issues on the subject: the effects of fluid compressibility and non-linearity. Rudenko and Soluyan [88] were the first to point out that it is insufficient to assume an incompressible fluid in the study of acoustic streaming because the streaming motion arises from acoustic waves propagating through the fluid, which are able to do so only because of its compressible nature. Studies by various authors of acoustic streaming near boundaries [81, 82] have shown that including the effects of compressibility results in a larger predicted streaming velocity outside the boundary layer, and can play an important role in the description of acoustic streaming near rigid boundaries.

The effect of non-linearity on acoustic streaming has been investigated by numerous authors [30, 43, 44, 87]. Classical treatment of acoustic streaming [77, 86, 103], referred to as Rayleigh-Nyborg-Westerwelt (RNW) or slow streaming [64, 109], neglects the effects of inertia of the fluid on the streaming motion, thus limiting its validity to weak acoustic sources. However, it was proposed in 1966 [95] that, for cases where the Reynolds number (the ratio of inertial to viscous forces) is large, the fluid inertia must be considered in the equations describing the fluid motion; this is often referred to as nonlinear streaming. Lighthill [64] points out that this generally applies to all forms of perceptible streaming.

Recent theoretical work by Menguy [68, 69] on acoustic streaming generated by a sinusoidal standing wave inside a cylindrical waveguide, predicts that the non-linear effect of fluid inertia will distort the streaming pattern observed. This study is concerned with the experimental investigation of non-linear effects found inside a tube under similar conditions to those presented by Menguy.

The present work is concerned with the streaming motion observed when a standing wave is set up in a cylindrical tube, otherwise known as Rayleigh streaming. In order to fully understand the streaming patterns predicted and observed, a summary of the equations describing Rayleigh streaming formed in a cylindrical tube is given in the next section.

5.2 Derivation of streaming equations

This section outlines the derivation of the equations describing acoustic streaming using the method of successive approximations, which is explained in more detail

in reference [77].

Consider a viscous, compressible fluid, whose motion is governed by the continuity equation (5.1) and Navier-Stokes equation (5.2):

$$\frac{\partial \rho}{\partial t} + \nabla \cdot (\rho \mathbf{u}) = 0 \tag{5.1}$$

$$\rho \left(\frac{\partial \mathbf{u}}{\partial t} + \mathbf{u} \cdot \nabla \mathbf{u} \right) = -\nabla p + \mu \nabla^2 \mathbf{u} + \left(\mu' + \frac{1}{3}\mu \right) \nabla (\nabla \cdot \mathbf{u}), \tag{5.2}$$

where p is the hydrostatic pressure, μ and μ' are the coefficients of shear viscosity and bulk viscosity respectively, and $\mathbf{u}$ is the fluid velocity vector.

Using the continuity equation (5.1) and the vector identity $\nabla \times (\nabla \times \mathbf{u}) = \nabla \nabla \cdot \mathbf{u} - \nabla^2 \mathbf{u}$, the Navier-Stokes equation (5.2) can be re-expressed as :

$$\frac{\partial (\rho \mathbf{u})}{\partial t} + F_1 = -\nabla p + \left(\mu' + \frac{4}{3}\mu \right) \nabla (\nabla \cdot \mathbf{u}) - \mu \nabla \times (\nabla \times \mathbf{u}), \tag{5.3}$$

where

$$F_1 = \rho (\mathbf{u} \cdot \nabla) \mathbf{u} + \mathbf{u} \nabla \cdot (\rho \mathbf{u}). \tag{5.4}$$

As noted by Rayleigh [86], since acoustic streaming is a second-order effect, in order to study its motion it is necessary to solve these equations to higher approximations than those describing linear propagation of sound.

First, the variables p, ρ and $\mathbf{u}$ are represented by:

$$\begin{aligned} p &= p_0 + p_1 + p_2 + \cdots \\ \rho &= \rho_0 + \rho_1 + \rho_2 + \cdots \\ \mathbf{u} &= 0 + \mathbf{u}_1 + \mathbf{u}_2 + \cdots \end{aligned} \tag{5.5}$$

where the order of each term is denoted by the indexes. Here, p_0 and ρ_0 are the equilibrium pressure and equilibrium density respectively in the absence of the sound field. p_1, ρ_1 and $\mathbf{u}_1$, which are the first-order approximations to the steady-state solutions of equations 5.1 and 5.3, vary sinusoidally in time with frequency ω and thus represent the sound field in the linear approximation. The second-order approximations, p_2, ρ_2 and $\mathbf{u}_2$, contain periodic terms of frequency 2ω and, more interestingly, time-independent terms which describe the streaming motion.

It is also necessary to include a term representing the relaxation mechanisms, which Markham [65] showed to be as important as the viscous terms. This is done by modifying the equation of state relating the first-order pressure and density by $p_1 = c^2\rho_1$ to

$$p_1 = c_s^2\rho_1 + R_r\frac{\partial}{\partial t}\rho_1, \tag{5.6}$$

with c_s, the speed of the propagating sound wave and R_r, a frequency-dependent constant representing the effects due to the relaxation mechanisms for a pressure varying sinusoidally with time.

Substituting the equations in 5.5 into the continuity equation (5.1) and Navier-Stokes equation (5.3), and using equation 5.6, expressions can then be obtained containing terms of equal order. Equating terms of first-order gives:

$$\frac{\partial\rho_1}{\partial t} + \rho_0\nabla\cdot\mathbf{u}_1 = 0 \tag{5.7}$$

$$\rho_0\frac{\partial\mathbf{u}_1}{\partial t} = -c_s^2\nabla\rho_1 + \left(\mu' + \frac{4}{3}\mu + R\rho_0\right)\nabla\nabla\cdot\mathbf{u}_1 - \mu\nabla\times(\nabla\times\mathbf{u}_1). \tag{5.8}$$

Similarly, the second-order equations are:

$$\frac{\partial \rho_2}{\partial t} + \rho_0 \nabla \cdot \mathbf{u}_2 + \nabla \cdot (\rho_1 \mathbf{u}_1) = 0 \tag{5.9}$$

$$\frac{\partial}{\partial t}(\rho_0 \mathbf{u}_2 + \rho_1 \mathbf{u}_1) + F_2 = -\nabla p_2 + \left(\mu' + \frac{4}{3}\mu\right) \nabla \nabla \cdot \mathbf{u}_2 - \mu \nabla \times (\nabla \times \mathbf{u}_2), \tag{5.10}$$

where

$$F_2 = \rho_0 \left[(\mathbf{u}_1 \cdot \nabla)\mathbf{u}_1 + \mathbf{u}_1(\nabla \cdot \mathbf{u}_1)\right]. \tag{5.11}$$

Assuming that it is only the steady solution to the streaming velocity $\mathbf{u}_2$ which is of interest, equations 5.10 and 5.11 can be simplified by taking the time-average over a period for each term to give:

$$\langle F_2 \rangle = -\nabla \langle p_2 \rangle_t + \left(\mu' + \frac{4}{3}\mu\right) \nabla \nabla \cdot \langle \mathbf{u}_2 \rangle_t - \mu \nabla \times (\nabla \times \langle \mathbf{u}_2 \rangle_t), \tag{5.12}$$

where

$$\langle F_2 \rangle = \rho_0 \langle (\mathbf{u}_1 \cdot \nabla)\mathbf{u}_1 + \mathbf{u}_1(\nabla \cdot \mathbf{u}_1) \rangle. \tag{5.13}$$

Finally, the first order solution $\mathbf{u}_1$ is obtained by solving equations 5.7 and 5.8 using suitable boundary conditions. The solution to $\mathbf{u}_1$ is then used in equation 5.12, which is solved to find the second-order approximation $\mathbf{u}_2$.

5.3 Solutions to the acoustic streaming equations in a cylindrical tube

The main part of this study is concerned with the investigation of one particular type of streaming, namely Rayleigh streaming. Rayleigh streaming, which occurs when an acoustic standing wave suffers dissipation in the boundary layer of a surface, is most commonly observed when a standing wave is set up inside a narrow cylindrical tube. Rayleigh [85, 86] was the first to derive and solve equations for the streaming motion generated in a viscous fluid between two parallel plates by a standing wave using the method of successive approximations detailed in section 5.2. More recently, his solutions have been modified to include various corrections by numerous authors [77, 88, 94, 109].

5.3.1 Rayleigh streaming

Consider the case of a standing wave of angular frequency ω and acoustic wavelength λ in a cylindrical air-filled tube of length L and radius a, where the main axis of the tube is aligned along the x-axis and the width of the tube along the y-axis. The acoustic particle velocity of the sound field is given by equation 2.12.

In accordance with Rayleigh, Nyborg and others [77, 85, 88, 109], the time-averaged first and second-order equations describing the fluid motion are derived using the method of successive approximations discussed in section 5.2. For these derivations, it is assumed that the wavelength is large compared to the diameter of the tube $2a$. Also, the boundary layer thickness δ_v, given by equation 2.31, is small compared to both λ and $2a$ such that the effects of viscosity are confined to

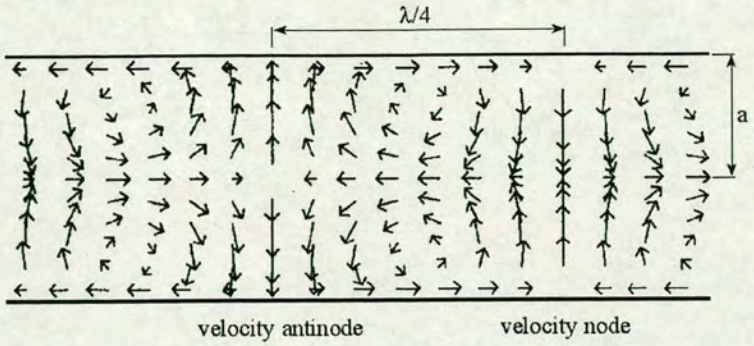

Figure 5.1: Rayleigh streaming in a cylindrical tube of radius a (adapted from [91]).

a small width adjacent to the tube walls. Using appropriate boundary conditions at the position of the tube walls, and assuming a no-slip condition at the walls of the tube, the first-order velocities are found and consequently used to solve the second-order equations. The second approximation yields the result that in the main acoustic field (outside the boundary layer), the axial and radial components of the streaming velocity u_{sx} and u_{sr} respectively, are described by:

$$u_{sx} = \frac{-3|u_a|^2}{8c} \sin 2kx \left[1 - 2\left(\frac{r}{a}\right)^2\right] \tag{5.14}$$

$$u_{sr} = \frac{3|u_a|^2}{8c} kr \cos 2kx \left[1 - \left(\frac{r}{a}\right)^2\right] \tag{5.15}$$

where r is the radial distance measured from the axis of the tube and c is the speed of sound. The resulting streaming pattern, as calculated by Rayleigh, is shown in figure 5.1.

As can be seen, the streaming behaviour is axi-symmetric, with vortices present either side of the central axis spaced at intervals of $\lambda/4$. There is a

steady flow along the tube walls directed towards the velocity nodes of the standing wave, which returns along the central axis of the tube to complete a closed loop. From equation 5.14, we see that the component of the streaming along the x-axis is zero at $r = a/\sqrt{2}$.

Qualitatively, the vortices seen in figure 5.1 are formed due to the interaction of the flow with vortices in the boundary layer [109]. A sound wave propagating along the tube produces a large velocity gradient in the boundary layer due to the no-slip boundary condition at the inner wall surface. The momentum of the sound wave will therefore vary sharply in the boundary layer, generating large forces called Reynolds stresses. These produce contra-rotational vortices just outside the boundary layer, whose motion depends on many parameters including the intensity of the sound field and the tube diameter.

It is noted that the streaming velocities given in equations 5.14 and 5.15 do not depend on the viscosity of the fluid. The streaming velocity u_s at a specific point can be predicted by measuring the pressure at that point and then using equation 2.11 to deduce the acoustic particle velocity amplitude $|u_a|$. This is then substituted into equations 5.14 and 5.15.

5.4 Non-linear acoustic streaming

Recently, a theoretical investigation of acoustic streaming at high sound levels in a cylindrical waveguide has been conducted by Menguy [68, 69]. Equations 5.1 and 5.2 governing the fluid motion in the boundary layer and, separately, in the main acoustic field, were set dimensionless using the acoustic Mach number

M and Shear number Sh. Using a perturbation method involving asymptotic expansions, followed by time-averaging of each term, the equations describing the streaming behaviour were derived. Menguy found that inside the acoustic boundary layer, inertial effects remain negligible even at high sound levels, an expected result due to the large viscous forces present. In the main acoustic field, a non-linear term due to the fluid inertia appears in the equations for the streaming velocity field. Its effect is determined by the value of the Reynolds number Re_{nl}, defined for this particular investigation by Menguy as $Re_{nl}=M^2/Sh^2$ (which compares inertia and viscosity but is different from the Reynolds number Re_s defined by Stuart [95]), and is only considered negligible for $Re_{nl} \ll 1$ when the slow streaming approximation becomes valid. By comparing the nonlinear and slow acoustic streaming, he predicted that, as Re_{nl} increases, the effects of fluid inertia would cause the toroidal vortex pattern to become increasingly unsymmetrical, as illustrated in figure 5.2(a). Also, the axial component of the streaming velocity along the x-axis, which is sinusoidal for weak acoustic sources, would become more and more distorted, as shown in figure 5.2(b).

It should be noted that, although the graphs in figure 5.2 only display data up to a Reynolds number of 4, theoretical predictions [41, 69] extend to higher Reynolds numbers (Re_{nl}=6).

Recent experimental work by Sharpe et al. [91] and Arroyo and Greated [8], shows the streaming pattern as predicted by Rayleigh. However, this work does not comment on non-linear distortion of the streaming motion at higher intensity levels where non-linear streaming is predicted to occur.

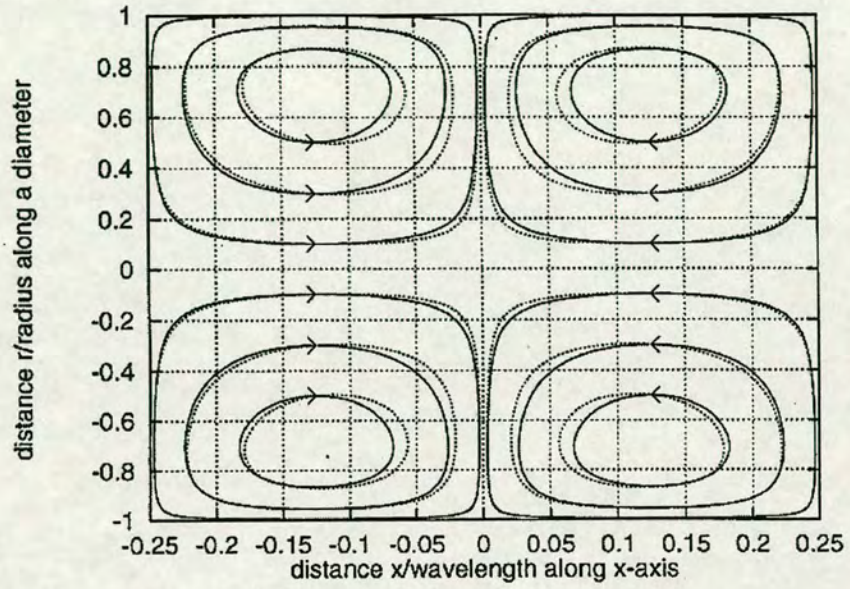

(a)

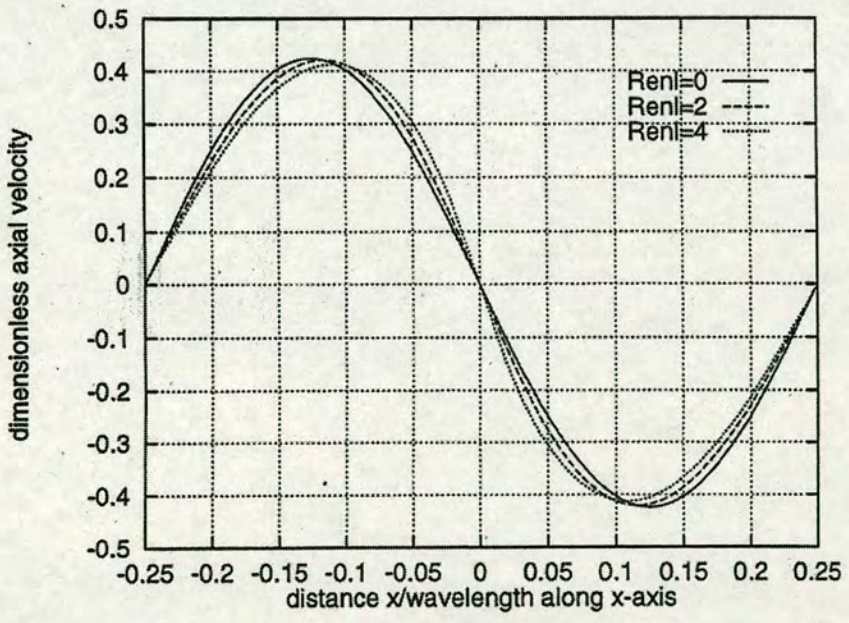

(b)

Figure 5.2: (a) Streamlines on a longitudinal section of the tube between two velocity nodes for Re_{nl}=0(–) and Re_{nl}=4(···) and (b) Dimensionless axial streaming velocity ($/M^2c_0$) on a longitudinal section of the tube between two velocity nodes for Re_{nl}=0, Re_{nl}=2 and Re_{nl}=4 (theoretical predictions by Menguy [69]).

The aim of this experimental work is to investigate the effects of non-linearity on the acoustic streaming experimentally and compare the results to the predictions of Menguy. The following sections discuss the application of PIV to the measurement of acoustic fields in two cases. In the first case, PIV is used to investigate acoustic streaming in a cylindrical air-filled tube under the influence of intense sound fields. These results are compared to theoretical work by Menguy [68, 69]. Secondly, observations of the acoustic particle velocity are made in order to determine whether the sound field propagation is affected by non-linear effects.

5.5 Preliminary investigation of acoustic streaming

5.5.1 Introduction

The initial aim of this work was to reproduce the acoustic streaming motion observed by Sharpe et al. and Arroyo and Greated [91, 8]. Preliminary observations and measurements were made to determine the problems associated with acoustic streaming.

Measurements were performed using the experimental arrangement shown in figure 5.3, with the PIV set-up as described in section 4.3.2 and illustrated in figure 4.4. Initial measurements were performed inside a cylindrical glass tube of length 614mm, wall thickness 2mm and internal radius 13.25mm, which was mounted vertically. However, for later experiments, a shorter tube of length 532mm was used. The acoustic field was generated inside the tube using a JBL

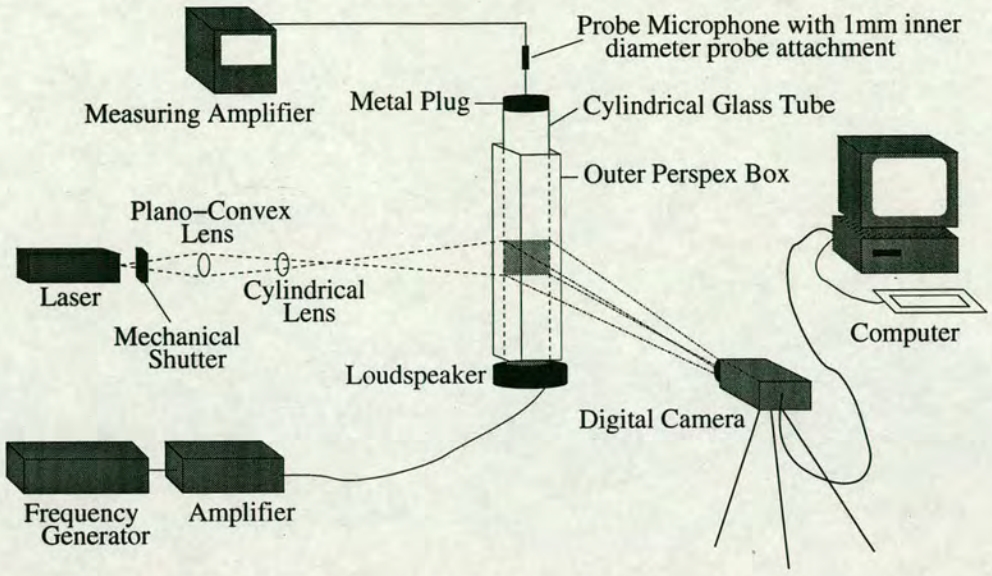

Figure 5.3: Experimental arrangement for taking PIV measurements of acoustic streaming inside a closed-end tube.

2446H 8Ω compression driver driven by an amplified sinusoidal output from a Stanford sine-wave generator. The loudspeaker was connected to the bottom of the tube by means of a flange, with an inset o-ring to reinforce the seal.

A burning incense stick was held just inside the top of the tube for a few seconds to generate smoke particles inside the tube, and the tube was then sealed by a metal plate to provide a rigid termination for the standing wave. The loudspeaker was driven at a frequency of 1975Hz, corresponding to the 7th resonance mode of the tube. The B&K short probe microphone described in section 4.5 was inserted through the centre of the metal plate such that the tip of the probe was flush with the wall of the plate inside the tube. The pressure amplitude at the rigid termination, corresponding to a pressure maximum under resonance conditions, was increased to a sound pressure level of 145-155dB (re 20μPa), the regime where acoustic streaming is visible.

The optically expanded light sheet from the laser was projected through the tube axis to enable visualisation of the streaming motion. Image pairs were then taken with a separation of 20-30ms, depending on the intensity of the sound field, corresponding to a particle displacement between the first and second images of approximately 1-8 pixels.

5.5.2 Results and discussion

Initial observations of the streaming motion highlighted a number of problems:

1. Unstable streaming motion
2. Non-symmetrical streaming pattern across the width of the tube
3. Unequally sized vortices along the length of the tube

The streaming motion was initially very unstable, with vortex motion unclearly defined. Literature research showed that various authors had observed severe distortion of the streaming motion due to significant convective currents around the outside of the tube [5, 91]. A perspex tube was therefore placed around the outside of the tube to restrict air motion and hence improve thermal lagging. With careful sealing between the two tubes at both ends, the streaming pattern stabilised and the streaming motion illustrated in figure 5.4 was seen.

It is clear from the photo in figure 5.4 that the streaming motion is unsymmetrical about the axis of the tube. Instead of seeing two equally-sized vortices side by side, as illustrated in figure 5.1, the vortex on the left side of the tube is more dominant. Without the sound field present, it became obvious that this

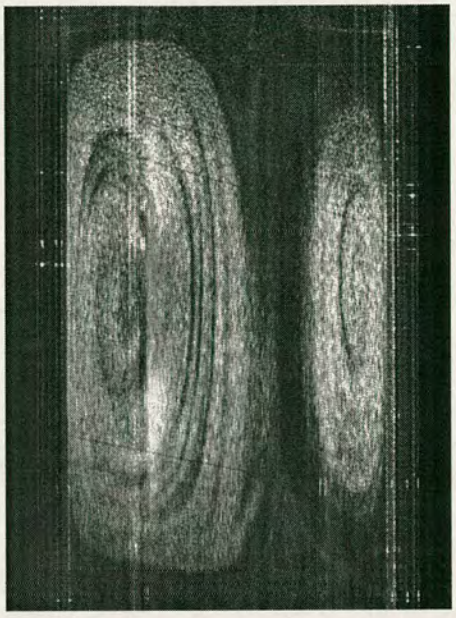

Figure 5.4: Photographic image of unsymmetrical Rayleigh streaming due to additional air circulation inside the tube.

unsymmetrical pattern was largely due to a mean current circulation travelling up the left-hand side of the tube and down the right-hand side. This appeared to be a result of air leaking in at both the top and bottom of the tube due to insufficient sealing measures. It was, however, unclear whether the unequally sized vortices along the length of the tube were a consequence of this circulation.

Due to the susceptibility of the streaming motion to convective air currents both inside and outside the tube, the connection between the loudspeaker and tube was changed to the arrangement described in section 4.2. Additionally, the rigid termination of the tube was changed to an aluminium plug with two inset o-rings to create a good seal, as illustrated in figure 4.2, effectively shortening the length of the tube to 595mm.

Adjusting the frequency of the sound field to set up a standing wave, a more stable and symmetrical streaming pattern was obtained, as shown in the image in

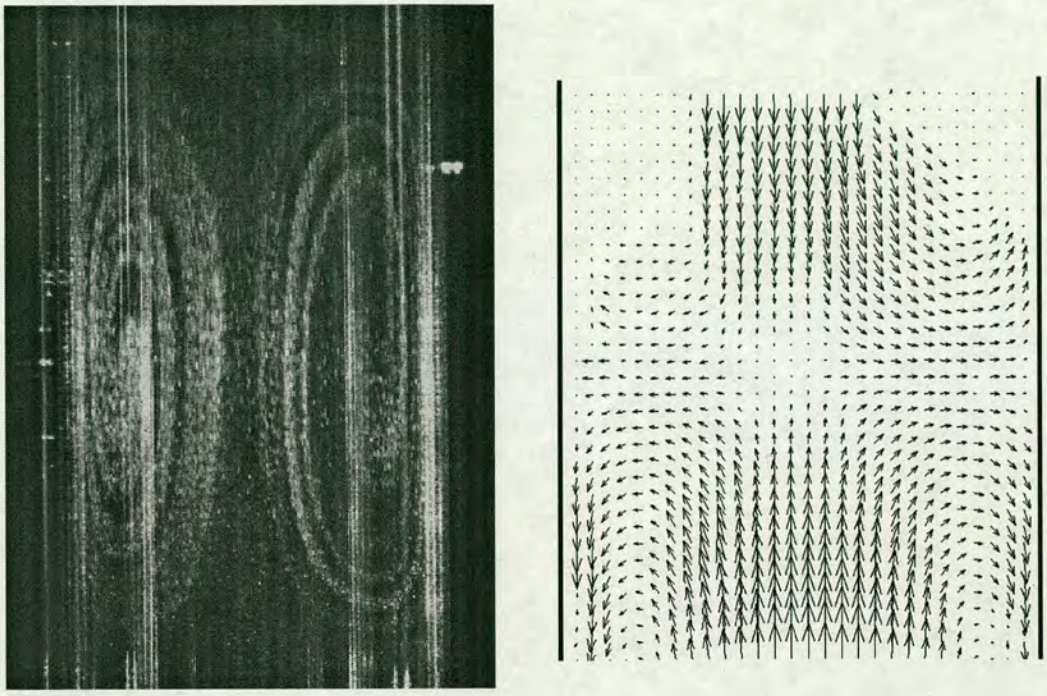

(a) (b)

Figure 5.5: (a) Photographic image of acoustic streaming in the cylindrical tube and (b) a PIV velocity map taken at a velocity antinode.

figure 5.5(a). This particular image, which was taken before the seeding particles had equilibrated in the tube in order to observe the streamlines of the streaming motion, clearly shows a steady flow moving along the central axis and returning along the tube walls to complete the loop. As can be seen from figure 5.5(a), some parts of the image do not contain clear particle images and hence will not yield velocity measurements, particularly near to the tube walls; this is due to flare from the walls of the tube and uneven seeding. Flare is a notorious problem in PIV measurements, particularly when working in gas mediums. It can be caused by inhomogeneous particle distribution, due to clusters of particles scattering more light than individual particles. Additionally, as can be seen in

figure 5.5(a), the light sheet passing through the curved surface of the cylindrical tube produces internal reflections and hence vertical lines near the tube walls. Although this means that when working with cylindrical tubes the slip velocity at the tube walls cannot easily be measured, it does not affect observations of the particle displacement along the central axis. This is the main requirement for observing and measuring non-linear effects on the acoustic streaming, as will be described in section 5.6.1. Once the seeding was more homogeneous, pairs of images were taken and cross-correlated, as described in Chapter 3, to produce a velocity vector map. The velocity map taken at a velocity antinode at an intensity level of 149.5dB is shown in figure 5.5(b). As can be seen, the streaming motion appears to be slightly asymmetric, with slightly broader vortices on the right hand side of the tube than on the left. This effect is probably due to convective currents outside the tube.

In order to check the validity and accuracy of these measurements, the axial streaming velocity profile across the tube width was determined from the velocity vector map shown in figure 5.5(b). From equation 5.14, the velocity profile across any section of the tube should be parabolic with a maximum on the tube axis ($r = 0$) and zeros at a distance $r = a/\sqrt{2}$ from the tube axis. Hence, axial velocities were extracted along three separate lines across the width of the tube, and theoretical curves fitted to each set of points using the measured maximum velocity and theoretical zero points from equation 5.14, as presented in figure 5.6.

As can be seen, good agreement is found between the experimental measurements and the theoretical curves in the central region of the tube to within 10% of the expected value. The velocities appear to be slightly higher than expected to the left of the tube axis, reflecting the asymmetry of the streaming pattern noted

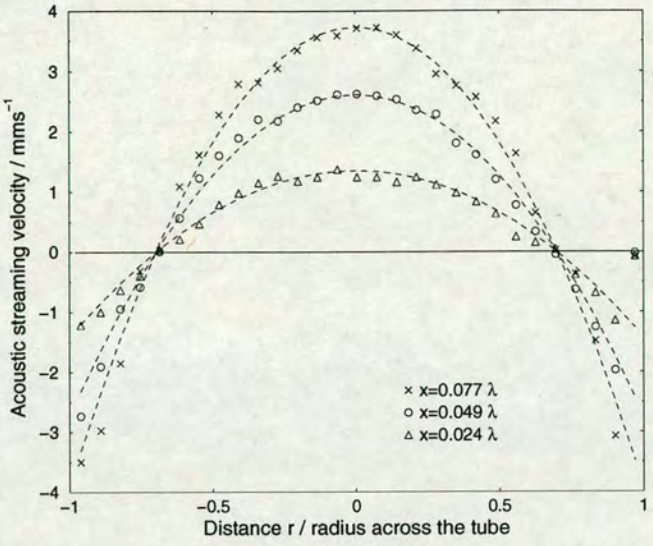

Figure 5.6: Axial velocity profile across the width of the tube at three positions of distance x from the acoustic velocity antinode. Experimental results (symbols) are compared with theoretical values (dotted lines).

earlier. A larger discrepancy between the theoretical and experimental results is seen in the outer regions of the tube between the zero velocity points and the tube walls; this is expected due to the increased error in the PIV measurements near the tube walls resulting from the flare on the PIV images.

Having demonstrated that this method could be used to accurately reproduce previous work, the study of acoustic streaming was then extended to investigate non-linear effects. As is discussed in the following sections, these results were then compared to theoretical work by Menguy et al. [68, 69].

5.6 Investigation of non-linear effects on acoustic streaming

For the remaining acoustic streaming measurements, a shorter glass tube of internal radius 13.25mm and length 532mm (513mm when closed with the metal plug) was used. In order to decide which frequencies to work at, the resonance frequencies of the closed-tube system were determined. The probe microphone was positioned at the end of the tube as described in section 5.5.1. Controlled by a PC and using the same software used to calibrate the probe microphone (see section 4.5.1), the frequency of the acoustic field produced by the loudspeaker was stepped up in 5Hz intervals from 50 to 2500Hz. The output signal from the conditioning amplifier was sampled by the Wavebook A/D converter, and analysed using software developed by Cullen [23].

The resulting frequency response curve is shown in figure 5.7. The dotted vertical lines represent the theoretical resonance frequencies of the tube assuming the end of the tube terminated by the loudspeaker acts as an open end. As can be seen, most of the resonance peaks are aligned close to the vertical lines, indicating that the loudspeaker termination behaves similar to that of an open end. This result is probably due to the fact that the acoustic field generated by the loudspeaker opens up into a reasonably large volume before being channelled into the end of the tube (see figure 4.1). Hence, the end of the tube is primarily terminated by an open rather than a closed end.

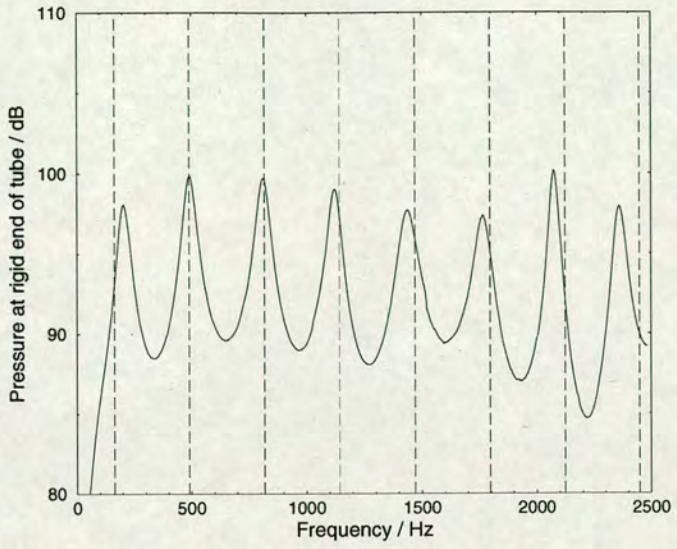

Figure 5.7: Anti-nodal pressure amplitude for the loudspeaker-tube system terminated by a rigid end. The dotted lines correspond to theoretical resonances of a tube terminated at one end and open at the other.

It was decided to investigate acoustic streaming at frequencies corresponding to the 6th and 7th resonant modes of the tube (i.e $\sim$1780Hz and $\sim$ 2090Hz) for two main reasons:

1. As detailed in section 4.3.2, the light sheet used to visualise the streaming motion was restricted to illuminating a plane 50mm wide. In order to investigate non-linear effects on the acoustic streaming motion, it was necessary to capture both a velocity node and antinode in the same image so that the mid-point between the two nodal points was known. As can be seen from figure 5.2(b), the position of the maximum axial velocity is predicted to become increasingly displaced from this point with increasing sound intensity due to non-linear effects. For the length of tube chosen, this restricted measurements to resonance frequencies at or above the 6th resonance mode.

2. The cut-off frequency of the tube, the critical frequency above which undesirable higher modes can propagate [40], was calculated to be 7.5kHz. Fourier analysis of the pressure signal at the first pressure antinode inside the tube showed that the level of the second harmonic, which was much stronger than the levels of the higher harmonics, increased relative to the fundamental with increasing sound intensity and also with increasing frequency. At 154dB (sound field frequency = 2070Hz), the amplitude of the second harmonic was 50% of the amplitude of the fundamental. Hence, it was decided to restrict the frequency to less than half the cut-off frequency to reduce the risk of higher mode propagation of the second harmonic. The contribution of higher harmonics is considered further in section 5.6.2.

5.6.1 Effect of high intensity sound fields on acoustic streaming

Experimental method

The modified experimental apparatus was arranged as described in section 5.5.1 and illustrated in figure 5.3, with a shorter glass tube of internal radius 13.25mm and length 532mm. Incense smoke was introduced into the top of the glass tube and the end sealed with the metal plug. A 2080Hz standing wave was set up in the tube, and the sound field intensity at the rigid end of the tube monitored by the short probe microphone. Measurements were made for sound field intensities at the rigid end of the tube in the range 145-154dB (re 20μPa), corresponding to a Reynolds number of Re_{nl}=1.9 to Re_{nl}=15.3.

Once the seeding appeared to be homogeneous and the streaming motion had stabilised, the light sheet was projected through the tube axis and the streaming particle displacement recorded by the cross-correlation camera, as described in section 4.3.2. Each pair of exposures had a pulse width of 4-6ms and separation 20-30ms, depending on the intensity of the sound field and hence the velocity of the streaming motion being measured. The PIV measurements were taken in the central region of the tube to avoid end effects from the tube. In order to assess the effect of sound field intensity on the acoustic streaming motion, measurements were repeated at various sound pressure levels, and at several points along the tube by moving the camera vertically. When moving the camera (in the latter case), care was taken to slightly overlap each set of images so that their corresponding positions could be identified during analysis. Once cross-correlated, the respective velocity maps could then be translated to their relative positions to produce a full-length, continuous velocity map. Each pair of images was then cross-correlated using a 32 $\times$ 32 pixel interrogation area with a 50% overlap to determine the average particle displacements. The physical particle displacement was then calculated by relating the number of pixels across the tube to the known tube diameter. This, together with the time lapse between exposures, was then used to calculate the acoustic streaming velocity.

Results

Figure 5.8 presents photos of the streaming motion between two adjacent velocity antinodes, taken at a frequency of 2080Hz for two different sound pressure intensity levels. At 151dB (figure 5.8(a)), each toroidal vortex appears to be relatively symmetrical. However, at 154dB (figure 5.8(b)) the vortex shape has become very unsymmetrical. Comparison with the predicted change in vortex

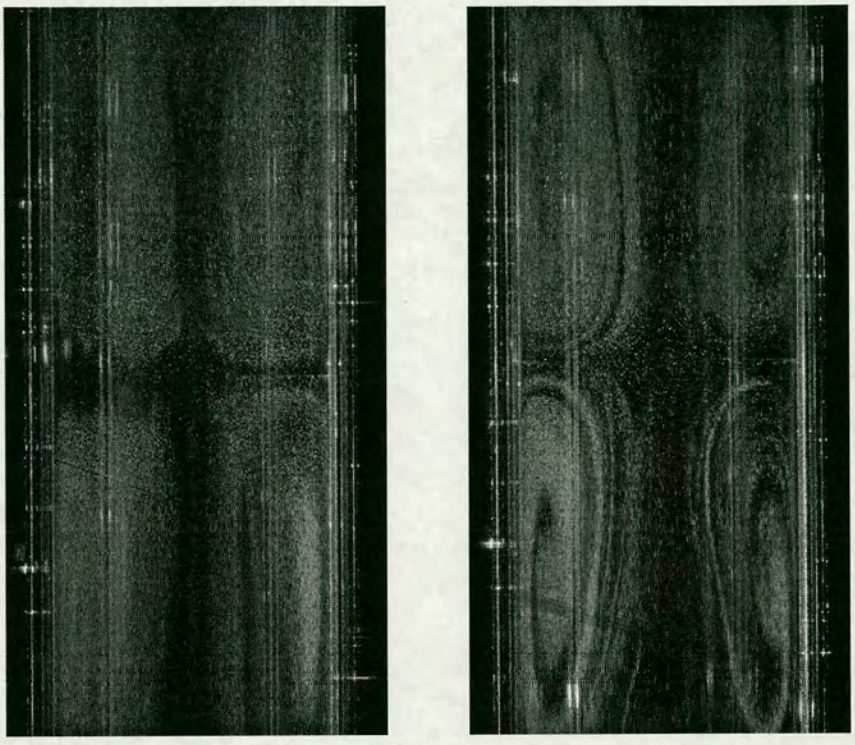

(a) (b)

Figure 5.8: Streaming motion between two velocity antinodes for sound pressure levels of (a) 151dB (Re_{nl}=7.7) and (b)154dB (Re_{nl}=15.3).

shape by Menguy (figure 5.2(a)) shows that the distortion occurs in the opposite direction to predictions. In figure 5.2(a), for high Reynolds numbers the vortices are wider at the velocity antinode and taper down towards the node. However, the experimental results show the vortices being wider at the velocity node and tapering down towards the antinode.

Figure 5.9 shows a velocity map from velocity antinode to node, produced by matching up images taken at different vertical positions and then translating each velocity map to its relative position.

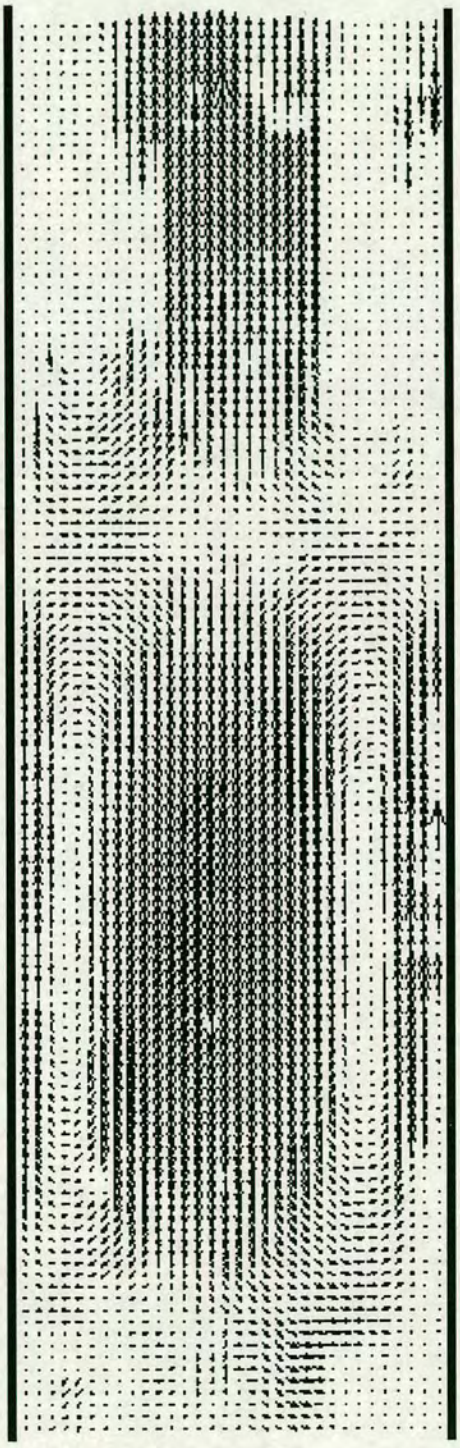

Figure 5.9: Velocity profile of the cylindrical tube from a velocity antinode (bottom) to node (top).

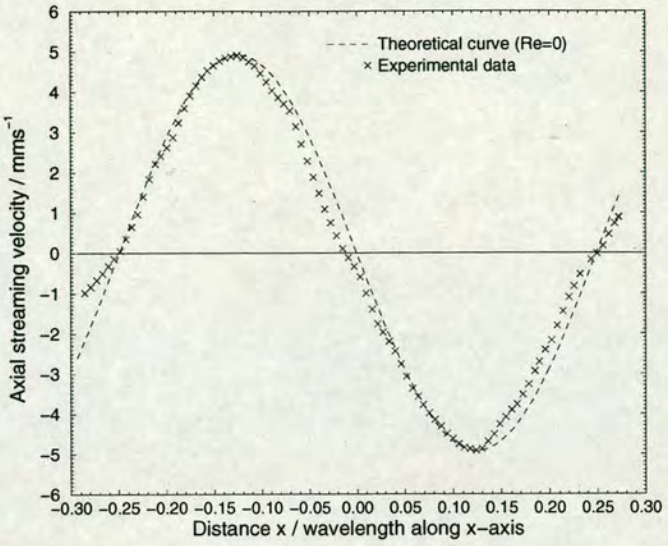

Figure 5.10: Axial velocity profile between two velocity nodes for a standing wave of 1786Hz and acoustic level of 149.5dB, measured at the rigid end of the tube.

In order to investigate the predictions of non-linear effects of fluid inertia in high-intensity acoustic fields on the axial component of the streaming velocity, points were extracted from the unvalidated vector maps and used to plot an axial velocity profile with distance along the tube. Figure 5.10 shows the axial streaming velocity profile between two velocity nodes for an acoustic level of 149.5dB, corresponding to a Reynolds number Re_{nl}=4.6. The theoretical curve for Re_{nl}=0 (sinusoidal dependence) was fitted using the measured velocity maximum and velocity node points. The experimental results lie reasonably close to the sinusoidal curve, though the position of the velocity antinode is shifted to the left of the expected position, reflecting the asymmetry along the length of the tube mentioned in section 5.5.2. Due to the unequal spacing of the velocity nodes and antinodes, it is difficult to conclude whether there is any deviation from the sinusoidal curve due to non-linear effects. From equations 5.14 and 2.11, there is a small discrepancy of u_s=0.34mm s^{-1} (equivalent to 0.4dB) between the measured

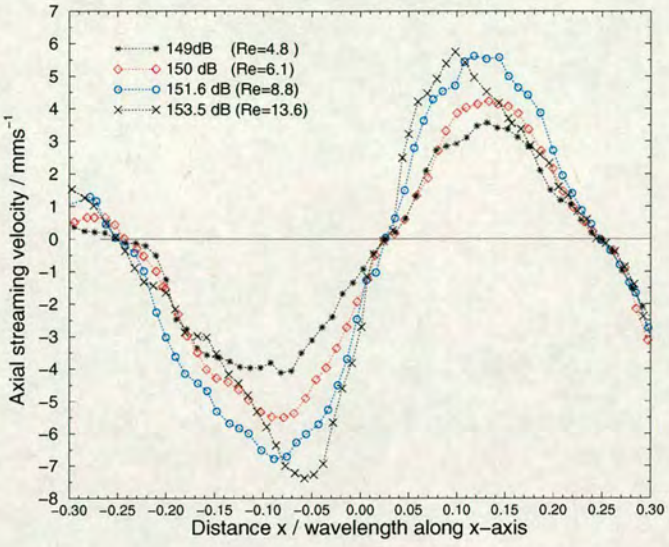

Figure 5.11: Axial velocity profile between two velocity antinodes for a standing wave of frequency 2080Hz for four different acoustic levels.

streaming velocity and expected value calculated from the pressure at the end of the tube. This could be partially attributed to attenuation of the pressure amplitude at the closed end of the tube.

In figure 5.11, axial streaming velocity profiles between two velocity antinodes for four different acoustic levels from 149 to 153.5dB, corresponding to Reynolds numbers of Re_{nl}=4.8 to Re_{nl}=13.6, are shown. The on-axis streaming velocity clearly deviates from sinusoidal dependence as the sound field intensity increases. However, comparison with figure 5.2(b) shows that the direction of the deviation opposes theoretical predictions, with the positions of the velocity maximum and minimum deviating towards the velocity node rather than the velocity antinode. As observed previously, the zero velocity points are not equally spaced, with the displacement between adjacent velocity nodes and antinodes larger when the on-axis streaming motion is directed towards the loudspeaker. The streaming pattern is noticeably distorted for acoustic levels below 150dB (when the con-

secutive vortices are very unsymmetrical) but becomes more symmetrical with increasing intensity level up to $\approx$ 154dB. The difference in displacements, usually 1-4mm ($\leq$10% of the vortex length), is significant compared to the deviation from sinusoidal dependence predicted at high Reynolds numbers. Hence, it is difficult to compare the results directly to theory unless the acoustic streaming pattern is completely symmetrical. The peak amplitudes of the on-axis streaming velocities are also unequal, with the velocity in the direction of the loudspeaker consistently higher. Calculations using equations 5.14 and 2.11 show that for Re_{nl}=6.1 and Re_{nl}=8.8, there is a discrepancy of u_s=0.4mm s^{-1} between the amplitude of the axial streaming velocity towards the loudspeaker and the expected value from the pressure measurements, as seen in figure 5.10. For Re_{nl}=13.6, the measured amplitude is 4mm s^{-1} smaller than expected.

Since the non-linear distortion of the streaming motion due to fluid inertia has only been calculated by Menguy et al. for $Re_{nl}\leq$6 [69], it is unclear whether the distortion at higher Reynolds numbers is expected to continue in the same direction. Regardless of this, the results indicate that additional forces are present in the tube for Reynolds numbers less than 6 which are causing the streaming pattern to become distorted in a similar manner to that predicted, but in the opposing direction. Repeated measurements confirmed the validity of this result. Observations of the streaming motion and related discussions [41] point towards two possible sources; non-harmonic acoustical pressure in the tube or effects due to collation of smoke particles. The next two sections are dedicated to the investigation of the source of the distortion.

5.6.2 Effect of harmonic distortion on acoustic streaming

Whilst taking PIV measurements, non-linear behaviour was clearly observed at velocity nodes in the streaming pattern, as shown in the photographic image in figure 5.12.

At velocity nodes and antinodes, the streamlines should be straight across the width of the tube. However, whilst this is true at the velocity antinode (located at the middle of the image), the streamline is curved around the central axis at the velocity node (seen at the top of the image). This indicates some form of distortion in the sound field .

Investigation of harmonic content of signal

The long probe microphone was lowered into the tube through the metal plug and positioned at the first velocity node from the end of the tube, indicated by a maximum pressure signal on the microphone amplifier. The amplified output voltage from the Brüel and Kjær amplifier was sampled by the Wavebook A/D converter and saved as a .wav file. Similar measurements were repeated at the velocity antinode. A standard signal analysis program, which performs a Fourier analysis on signals to identify the separate harmonic components, was then applied to the sound files and used to extract the pressure amplitudes of the different harmonics. The pressure amplitudes for the first four harmonics of a 2070Hz standing wave, for two different acoustic levels measured at the rigid end, are shown in table 5.1.

At the velocity node, the fundamental harmonic dominates with the amplitude of the 2nd harmonic increasing relative to the fundamental with increasing sound intensity levels. At 150dB, the amplitude of the second harmonic is 10dB lower

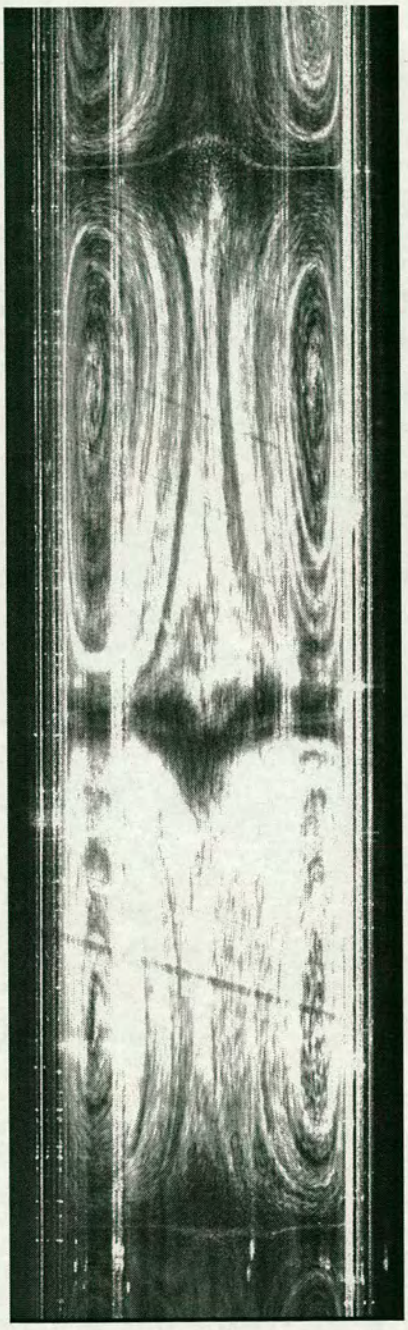

Figure 5.12: Photographic image of non-linear distortion at the velocity node (top of the image).

Position	Sound Intensity Level (dB)	Harmonic Components (dB)			
		1st	2nd	3rd	4th
Velocity antinode	150	76	90	43	37
Velocity node	150	90	80	36	41
Velocity antinode	154	78	90	45	40
Velocity node	154	90	84	49	54

Table 5.1: Amplitude of the first four harmonics (in decibels) at the first velocity node and velocity antinode away from the rigid termination of the tube, for two intensity levels measured at the rigid end of the tube. The same reference level (90dB) is used for the highest component in each case.

than that of the fundamental which, using equation 2.4, corresponds to a pressure amplitude 32% of that of the fundamental harmonic. At 154dB, this difference reduces to 6dB, equivalent to an amplitude 50% of that of the fundamental. At the velocity antinode, the amplitude of the second harmonic is larger than the fundamental in both cases. As can be seen, the amplitudes of the higher harmonic components are too small to have any significant effect, and can therefore be neglected.

As can be seen from the diagram in figure 5.13 showing the axial streaming velocities for the first and second harmonics and the resulting multi-harmonic streaming velocity, the second harmonic component in the signal could in theory be partially responsible for the distortion observed. Each velocity antinode of the fundamental harmonic corresponds to a node of the second harmonic. Hence, should the amplitude of the second harmonic be significant compared to that of the fundamental, the slope of the resulting axial velocity will be increased at the streaming velocity node and decreased at the streaming velocity antinode. Thus, there is competition between the effect of the non-linear streaming of the

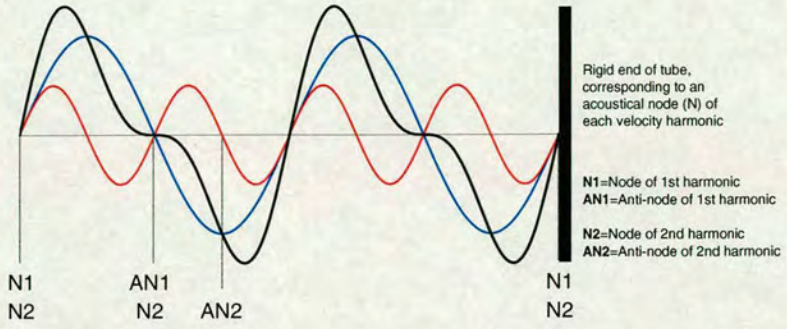

Figure 5.13: Diagram of the axial streaming velocity profile for a standing wave in a closed-end tube, showing contributions from the fundamental harmonic (blue line), second harmonic (red line) and the resulting multi-harmonic signal (black line).

fundamental and the linear streaming of the second harmonic. Calculations by Menguy [41, 69] to compare these two effects showed that for a typical sound field with Re_{nl}=5 (149dB for an acoustic field of frequency 2070Hz), the non-linear streaming effect is compensated by a second harmonic 8.8dB below the fundamental.

Although the measurements in table 5.1 suggest that the amplitude of the second harmonic is not quite large enough to mask the nonlinear streaming effect at least up to levels of 150dB, the harmonic composition of the sound field was modified to experimentally determine whether this was the case.

Modification of the acoustic signal

A program was written using CSound to generate a multi-harmonic frequency signal, with the amplitude and phase of each harmonic separately defined. A .wav file was generated with two frequency components at 2067Hz and 4134Hz, corresponding to the fundamental and second harmonic of the standing wave; the 2067Hz component had a fixed amplitude and 0^o phase lag, whilst both the

amplitude and phase of the 4134Hz component were varied. The resulting .wav file was transmitted to the loudspeaker via the PC's sound card and an amplifier to produce a multi-harmonic standing wave in the tube. This input sound field is latterly described as the modified sound field, and the unmodified field referred to as the original sound field. As before, the long probe microphone was positioned inside the tube at the first velocity node and the output voltage signal viewed on an oscilloscope. The amplitude and phase of the 4134Hz component of the signal were modified until the pressure signal at the velocity node was sinusoidal, indicating that the second harmonic was at a minimum level. The output voltage from the microphone amplifier was then sampled by the Wavebook and saved as a .wav file. The microphone probe was removed from the tube and, once the streaming had stabilised, PIV measurements were obtained using the method employed in section 5.6.1.

Results and discussion

For a standing wave of sound intensity level 150dB measured at the rigid end of the tube, a second harmonic component with 20% of the amplitude of the fundamental and phase lag of 170^o to 190^o (depending on the amount of seeding in the tube) was required to minimise the amplitude of the second harmonic at the velocity node. When this signal was applied, the amplitude of the second harmonic at the velocity node reduced from 32% to 8% of that of the fundamental harmonic, and the streamline observed at the velocity node (see figure 5.12) became much flatter, indicating a reduction in distortion. At 154dB, the second harmonic component had to be increased from 20% to 35% of the amplitude of the fundamental to reduce the amplitude of the second harmonic at the velocity node to the same level.

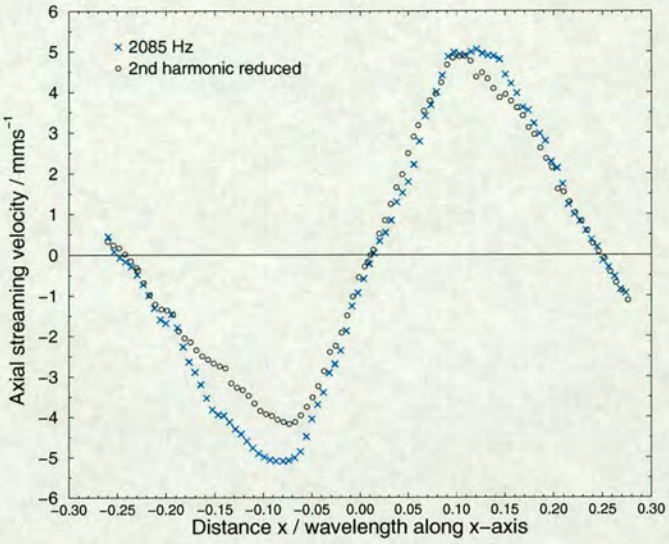

Figure 5.14: Axial velocity profile between two velocity antinodes for a sound field of 150dB measured at the rigid end. Measurements are shown for the original sound field (crosses) and modified field (circles).

Figure 5.14 shows the axial streaming velocity profile produced by the original sound field and the modified field. With the amplitude of the second harmonic diminished, a number of comparisons were made with previous results:

1. The displacement between the adjacent velocity nodes and antinodes is more equally spaced, although it is still larger when the axial streaming motion is directed towards the loudspeaker.

2. The streaming velocity profile still deviates from sinusoidal dependence in a direction opposing theory as seen previously, with the distortion becoming more pronounced with increasing acoustic intensity.

3. The amplitude of the on-axis streaming velocity is substantially reduced in the direction heading towards the loudspeaker.

As the displacement of the nodes and antinodes became more equally spaced, measurements were taken to ascertain whether this was due to a change in the

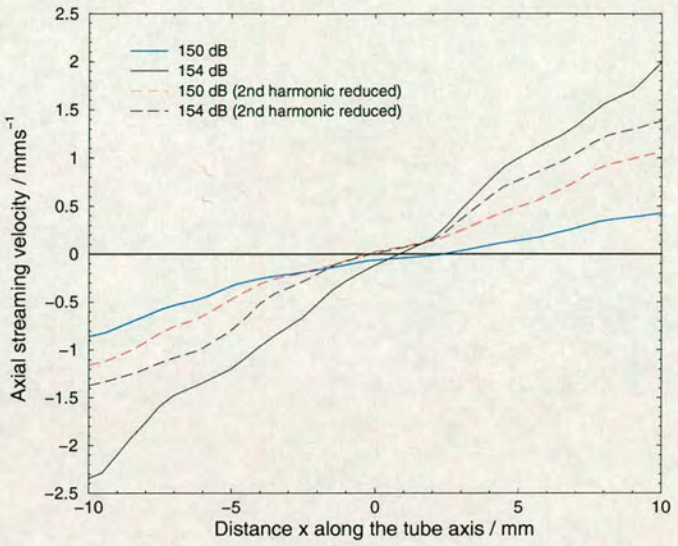

Figure 5.15: Axial velocity profile surrounding an acoustic velocity node for acoustic levels of 150dB and 154dB measured at the rigid end of the tube. Measurements for both acoustic levels generated using the original sound field (solid lines) and modified sound field to reduce the second harmonic distortion (dashed lines) are shown.

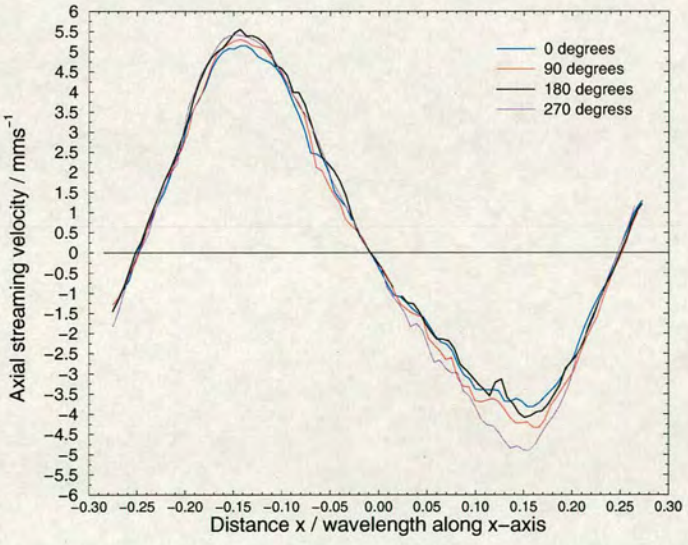

Figure 5.16: Axial velocity profile between two velocity nodes for a sound field of 150dB, with a second harmonic component (of amplitude 20% of the fundamental) added at phase angles 0, 90, 180 and 270 degrees relative to the phase of the fundamental harmonic.

Phase of 2nd harmonic component (degrees)	**Amplitude of u_s ($mm\,s^{-1}$)**	
	+x direction	-x direction
0	5.17	3.89
90	5.30	4.42
180	5.58	4.11
270	5.42	4.95

Table 5.2: Peak amplitudes of the axial streaming velocities shown in figure 5.16.

position of the velocity node, or velocity antinode, or both. Although both the node and antinode move when the acoustic level is changed, reducing the amplitude of the second harmonic primarily results in the shift of the acoustic velocity node. As demonstrated in figure 5.15, when the original sound field is present, increasing the acoustic level by 4dB results in a shift of the velocity node by $\approx$ 1.5mm. With the second harmonic minimised, an increase in 4dB has little or no effect on the relative position of the node. It is also noted that use of the modified sound field results in a velocity node to the left ($\approx$2.6mm at 150dB) of that generated from the mono-frequency sound field, thus confirming the increased symmetry discussed earlier.

Figure 5.16 demonstrates how the axial streaming velocity profile changes when the phase angle of the second harmonic component takes values of 0^o, 90^o, 180^o and 270^o with the amplitude kept constant. The direction of the distortion from sinusoidal remains the same in all four cases. However, a significant change is observed in the maximum and minimum amplitudes of the axial streaming velocity for each case, particularly in the direction of the loudspeaker (right-hand side of the graph); the values of the respective amplitudes are also given in table 5.2. These results demonstrate that alteration of the second harmonic

does not help in obtaining equal peak velocities. It appears from the results obtained that minimising the second harmonic component at the velocity node has a limited effect on the distortion of the axial streaming velocity. However it would be interesting to compare these results with theoretical simulations of modified sound fields.

5.6.3 Effect of different particles on acoustic streaming

Observations of the streaming indicated that the seeding particles influenced the streaming motion and, in particular, the degree of symmetry along the axis of the tube. As discussed in section 4.4, incense smoke is a suitable choice of seeding for acoustic fields in the frequency and sound intensity ranges pertaining to this study. In order to obtain an accurate representation of the fluid flow, the particle concentration must be sufficiently high and homogeneous to obtain adequate PIV resolution. However, results indicate that an excessively high particle concentration alters the properties of the flow, as discussed in section 3.4.2.

Figure 5.17 demonstrates the effect of low and high seeding concentrations on the axial streaming velocity profile in an acoustic sound field of intensity 150dB. With the normal amount of seeding used to obtain valid PIV images (the lower concentration), the axial streaming velocity between a velocity antinode and adjacent node is relatively symmetrical with only a slight distortion, as discussed earlier. When a much higher concentration of particles is present, the distortion becomes more severe with the point of maximum velocity lying approximately three-quarters of the distance from the velocity antinode to node. The amplitude of the streaming velocity is also reduced by $1.3\text{mm}\,\text{s}^{-1}$, corresponding to a

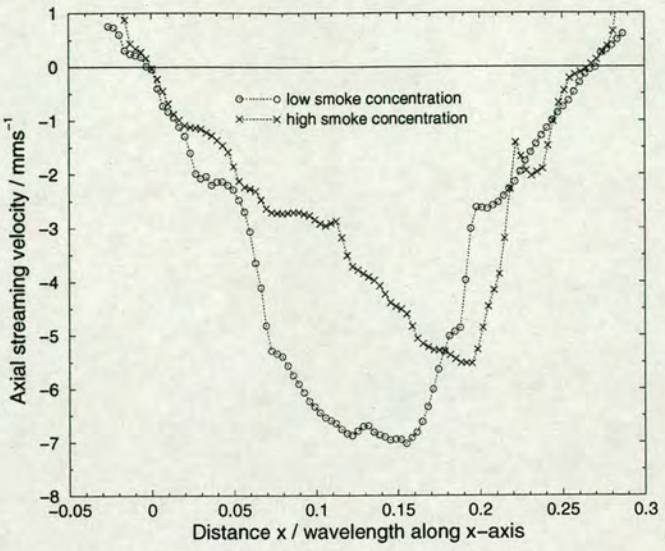

Figure 5.17: Axial velocity profile from velocity antinode to node (left to right) for a sound field of SPL 150dB seeded by a small amount of smoke (circles) and large amount of smoke (crosses).

decrease in intensity of 1dB. This result concurs with observations of increased turbulence at higher particle concentrations.

As the loudspeaker end of the tube was closed, achieving a homogeneous seeding distribution in the vertically mounted tube was very difficult as there was no air current inside the tube to draw the seeding particles in and circulate them around. Therefore, once the tube was sealed by the metal plug, a low intensity sound field was generated inside the tube to aid this process. Proceeding to higher sound field intensities before the particles reached equilibrium resulted in a very unsymmetrical streaming pattern. It was therefore necessary to reach a compromise between leaving the seeding long enough to evenly distribute but having sufficient time to take measurements before the particles coagulated and hence lagged the fluid response as discussed in section 4.4.

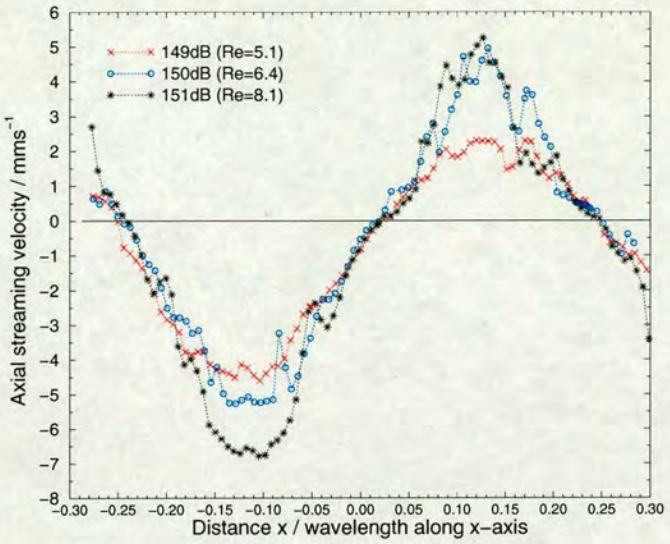

Figure 5.18: Axial velocity profile between two velocity antinodes for a standing wave of frequency 2205Hz for three different acoustic levels. The tube was seeded with bubbles generated by a haze generator.

In order to check the reliability of the measurements using smoke particles, the PIV measurements were repeated with neutrally buoyant bubbles (described in section 4.4) and the results compared. The bubbles were produced by a generator which evaporated and condensed a water-based liquid and then expelled it in large concentrations (as a smoke haze) using an air jet. The haze of bubbles were then channelled into a length of flexible hose and directed into the top of the tube using a funnel. The additional force of the air jet aided the quick and even seeding of the tube. PIV measurements were then taken as described in section 5.6.1.

Figure 5.18 shows the axial streaming velocity profiles between two velocity antinodes for three different acoustic intensity levels from 149 to 151dB, corresponding to Reynolds numbers of Re_{nl}=5.1 to Re_{nl}=8.1. Comparison with the results in figure 5.11 for the same tube seeded with incense smoke shows a high number of similarities, with no significant changes to either the amplitude or displacement discussed above. Calculations using equations 5.14 and 2.11 show that

for Re_{nl}=5.1, there is a discrepancy of u_s=0.3mm s^{-1} (equivalent to 0.4dB) between the amplitude of the axial streaming velocity in the negative axial direction and the expected value calculated from the pressure measured at the end of the tube. For Re_{nl}=6.4 and Re_{nl}=8.1, the measured amplitudes are 0.2 mm s^{-1} and 0.3mm s^{-1} higher, corresponding in both cases to a discrepancy in the pressure amplitude of 0.2dB. This shows that the use of bubbles as seeding particles yields an accuracy commensurate with that achieved using incense smoke.

It appears that the deviation from sinusoidal dependence is smaller than observed when the tube is seeded with incense smoke. However, results were only obtained for acoustic levels up to 151dB. Above this pressure level, the majority of the bubbles burst and the seeding concentration became too low to obtain valid PIV measurements. Hence, it was not possible to ascertain whether the distortion became as pronounced as observed for seeding using incense smoke as the sound intensity increased.

Although it appears that the non-linear harmonic distortion of the acoustic signal, as well as the high concentration and unhomogeneous distribution of the seeding may add to the non-linear effects observed, it is thought unlikely that they are responsible for the asymmetry of the streaming motion.

5.7 Acoustic sound field

The acoustic streaming velocity measurements presented in previous sections show that the apparent positions of the acoustic velocity nodes and antinodes deduced from the streaming motion are not equally spaced. It therefore seemed

logical to check the pressure and velocity components of the acoustic sound field. This was done using two separate methods: the pressure field along the tube axis was measured using the probe microphone to determine the actual spacing of the pressure nodes and antinodes, and the acoustic velocity field was examined using PIV.

5.7.1 Pressure field measurements

A 2085Hz standing wave was set up in the tube using the experimental configuration described in section 5.6.1 but without any seeding present. The sound field, measured at the rigid end of the tube by the long probe microphone, was set at a pressure level of 152.5dB (Re_{nl}=10.8), a sufficiently high level for non-linear distortion to be observed as indicated by previous results. Pressure measurements were then taken along the tube axis at 2mm intervals. In order to confirm that the asymmetry was not due to non-harmonic distortion, measurements were then taken using the modified sound field described in section 5.6.2. To determine the effect of seeding on the measurements, the experiment was repeated after seeding the tube with the normal level of incense smoke required for PIV measurements. The resulting pressure amplitudes are plotted in figure 5.19.

In general, there is good agreement between all three sets of pressure measurements, with the results showing equal spacing between consecutive pressure nodes and antinodes to within ±1mm. However, there is a large discrepancy between the amplitudes of the measured pressure points at the pressure nodes; for the original sound field, the difference between the pressure amplitudes at the pressure antinode and node is 21.5dB. For the modified sound field, this in-

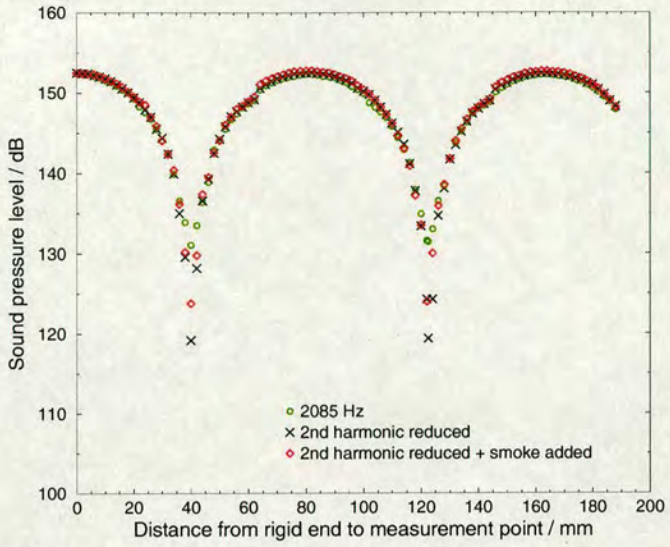

Figure 5.19: Pressure amplitude variation with distance along the closed-end tube for the original and modified sound fields in an unseeded tube, and for the modified sound field in a tube seeded with incense smoke.

creases to 28.5dB with incense smoke present and 33.5dB without smoke. The reduction in pressure amplitude at the pressure nodes for the modified field was not unexpected, since a substantial contribution to this comes from the second harmonic. However, it is surprising that the addition of incense smoke to the tube should modify the pressure amplitude by 5dB. This effect could be due to additional damping in the tube. Although the results indicate that the pressure nodes and antinodes, and therefore the velocity antinodes and nodes (see section 2.2.1) are equally spaced, it is feasible that this may not actually be the case. As discussed in section 4.6, the presence of the probe in the sound field clearly disturbs the acoustic flow and hence the pressure immediately surrounding the probe tip. Since this effect has been observed to be considerable in high intensity fields, it is conceivable that any distortion of the sound field due to other effects may be masked, particularly if the distortion is small compared to the stationary eddies. Hence, these results cannot be considered conclusive evidence that the

distance between consecutive pressure nodes and antinodes within the acoustic sound field is equal to within ±1mm.

Considering this point, the acoustic sound field was examined using the non-intrusive technique of PIV to check for inconsistencies.

5.7.2 Velocity measurements

Velocity measurements of the acoustic sound field in the axial and radial directions were made using the same experimental arrangement as before, but with the PIV set-up as described in section 4.3.1 and illustrated in figure 4.3. Due to the fixed position of the beam alignment optics, the loudspeaker-tube combination was placed onto a translation stage and moved vertically between images rather than vertically translating the camera. The short probe microphone was positioned at the end of the tube to monitor the pressure amplitude. As the separation time between image pairs was restricted to multiples of 0.1 seconds, the frequency of the standing wave in the tube was set to 2071 Hz, allowing ten different positions in the acoustic cycle (although not within the same cycle) to be measured. PIV images were then taken at various points along the tube and for the same range of acoustic intensities as used when observing the acoustic streaming velocities (145 to 154dB).

Figure 5.20 shows the axial acoustic particle velocity profile across the width of the tube at three separate axial positions. As can be seen, the sound wave appears to be propagating in a planar manner across three-quarters of the tube diameter as expected. The lower velocities adjacent to the tube walls are a result of flare in the PIV images, as described in section 5.5.2 and confirmed by comparison

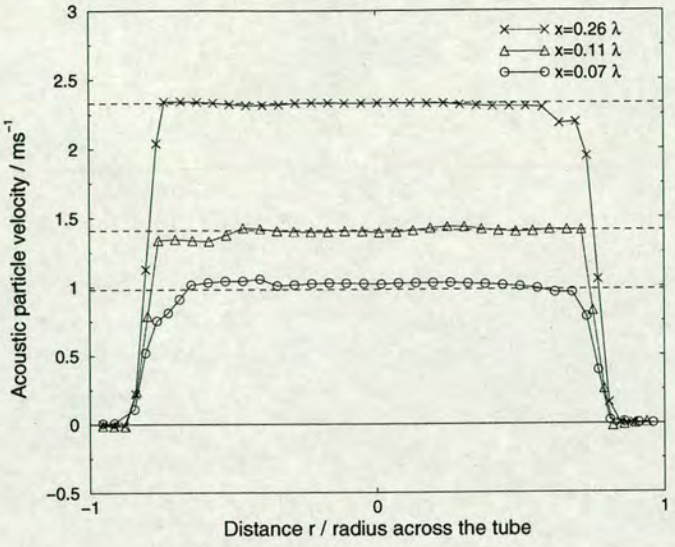

Figure 5.20: Axial velocity profile across the width of the tube for a sound field of intensity 150.7dB. Measurements were taken at three separate positions of distance x from the acoustic velocity node. Experimental results (symbols) are compared with theoretical values (dashed lines).

with the PIV images. The cross-sectional velocity measurements agree well with theoretical values, calculated using equations 2.11 and 2.12, at positions x=0.26λ and x=0.11λ. However, a discrepancy of about 5% is observed at the position nearest the velocity node.

The axial velocity profile of the acoustic field at various points within the acoustic cycle and taken over a number of cycles is shown in figure 5.21 for two slightly different positions in the tube. The two sets of results were obtained maintaining near-identical acoustic conditions but in separate experiments. Although the positions within the tubes of figures 5.21(a) and (b) are not quite the same (the velocity node at the left of figure 5.21(a) corresponds to the velocity node at the centre of figure 5.21(b)), comparison between the two figures yields an interesting observation. In figure 5.21(a), the velocity node appears to be in the same position at various points in the acoustic cycle as well as over a number of

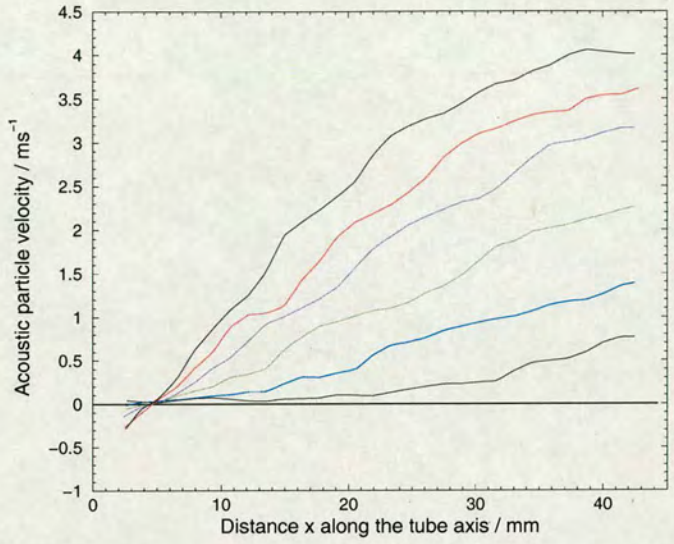

(a)

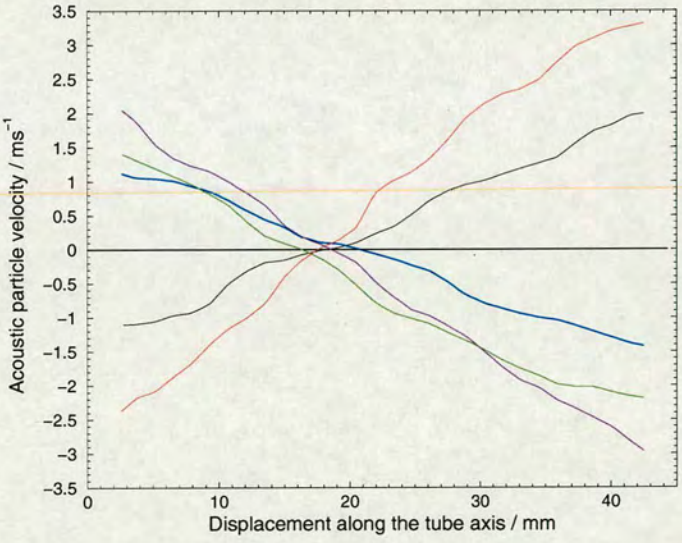

(b)

Figure 5.21: Axial velocity profile of the acoustic field, taken at times corresponding to various points in the acoustic cycle and over a few acoustic cycles. Measurements were taken in a sound field of frequency 2064Hz and intensity level of 152dB at two positions in the tube; (a) between an acoustic velocity node and antinode and (b) with a velocity node in the centre of the image.

cycles, as expected. However, this is clearly not the case in figure 5.21(b), where the position of the velocity node is observed to vary by up to 4.4mm. This variation also appears to be independent of position (and hence velocity amplitude) in the acoustic cycle. Both sets of results were observed in repeated measurements, with no obvious indication of the source of the effect.

Direct observations of the acoustic field, whilst illuminated by the pulsed light sheet at very low intensity, showed that the positions of the velocity nodes and antinodes oscillated intermittently with a frequency between 0.5 and 2Hz. These observations were found to be independent of the sound field frequency. Due to the continuous wave illumination used in previous experiments (as opposed to the stroboscopic nature of the pulsed light sheet), this effect had not previously been noted.

These observations suggest that the acoustic wavelength is varying with time. Given the high precision of the frequency signal provided by the Stanford sine-wave generator, this implies that the speed of sound within the tube is not constant. It is possible that this could be due to either a density variation, or temperature gradient along the length of the tube, arising from the nature of the seeding process. Although the seeding was left to equilibrate throughout the tube prior to taking measurements, any remaining variation in density or temperature could conceivably yield this effect. The intermittent behaviour of these low frequency fluctuations make them high unlikely to be the source of the asymmetric streaming pattern, which was consistently observed along the length of the tube.

5.8 Conclusions

Literature research showed that whilst much experimental and theoretical work on acoustic streaming exists, little experimental work has been undertaken on the effects of fluid inertia on the streaming motion. This parameter becomes significant when high-intensity acoustic sources are used to generate the streaming motion. Recent theoretical work on the acoustic streaming in a cylindrical waveguide by Menguy [68] predicted that in the presence of high-intensity sound fields, distortion of the streaming motion will occur due to the fluid inertia.

Preliminary observations of the streaming motion showed that it was very susceptible to distortion by mean current circulations inside the tube caused by insufficient sealing measures at the tube ends, and convective currents both inside and outside the tube. Improvements were made to the experimental apparatus, which yielded a more symmetrical motion.

PIV measurements of the acoustic streaming motion in the tube, in conjunction with pressure measurements at the tube termination, revealed that the shape of the toroidal vortices became increasingly distorted with increasing sound intensity. At very high sound intensities, the vortices were observed to be wider at the velocity node and taper down to a point at the velocity antinode; this observation opposed the theoretical predictions, where the vortices were expected to be distorted in a similar manner but with the tapered end of each vortex at the velocity node. In addition, the component of the streaming velocity along the tube axis was found to deviate with increasing sound field intensity from the sinusoidal dependence expected when inertial effects were considered negligible. However, the direction of the deviation was also found to oppose theoretical

predictions; the positions of the velocity maxima and minima deviated towards the velocity nodes rather than the antinodes. The positions of the zero velocity points along the axis were unequally spaced, with a larger displacement between adjacent velocity nodes and antinodes when the on-axis streaming motion was directed towards the loudspeaker. Due to the significant difference in displacements (when compared to the predicted deviation from sinusoidal dependence), direct comparison with theory was extremely difficult. Hence, further experimental studies were undertaken using PIV in order to identify the source of the longitudinal asymmetry.

Following observations of non-linear behaviour at the velocity nodes in the streaming pattern, pressure measurements of the sound field identified a relatively high second harmonic component at the velocity node; however, comparison with theoretical calculations suggested the amplitude of the second harmonic was not large enough to mask the nonlinear streaming effect. While modification of the acoustic field to minimise the second harmonic component reduced the distortion of the streaming pattern at the velocity node, this was not found to be responsible for the asymmetry of the streaming motion. Extremely high seeding concentration levels were shown to severely distort the axial streaming velocity profile, as well as causing a significant decrease in the streaming velocity amplitude. The streaming pattern was also observed to be very unsymmetrical if the streaming motion was instigated before a homogeneous seeding distribution was achieved. Streaming velocity measurements obtained using neutrally buoyant bubbles showed good agreement with those obtained using incense smoke particles. However, measurements using the bubbles were limited to intensity levels up to 151dB, above which the bubbles burst. Although the seeding was observed

to affect the streaming motion to a certain extent, the results showed it was not ultimately responsible for the asymmetry of the streaming motion.

PIV measurements of the acoustic sound field showed an intermittent oscillating behaviour of the velocity node and antinode positions, with a spatial deviation of up to 4.4mm; this was confirmed by direct observation using the stroboscopic illumination of the pulsed light sheet. Although the source of this fluctuation was not ascertained, it was considered highly unlikely that this behaviour was responsible for the asymmetry of the longitudinal streaming pattern.

Chapter 6

Acoustic behaviour of an open-ended pipe

The behaviour of acoustic fields in the vicinity of a tube termination has been the subject of much experimental and theoretical investigation. This has important implications in the study of wind instruments, where sound levels both inside and outside the instrument can be as high as 160dB under playing conditions. The interaction of the flow with the walls at an opening in the tube strongly affects the behaviour of the acoustic field and hence the sound produced by the instrument.

This chapter describes the use of PIV to investigate the non-linear acoustical behaviour at the termination of an open-ended tube. Following a review of the existing theoretical and experimental work, initial observations of the flow behaviour at the open end of a tube are presented. A method for obtaining the radiation impedance at the end of a tube using PIV measurements in conjunction with pressure measurements is then outlined, and preliminary measurements taken in a simple acoustic tube configuration to validate the technique. Measurements of the real part of the radiation impedance at the open exit of a tube as

a function of intensity are presented, and the results compared to existing measurements using alternative techniques. Finally, the vorticity at the tube exit at various points within the acoustic cycle is examined.

6.1 Background

6.1.1 Linear radiation impedance

As described in section 2.2.2, when a sound wave reaches the open end of a tube, the change in acoustical conditions results in a change in acoustic impedance and hence part of the wave leaves the tube as radiated sound with the remaining part reflected back along the tube. The acoustic impedance at the end of the tube (referred to as the radiation impedance Z_r) is therefore a complex quantity which can be separated into real and imaginary parts:

$$Z_r = R + jX, \tag{6.1}$$

where the acoustic resistance, R, is the real component of the acoustic impedance and represents the dissipation of energy. The acoustic reactance, X, is the imaginary component which characterises the inertia of the acoustic flow around the end of the tube. The end effects associated with the acoustic reactance can be compensated for by adding an end correction to the geometrical tube length. From this corrected length, the resonance frequency of the tube can then be calculated.

The values of both the acoustic resistance and reactance depend strongly on the geometry of the pipe end. In the linear regime (i.e. for a weak acoustic field at the exit of the tube) and for low frequencies such that $ka \ll 1$, the radiation impedance for an unflanged thin-walled tube was given by Levine and Schwinger [62] as:

$$Z_{rlin} = \left(\frac{(ka)^2}{4} + jk\delta_0 \right) Z_c \tag{6.2}$$

with characteristic impedance $Z_c \simeq \rho c/S$, wavenumber k, tube radius a and length correction δ_0=0.6133a.

The radiation impedance for an identical tube but with the addition of an infinite flange at the end was found by Nomura et al. [75] to be:

$$Z_{rlin} = \left(\frac{(ka)^2}{2} + jk\delta_\infty \right) Z_c \tag{6.3}$$

where the corresponding length correction δ_∞=0.8216a.

However, at higher acoustic levels (where the acoustic velocity at the tube exit $u \geq 0.01c$), non-linear effects are observed in the tube. These include shock waves [50], which result when the acoustic wave becomes progressively deformed as it propagates along the tube, and vortex formation, a localised effect at the open end of the tube [28, 52]. At such acoustic levels, the above linear equations are no longer valid.

6.1.2 Non-linear radiation impedance

One of the first observations of non-linear behaviour was by Sivian in 1935 [92]. He showed that the acoustic resistance of an orifice in a plate placed at the end of a tube depends on the intensity of the incident sound wave. This situation is akin to a tube terminated with a finite flange. Using smoke particles to visualise the flow, Ingard and Labate [52] observed the formation of vortices and jets at the orifice as the sound intensity levels were increased. They identified four definite flow regimes for a range of orifice diameters and frequencies under increasing particle velocity. A more detailed experimental investigation was made by Ingard and Ising [51] in 1967. By simultaneously measuring the flow velocity through an orifice in a plate and the sound pressure fluctuations producing the flow, they showed that at high sound intensity levels, the acoustic resistance (the real part of the radiation impedance) increased proportionally with the orifice flow velocity whereas the acoustic reactance decreased but at a much slower rate. Later observations by Disselhorst and van Wijngaarden, and also by Peters et al. [28, 79], showed that the coefficient of proportionality of the resistive term can be affected by the edge sharpness of a tube termination. Ingard and Ising [51] also found that the axial flow velocity outside the tube during outflow and inflow was asymmetric, with the outflow velocity remaining large at substantial distances from the orifice, but the inflow velocity rapidly decreasing to small values at a distance of only two to three diameters from the orifice; this confirmed the occurrence of flow separation and jet formation at the orifice.

Following these early observations, several authors performed further theoretical and experimental work to investigate these non-linear effects, most notably vortex shedding and jet formation. This work is discussed below.

One of the main parameters characterizing the flow is the acoustic Strouhal number Sr_{ac}, which for an acoustic velocity through the exit of the pipe of amplitude u_{ac} is defined as [79]

$$Sr_{ac} = \frac{\omega a}{u_{ac}}, \tag{6.4}$$

where ω is the angular frequency of the sound wave inside the pipe, and a is the pipe radius. The Strouhal number represents a measure of the non-linearity of the flow, where a small Strouhal number is indicative of significant non-linearity. Conversely, the opposite is true; a large Strouhal number characterises a largely linear flow.

It is generally accepted that at sufficiently high acoustic levels, flow separation occurs at the inner edges of a tube due to frictional forces. This causes the formation of vortices, which are subsequently shed from the boundary layer into the main flow, and the formation of jets. The vortex shedding results in acoustical energy losses as some of the acoustic energy is converted to kinetic energy of the vortical motion. This kinetic energy is then dissipated as heat from frictional interactions.

The strength of this non-linear behaviour, and hence the amplitude of the acoustical energy losses, depends on the geometry of the tube exit. For a tube with sharp inner edges, flow separation occurs both during outflow and inflow. As a result, vortex shedding occurs throughout the acoustic cycle, with the flow concentrated into a jet when the flow is directed out of the tube exit, as illustrated in figure 6.1. The motion of the acoustic flow along the tube axis becomes more asymmetric as the acoustic exit velocity increases, with the amplitude of the flow velocity out exceeding that of the flow in due to the additional contribution from

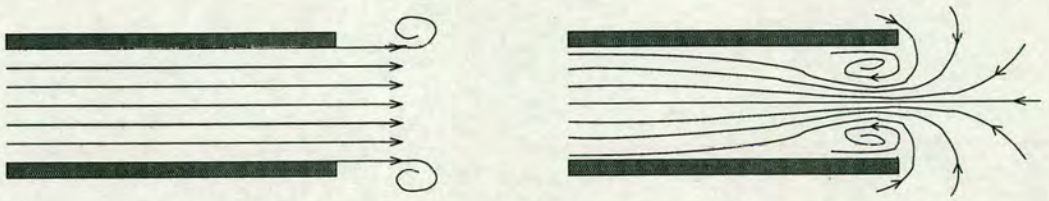

Figure 6.1: Acoustic flow at the exit of a tube with sharp inner edges. During the first half the acoustic cycle, the flow is directed out of the tube in the form of a jet, and vortex shedding occurs (a). During the second half of the cycle, the flow reverses direction, travelling into the tube (b).

the vortices and jet. As can be expected, the resulting acoustical energy losses are significant, even for relatively low acoustic velocities at the tube exit.

For a tube with rounded inner edges, the vortex shedding and related acoustic energy dissipation are much less significant. At high acoustic Strouhal numbers (low acoustic velocities), the acoustic flow can be considered as an ideal potential flow during both the inflow and outflow part of the acoustic cycle. However, at higher acoustic velocities at the tube exit (i.e. for acoustic Strouhal numbers of the order of unity or smaller), flow separation occurs during the outflow part of the acoustic cycle and jet-like flow is seen [28].

Using an experimental flow visualisation technique, Disselhorst and Wijngaarden [28] showed that in the case of a sharp edged tube, vortices were generated during inflow and expelled during outflow; two approaches were proposed to model this for different Strouhal numbers.

For the case of high Strouhal numbers, ($\mathrm{Sr}_{ac} \gg 1$), Disselhorst and van Wijngaarden [28] proposed a two-dimensional flow model employing discrete point vortices. This approach was justified because vortices shed at the end of tube were not convected away, but remained close to the position where they were

generated. The model was used to predict the acoustic energy absorption due to vortex shedding induced at the end of a two-dimensional channel by a sinusoidal acoustic signal with no mean flow present. Reasonable agreement was found with the results of the flow visualisation work.

For low Strouhal numbers, Disselhorst and Wijngaarden used a quasi-stationary approach, in which the flow is directed out of the tube (with assumed jet formation) during the first half of the cycle. During the second half of the cycle, the flow is directed back into the tube. This is characterized by the formation of a *vena contracta* (narrowed part of the flow stream a small distance inside the end of the tube) and regions of turbulence adjacent to the walls just inside the tube. Good agreement was again found between the theoretical results and experimental work. Similar results were found by Peters and Hirschberg [78] using a model with a single point vortex and vortex segment attached to the edge.

A similar quasi-stationary approach has been used to model the non-linear behaviour at high acoustic amplitudes with and without a mean flow present for the case of pipes terminated by an orifice plate at the exit [51] and by a nozzle [11, 24].

For further reference, a good review of theoretical and experimental investigations at open tube terminations is given by Peters et al. [79].

6.1.3 Recent work

Recently, two experimental studies of the radiation impedance at the open end of a tube have been published [9, 25]. Dalmont et al. [25] used the two-

microphone method (summarised in section 3.2.2 and [21]) to determine the radiation impedance at the open end of a thin walled unflanged copper tube with increasing sound intensity level. As discussed earlier, this method is difficult to calibrate, and relies on indirect calculation of the velocity through pressure measurements.

Using equation 6.2 to calculate the linear component of the acoustic resistance, the non-linear component was found to be approximately proportional to the amplitude of the average acoustic velocity through the cross-sectional area of the tube exit, u_{exit} :

$$Re(Z_{rnl}) = (0.6 \pm 0.1)\frac{u_{exit}}{c} Z_c \tag{6.5}$$

where c is the speed of sound and Z_c is the characteristic impedance of the medium inside the tube. This confirmed the observations of Ingard and Ising [51].

Experimental studies by Atig [9] used the same two-microphone method to determine the radiation impedance for a tube terminated by two different geometries: round edges and sharp edges. Using a similar approach to that used by Dalmont et al. [25], Atig also determined the acoustic resistance. This was done for both geometries over a range of acoustic velocity amplitudes at the exit of the tube from 1 to $23\mathrm{m\,s^{-1}}$. For the case of the round-ended tube, it was found that for exit velocities below $7\mathrm{m\,s^{-1}}$, the non-linear radiation impedance remained relatively constant with increasing velocity. For exit velocities above this value, the non-linear impedance was observed to increase exponentially with increasing velocity up to $17\mathrm{m\,s^{-1}}$. Above $17\mathrm{m\,s^{-1}}$ a linear dependence with exit velocity was observed. For the case of the sharp-ended tube, the non-linear impedance increased proportionally to the exit velocity over the entire range of velocities.

The objective of the experimental work described below was thus to investigate the non-linear behaviour of acoustic fields at the open end of a tube for a range of acoustic exit velocities. In particular, the primary aim of this work was to measure the radiation impedance and hence evaluate the dependence of the acoustic resistance on the exit velocity. The following sections discuss the application of PIV to the measurement of the acoustic fields at the tube exit. In contrast to the recent work described above, PIV was selected for this work as it provides a direct velocity measurement and is a non-intrusive method of investigation.

6.2 Flow visualisation at the exit of an open-ended tube

Preliminary observations of the flow behaviour at the open end of a tube with rounded inner edges were made using the PIV technique. The apparatus used for the acoustic field measurements is illustrated in figure 6.2. This experimental arrangement is very similar to that used in chapter 5 for the acoustic streaming measurements, with the exception of the perspex box surrounding the tube. Initial tests showed that in order to obtain PIV data, it was necessary to retain the seeding particles within the region of the open tube end for the duration of the measurements. Accordingly, a different perspex box of height 500mm and square cross-section of length 120mm, with a flange on one end, was constructed. The box flange was attached to a plate on the top of the loudspeaker-tube connector such that its walls were equidistant from the vertically-mounted cylindrical tube and its total height was greater than that of the enclosed tube. The distance

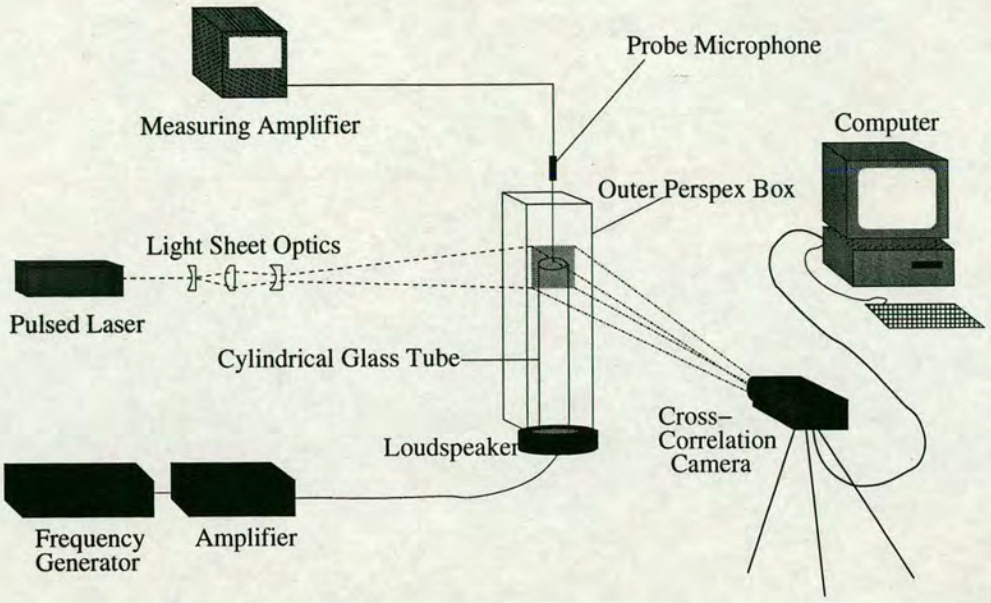

Figure 6.2: Experimental arrangement for taking PIV measurements of the acoustic field at the open end of a tube.

from the box walls to the tube exit was made as large as practicable to minimise boundary effects on the behaviour of the acoustic field.

Preliminary observations were made using the cylindrical glass tube used for the acoustic streaming measurements in chapter 5, of internal radius 13.25mm, wall thickness 2mm and length 532mm, which was mounted vertically onto the loudspeaker. A burning incense stick was held just inside the top of the perspex box for a few seconds to produce smoke particles in the volume surrounding the tube. An acoustic field was then generated inside the tube by the JBL compression driver, controlled by an amplified sinusoidal generator signal. In order to produce a strong velocity field at the tube end, frequencies around the acoustic resonances of the loudspeaker-tube combination were used. The resonant frequencies were identified by positioning the long probe microphone a small distance inside the top of the tube and manually sweeping through the frequencies to find the values corresponding to pressure maxima.

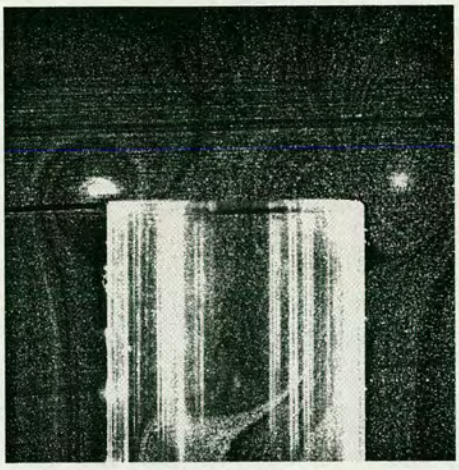

Figure 6.3: PIV image of the acoustic flow behaviour at the open end of a tube with rounded inner edges, excited at a resonance frequency of 564Hz and sound field intensity of 123.5dB.

The PIV apparatus was set up as described in section 4.3.1 and shown in figure 4.3, with the pulsed light sheet projected through the axis of the tube. Since the position of the light sheet was fixed, the combined loudspeaker-tube apparatus was placed on a vertical translation stage and positioned such that the pulsed light sheet was projected through the axis of the tube. The centre of the tube was positioned at the beam focus with the tube exit in the region of illumination. Pairs of images 40μs apart were recorded using the Kodak ES 1.0 camera. Viewing the flow in real-time with the PIV system, the long probe microphone was positioned along the tube axis with the tip of the probe a distance of 8mm (164 pixels) outside the tube, and the pressure amplitude of the acoustic field measured. This point corresponded to the position of the pressure minimum for a thin-walled unflanged tube [62].

Figure 6.3 shows a PIV image of the acoustic flow at the open end of the tube for a sound pressure level, measured just outside the tube exit, of 123.5dB. The

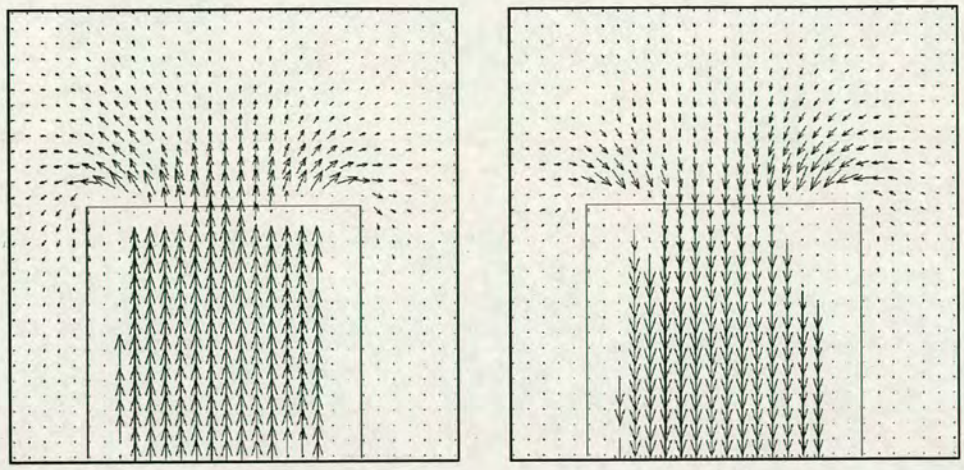

(a) (b)

Figure 6.4: Acoustic particle velocity maps corresponding to the PIV image in figure 6.3, showing the maximum parts of the acoustic phase when the acoustic flow is directed (a) out of the tube exit (ϕ_u=90^o) and (b) back into the tube (ϕ_u=270^o).

acoustic particle velocity, obtained from the PIV image at the same point where the pressure measurement was taken, was found to be 0.7m s^{-1}, corresponding to Sr_{ac}=67. Although a region of stationary circulation is observed outside the tube, no non-linear effects are seen. This is as expected for a flow with such a high Strouhal number. The velocity vector maps corresponding to the PIV image in figure 6.3, with the phases in the acoustic cycle where ϕ_u=90^o (maximum acoustic velocity out of the tube), and ϕ_u=270^o (maximum velocity into the tube), are shown in figure 6.4. The acoustic motion is symmetrical, with equal acoustic particle amplitudes (to within an error of 4%) during both inflow and outflow as expected.

It is also noted from the velocity maps in figure 6.4 that a significant amount of velocity information adjacent to the walls inside the tube is missing due to problems with flare (as observed in chapter 5). Although this information is

not required in order to measure the radiation impedance, it makes quantitative observation of flow separation and vortex formation inside the tube virtually impossible.

6.3 Impedance measurements using PIV

In order to measure the impedance of any acoustic field, it is first necessary to know the magnitudes of the fundamental harmonic components of the acoustic velocity and pressure at one or more specific points, in addition to the phase relationship between them. Impedance is inherently a linear concept, whereby the pressure and acoustic velocity are assumed to vary sinusoidally. However at high intensity levels, both pressure and velocity will become distorted to some degree, which ultimately limits the validity of the concept.

6.3.1 Measurement of the acoustic velocity and pressure amplitudes

In order to obtain a true measurement of the impedance, it is necessary to measure the pressure and acoustic velocity at the same spatial position. However, it was not possible to do this concurrently, as the long probe microphone required for the pressure measurements was found to cause local flow disturbance as shown in section 4.6. Due to the necessity to measure the pressure and acoustic velocity at specific points in the flow, it was not possible to take PIV measurements of the acoustic field simultaneously with pressure measurements within the field. Hence, the velocity measurements were obtained first using PIV, after which the probe

microphone was suspended in the acoustic field and the pressure measured at specific PIV grid points. Using the PIV apparatus to view the area of interest in real time, the tip of the probe microphone was positioned to within an accuracy of ± 2 pixels, corresponding to ± 0.1mm for a viewing area of 5cm^2. As before, the output voltage signal from the Brüel and Kjær measuring amplifier was sampled by the Wavebook A/D converter at each point to yield a pressure amplitude.

There are two inherent problems in obtaining the fundamental component of these pressure and velocity measurements. Firstly, non-linear effects at the tube exit can distort the velocity wave. Secondly, non-linear propagation and loudspeaker distortion make it practically impossible to obtain a purely sinusoidal pressure signal.

Whilst the velocity field became increasingly distorted with high sound intensity, an FFT of the velocity signal allowed accurate determination of the fundamental and higher harmonic component amplitudes. A graph of exit velocity as a function of phase angle within the acoustic cycle provided visual confirmation that the distortion was limited and the velocity signal was therefore close to sinusoidal; this is discussed in section 6.3.4. The pressure signal was similarly analysed using an FFT to extract the separate harmonic components. The relative magnitudes of the higher harmonics were compared to the fundamental to verify that the pressure signal was not seriously distorted either.

6.3.2 Establishment of the phase relationship

Due to the separate measurement of the pressure and acoustic velocities, establishing their phase relationship was more complex. In order to relate the two sig-

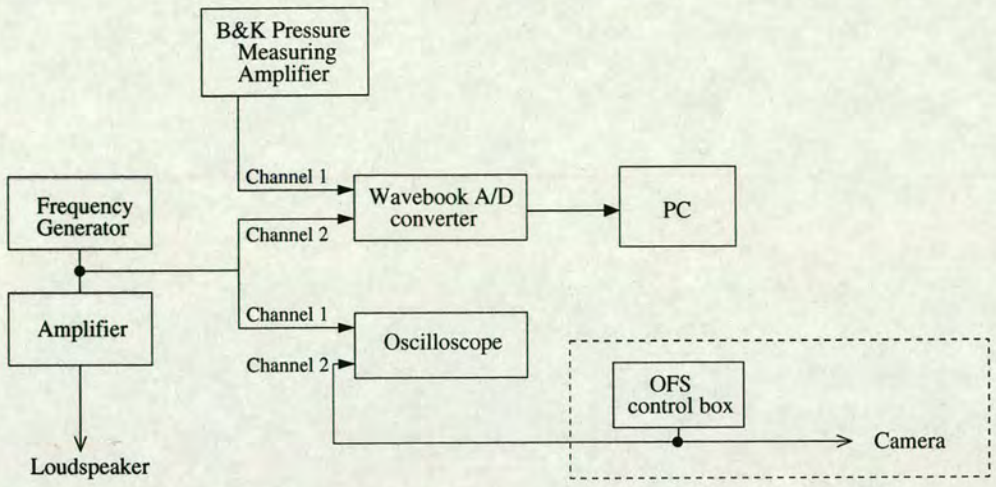

Figure 6.5: Apparatus for measuring the phase difference between the pressure and acoustic velocity. The dotted outline indicates continuation to figure 4.3.

nals, the sinusoidal input signal to the loudspeaker, which was assumed to have a constant frequency throughout the measurements, was used as a reference signal as illustrated in figure 6.5. The phase differences between the acoustic velocity and the reference signal, and separately between the pressure and the reference signal, were obtained. From this, the phase difference between the pressure and velocity was then calculated.

A Stanford pulse generator produced the sinusoidal reference signal of frequency f, which was then amplified and used to drive the loudspeaker. A manual control on the pulse generator allowed the phase angle of this input signal to be shifted relative to the time base of the frequency generator by a phase angle ϕ_{in}. The voltage output from the pulse generator was additionally fed to Channel 1 of a digital oscilloscope, and the pulsed input voltage signal to the correlation camera, whose rising edge controlled the start of the first exposure of each image pair, was fed into Channel 2.

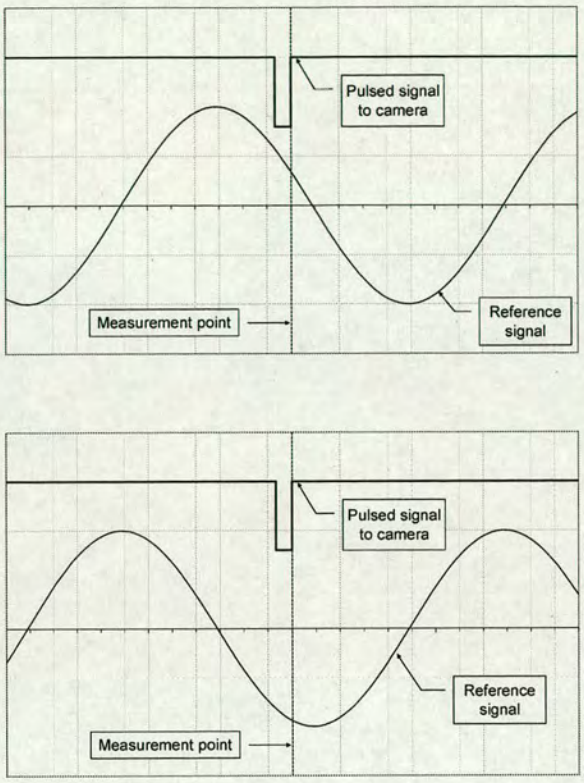

Figure 6.6: Representation of the oscilloscope screen, showing the pulsed signal to the camera and the reference signal for two values of ϕ_{in}, 90 degrees apart.

Due to technical problems, it was not possible to trigger the rising edge of the first pulse to the camera to coincide with a specific point of the reference signal. Instead, the rising edge of the pulse was set as the measurement point on the oscilloscope screen as shown on figure 6.6. Small adjustments (of the order of $\pm 0.02\,\text{Hz}$) were initially made to the frequency of the reference signal (prior to taking measurements) such that the beginning of each pulse to the camera coincided with the same point on the reference signal (as viewed on the oscilloscope) for a fixed input phase ϕ_{in}. This frequency was then kept constant throughout the experiment.

In order to establish the phase relationship between the reference signal and the velocity field, ϕ_{in} was shifted in 10^o increments from 0 to 360^o, with PIV image pairs recorded one second apart and five image pairs taken at each phase angle. Figure 6.6 shows a representation of the oscilloscope screen for two values of ϕ_{in}, 90^o apart. Due to the restricted number of images which could be obtained at any one time (as discussed in section 4.3.1), image pairs corresponding to input phase angles of ϕ_{in}=0^o–180^o, and ϕ_{in}=190^o–360^o, were acquired as two separate data sets, taken in close succession in order to maintain similar acoustic conditions.

The phase angle of the reference signal corresponding to the rising edge of the pulse, ϕ_{ref}, indicated by the measurement point on figure 6.6, was recorded for input phase angles of ϕ_{in}=0^o, 180^o, 190^o and 360^o. This gave four independent measurements from which the phase amplitude of the velocity relative to the reference signal, ϕ_u-ϕ_{ref}, could be calculated, as well as providing a check on consistency between the two datasets.

Since the pulse width between the first and second exposures of $\triangle t$=40μs was significant compared to the period of one acoustic cycle, a phase correction was made to these results. Due to the change in velocity which occurs between the first and second exposures, the actual velocity calculated from the PIV map lies between the velocity at the time of the first image and that at the second image. This is akin to the problem of velocity gradients across an interrogation area discussed in section 3.5.4. Hence, in order to reduce the phase error associated with this effect, a phase correction corresponding to half the pulse width (i.e. 20μs) was added.

Once the experimental measurements were complete, the PIV images were cross-correlated to produce vector maps and each set of five vector maps was averaged using a standard software package. By examining the averaged vector maps and extracting velocity values from specific points on each averaged map (corresponding to positions of pressure measurement), the maximum acoustic velocity amplitude, $|u_a|$, was established, and the mean phase amplitude and associated error calculated.

For the pressure measurements, the output voltage signal from the Brüel and Kjær measuring amplifier was taken to Channel 1 of the Wavebook A/D converter, and simultaneously captured with the reference signal from the pulse generator, which was fed into Channel 2. The phase relationship of the pressure relative to the reference signal, ϕ_p - ϕ_{ref}, was then calculated using the auto.c program written by Cullen [23]. This calculation included corrections for the reverse bias of the probe microphone and the phase response of the long probe calculated in section 4.5. Although the pressure signal was expected to contain higher harmonic components, especially at high intensities, the program only considers the strongest frequency component in the signal. This corresponded to the phase difference between the reference signal and the fundamental harmonic, confirmed by the output of the frequency by the program during analysis.

Due to the complex nature of the method for ascertaining the phase relationship between pressure and velocity using PIV, preliminary measurements were made in an acoustic field where the phase difference between the two parameters was already known. The method was then applied to the more complex situation of the measurement of radiation impedance at the open end of a tube.

6.3.3 Preliminary measurements

From section 2.2.1, when a standing wave is set up in a closed-end tube, the pressure and acoustic velocity are known to be $\pi/2$ out of phase (with respect to time), with the velocity leading the pressure. This situation is ideal for the purpose of checking the accuracy of phase measurements using PIV.

The experimental configuration described in section 6.2 was used, but with the end of the cylindrical glass tube (opposite the loudspeaker) terminated by the aluminium plug with inset o-rings as used in the acoustic streaming experiments (see figure 4.2). In order to optimise the signal-to-noise ratio of the PIV measurements, the vertical position of the tube was set such that a velocity antinode was situated at the centre of the PIV image.

Incense smoke particles were introduced into the end of the tube, and the end then sealed with the plug. Once the seeding concentration appeared to be homogeneous, a standing wave of frequency 806Hz (corresponding to the third resonant mode of the loudspeaker-tube combination) was set up in the tube and the sound field intensity at the rigid end of the tube monitored by the long probe microphone. Increasing the phase of the input signal to the loudspeaker by 10 degrees after each set of 5 double exposures, PIV images were taken for phase angles ϕ_{in}=0^o to 180^o. The long probe microphone was then lowered into the tube through the hole in the metal plug and positioned at the pressure node (velocity antinode). A calibration image was taken to ascertain the position of the probe, and the pressure and input signal to the loudspeaker were then sampled by the A/D converter and analysed. Measurements were taken at three sound intensity levels (measured at the rigid termination of the tube) of 145dB, 150dB and 155dB.

Sound Intensity Level at rigid termination (dB)	ϕ_p - ϕ_u (degrees)		Mean ϕ_p - ϕ_u (degrees)
	ϕ_{in}=0°	ϕ_{in}=180°	
145	-93.7	-89.3	-91.5
150	-89.7	-85.3	-87.5
155	-89.5	-90.1	-89.8

Table 6.1: The phase difference ϕ_p-ϕ_u between the pressure and acoustic velocity for a standing wave in a closed-end tube, for three different sound intensity levels measured at the rigid termination of the tube.

Once the PIV maps had been cross-correlated, the phase relationship between the pressure and velocity was calculated using the method outlined above for ϕ_{in}=0° and ϕ_{in}=180°, with the velocity value extracted at the point on the velocity map corresponding to the position of the probe microphone tip.

The results are shown in table 6.1. As can be seen, the mean phase difference ϕ_p - ϕ_u is close to the theoretical value of -90° for each case, to within an error of 2.5°. These results verified the validity of this approach.

6.3.4 Measurements of radiation impedance for a thin-walled unflanged open pipe

In order to be able to make quantitative comparison between impedance measurements using PIV and existing measurements using the two-microphone method by Dalmont et al. [25] and Atig [9], a similar tube configuration was used.

Experimental method

The cylindrical glass tube used in previous experiments was replaced by a copper tube of internal radius 10.1mm, wall thickness 0.9mm and length 250mm.

This had the obvious restriction of limiting observations to the tube exit and surrounding area. However the use of copper rather than glass allowed the exit geometry to be machined more precisely, approximating a thin-walled unflanged tube. This was used in conjunction with the experimental apparatus described in section 6.2.

In order to obtain an optimal signal-to-noise ratio for the velocity measurements, frequencies around the acoustic resonances of the loudspeaker-tube combination were used. To identify the resonance frequencies, the tip of the long probe microphone was positioned 4cm inside the tube to minimise end effects due to the acoustic field behaviour at the tube exit. Then, using the same method as described in section 5.6 for obtaining the resonance frequencies of the closed tube, the resonance frequencies for the open tube were obtained over a frequency range of 50 to 2000Hz.

The frequency response curve for the open-ended copper tube is shown in figure 6.7. As can be seen, the copper pipe has resonance frequencies at 655Hz, 1265Hz and 1910Hz.

It was decided to take measurements at a frequency of 700Hz, lying close to the first resonance of the loudspeaker-tube system, for two main reasons. Firstly, this frequency was close to the excitation frequency used by Atig [9] for a similar experimental configuration; in addition, lower frequencies minimise the error in the phase measurements due to the set time separation between the first and second exposures of $\triangle$t=40μs (as discussed in section 6.3.2).

Preliminary PIV measurements identified that, due to glare at the tube exit, the first row of interrogation areas above the tube exit did not yield velocity

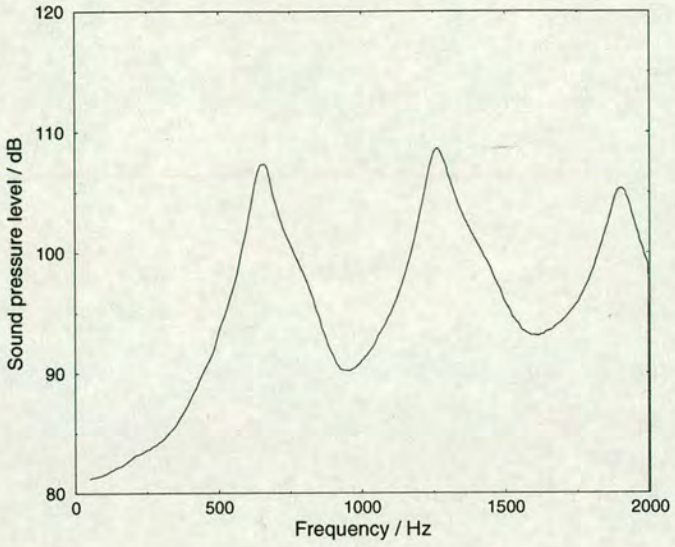

Figure 6.7: Pressure amplitude for the loudspeaker-tube system with an open end.

measurements. Hence measurements were taken at a distance of 1.3mm (29 pixels) outside the tube, corresponding to the grid points representing the central positions of the second row of interrogation areas above the tube exit. Measurements were taken for sound intensity levels from 121dB to 142dB (Sr_{ac}=71.9 to 7.6). Three pressure measurements were taken for each data set at positions corresponding to the three central PIV grid points around the tube axis. This provided a check on the pressure signal for each case, and two surplus pressure measurements in the near vicinity of the tube axis in case of missing or invalid velocity vectors on the PIV maps.

When the velocity amplitudes extracted from the PIV maps at the specific grid points pertaining to the pressure measurements were plotted as a function of phase angle within the acoustic cycle, the resulting sine wave was found to have a superimposed steady flow velocity V_{st}. This was directed out of the tube such that the velocity signal was as illustrated in figure 6.8, with the value of V_{st} increasing with sound intensity. As discussed in section 6.1.2, in the non-

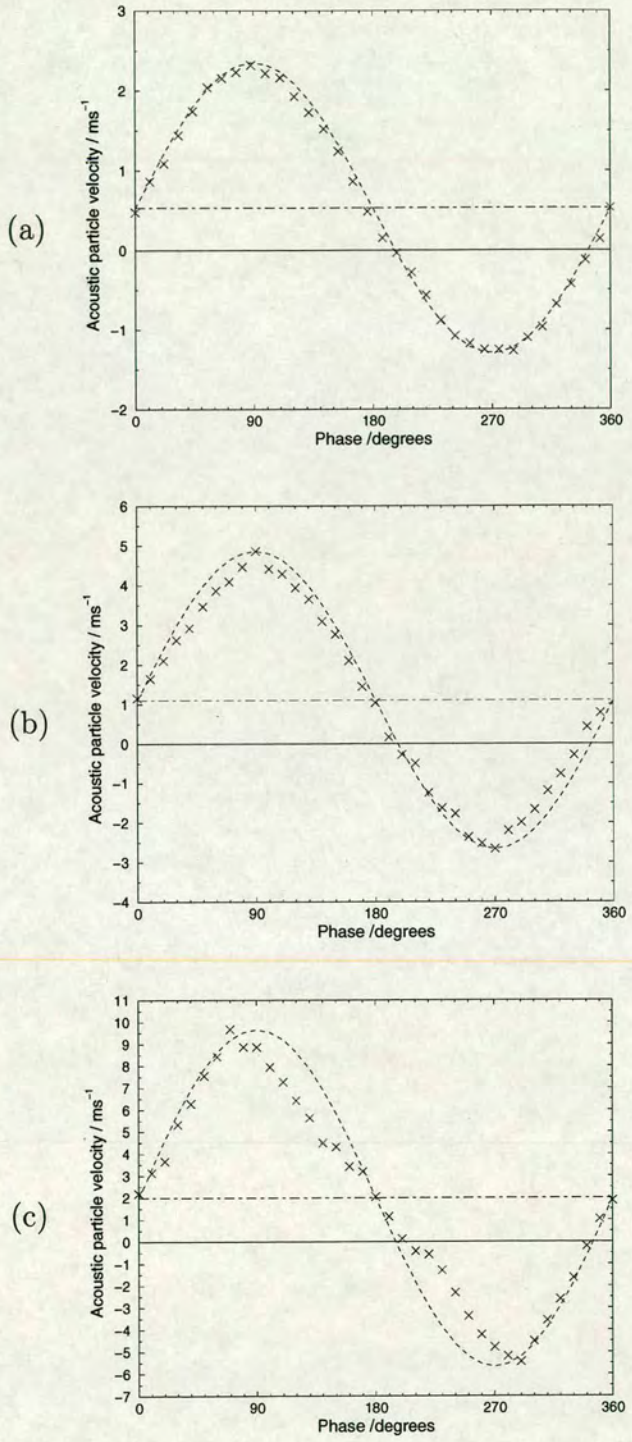

Figure 6.8: Acoustic velocity amplitude as a function of phase angle within the acoustic cycle, for three sound intensity levels, measured 1.3mm outside the tube on the tube axis, of (a)130dB, (b)136dB and (c)142dB. – – – indicates the superimposed steady flow velocity V_{st}.

linear regime, flow separation is observed at the inner edges of the tube, resulting in a strong jet directed out of the tube during outflow. During inflow, a much smoother motion is seen as illustrated in figure 6.1. Hence, the flow velocity along the tube axis outside the tube is expected to be asymmetric, with a 'mean flow' superimposed onto the sinusoidally varying velocity signal due to the presence of the jet as observed. Given that the opposite end of the tube was closed by the loudspeaker, it was assumed that the 'mean flow' observed along the tube axis was compensated for by an inward flow at the tube edges, resulting in zero net flow out of the tube. This was, however, difficult to verify quantitatively due to the glare at the tube edges. The magnitude of this mean flow was derived from the difference between the maximum velocities into and out of the tube, and accounted for before calculating the velocity amplitude and phase relative to the reference signal at each intensity level.

Figure 6.8 also illustrates the level of distortion observed in the velocity signal. To quantify this distortion, an FFT was performed on the graphed results, and the second and third harmonic components normalised relative to the amplitude of the fundamental; the results are shown in table 6.2. While it is clear that the distortion increases with higher intensities, the amplitude of the second and third harmonic components remains small relative to the fundamental velocity signal even at an intensity level of 142 dB (figure 6.8(c)). Table 6.2 also shows the normalised harmonic components calculated from an FFT of the pressure signal for the same three intensities. The pressure signal for intensities above 130dB deviates from sinusoidal dependency as the amplitude of the third harmonic becomes increasingly significant. Whilst the normalised amplitude of the second harmonic is comparable with that of the velocity, a significant increase is seen in the third harmonic component.

Sound Intensity Level (dB)	**Normalised harmonic components**					
	Pressure			Velocity		
	1st	2nd	3rd	1st	2nd	3rd
121	1.00	0.00	0.02	1.00	0.00	0.00
126	1.00	0.01	0.07	1.00	0.02	0.01
130	1.00	0.01	0.13	1.00	0.04	0.03
136	1.00	0.04	0.25	1.00	0.05	0.05
142	1.00	0.16	0.38	1.00	0.11	0.10

Table 6.2: Normalised amplitudes of the first three harmonic components for the pressure and velocity signal measured at the open end of the tube. Results are shown for five sound intensity levels.

Once the results had been analysed and values for p, u and ϕ_p-ϕ_u ascertained, the real part of the radiation impedance and hence the non-linear contribution was derived.

From equations 2.7 and 2.8, the acoustic impedance is given by:

$$Z = \frac{p}{U} e^{i(\phi_p - \phi_u)}, \tag{6.6}$$

where p is the amplitude of the sound pressure, and U is the amplitude of the volume velocity out of the cross-sectional area of the tube. Hence, for the case of a thin-walled unflanged tube, the non-linear contribution to the acoustic resistance can be found by subtracting the real part of equation 6.2 from equation 6.6:

$$\begin{aligned} Re(Z_{rnl}) &= Re(Z_r - Z_{rlin}) \\ &= \frac{p}{U} e^{i(\phi_p - \phi_u)} - \frac{(ka)^2}{4} Z_c . \end{aligned} \tag{6.7}$$

The remaining unknown value in equation 6.7 is the volume velocity, which can be ascertained from the PIV velocity maps. Assuming that the flow velocity at the tube exit is radially symmetric about the tube axis, the volume velocity out of the cross-sectional area of the tube can be approximated using the method of integration by summation. Dividing the cross-sectional area of interest into annuli of width $\triangle R$, the volume velocity is then found from:

$$U = \sum_{r=0}^{r=a} 2\pi r. \triangle R.U_r \tag{6.8}$$

where $\triangle R$ is equal to the spacings between PIV grid points on the velocity maps (equivalent to 16 pixels for a 32 $\times$ 32 interrogation area) and the acoustic velocity, U_r, is the velocity value found at each grid point.

Results

Figure 6.9 shows the acoustic resistance as a function of exit velocity for the copper tube. The results found by Atig [9] using the two microphone method are also shown, along with the corresponding values assuming a linear regime, both for a thin-walled tube (equation 6.2) and a tube with an infinite flange (equation 6.3). The main source of error in the calculation of the radiation impedance at each point was found to be due to the measurement of the phase difference ϕ_p-ϕ_u, with errors ranging from 0.6^o to 5.2^o.

The results show that the acoustic resistance is dependent on the sound intensity level, as shown by previous experimental studies, increasing with acoustic exit velocity for levels above $1\,\mathrm{m\,s^{-1}}$. Comparison with the results by Atig [9] shows that although the present measurements are consistently higher, the points fol-

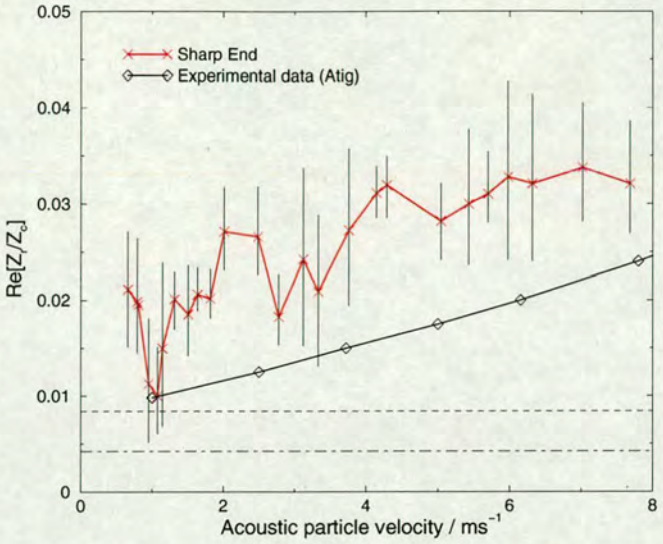

Figure 6.9: Acoustic resistance as a function of velocity at the tube exit. Experimental results are compared to results obtained by Atig [9] using the two-microphone method. The corresponding values, assuming linear conditions, are also shown for the case of an unflanged thin-walled tube (– – –) and a tube with an infinite flange (- - -).

low a similar trend. It is noted that the results should not be expected to show exact agreement due to differences in the tube termination. Unlike the unflanged tube used in the above experiment, the experimental configuration used by Atig featured a small flange at the tube termination. Contrary to the observed results, theoretical studies suggest that the addition of a small flange yields slightly higher values of the acoustic resistance.

It is interesting to note that the measured values appear to initially decrease with increasing exit velocity (for velocities below $1\,\mathrm{m\,s^{-1}}$). A similar observation was made by Atig for the case of a tube with rounded edges and acoustic exit velocities up to $\approx 4\,\mathrm{m\,s^{-1}}$. However, problems were encountered with obtaining valid PIV data at levels below $1\,\mathrm{m\,s^{-1}}$, as reflected by the large error bars at these points. Due to the weakness of the sound field at the tube exit, it was difficult to obtain homogeneous seeding around the area. This resulted in areas around

the tube axis where there were too few particles to obtain a good signal-to-noise ratio.

It is clear from the above calculations that the value of the phase angle between the pressure and velocity has a significant effect on the final value of the real part of the radiation impedance, as indicated by the error bars on the graph. However, the results do show that, at the intensity levels investigated, PIV can be used to calculate these values at the open exit of a tube, producing results which show the same general trend as measurements obtained using other techniques.

The advantage of using PIV to measure the acoustic field at the tube termination is that it allows not just the radiation impedance to be obtained, but also permits determination of further acoustic quantities such as the vorticity. This is described in the following section.

6.3.5 Vorticity

As discussed in section 6.1, vorticity, and in particular vortex shedding, is an important feature of the acoustic flow at the exit of a tube, especially for a tube with sharp inner edges.

The vorticity, $\vec{\omega}$, of fluid motion is defined as [97]:

$$\vec{\omega} = \nabla \times \vec{u} \tag{6.9}$$

where the velocity vector $\vec{u} = (u, v, w)$. For the case of a two-dimensional PIV velocity map, it is only possible to obtain the component of vorticity along the

z-axis (perpendicular to the light sheet), such that

$$\omega_z = \frac{\partial v}{\partial x} - \frac{\partial u}{\partial y} \tag{6.10}$$

The vorticity was calculated at each grid point on the velocity map using a C-program written by Haydon [48]. This used a simplistic algorithm which considered the four closest neighbours to determine velocity differentials in the x (axial) and y (radial) directions.

Although more sophisticated techniques for calculating vorticity exist, which attempt to reduce errors associated with the calculation of differentials by including a higher number of neighbouring points, such as that proposed by Nogueira [74], it was considered that this was unnecessary for the purpose of this study.

Figure 6.10 shows the vorticity contour plots at four different times in the acoustic velocity cycle of period T. Time t=0 is defined as the point in the cycle where the acoustic velocity is a minimum at the tube exit, with t=0.25T and t=0.75T describing the points when the acoustic velocity is at its maximum, during outflow and inflow respectively. The unit of vorticity in all plots is s^{-1}, with positive (counterclockwise) vorticity represented by the red-coloured regions, and the negative (clockwise) vorticity shown in blue. Due to the illumination of the solid tube from the right hand side, no valid vorticity values were available on the left side of each image below the level of the tube exit. The elongated red sections shown just above and orientated parallel with the top of the tube are also invalid vorticity values due to glare from the top of the tube.

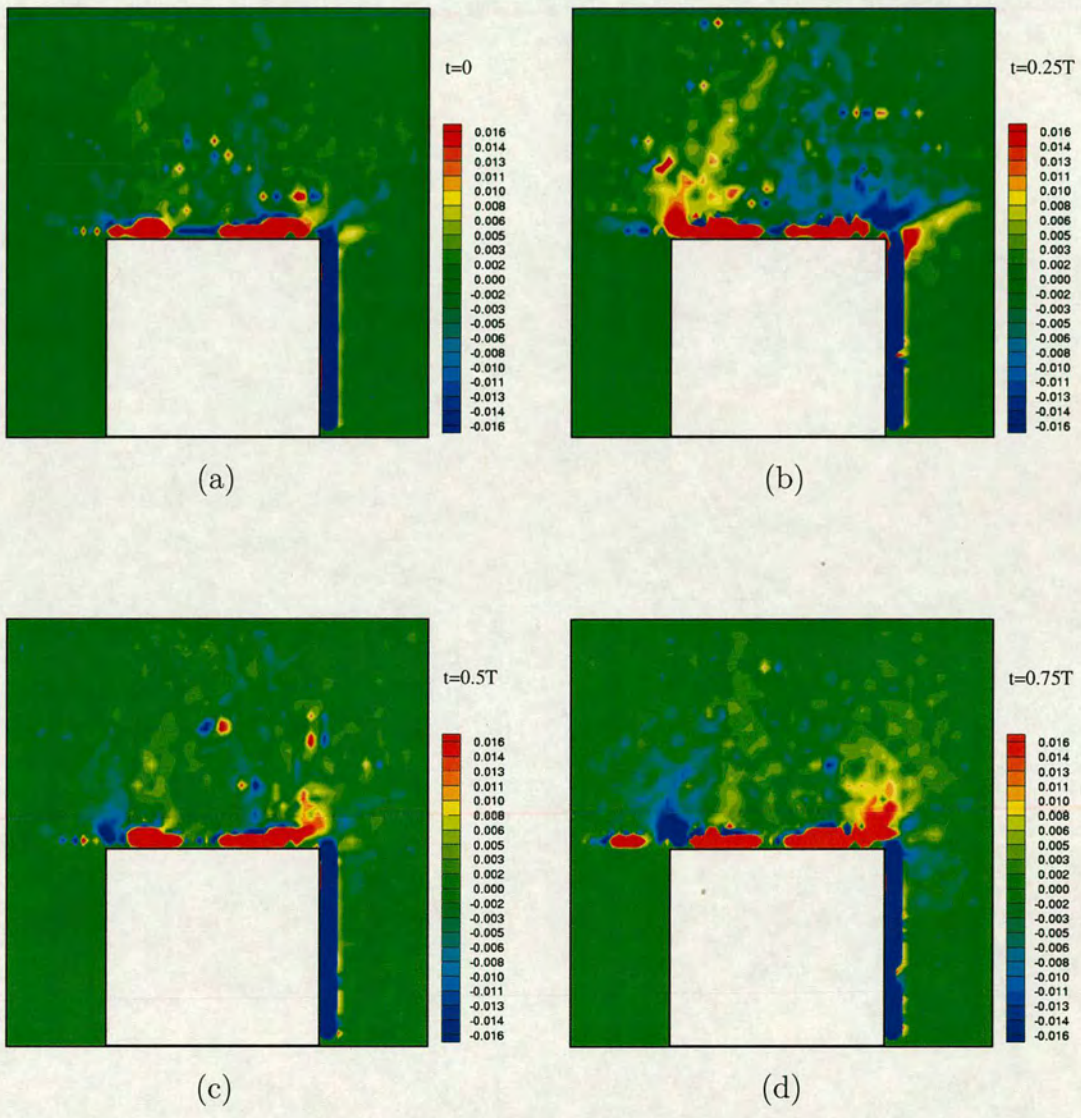

Figure 6.10: Vorticity (s^{-1}) of the acoustic field at the tube exit, with an intensity at the tube exit of 130dB, at times (a) t=0 (b) t=0.25T (c) t=0.5T and (d) t=0.75T. The area in white indicates the position of the tube.

Figures 6.10(a) and (c) show vorticity contour maps at times when the acoustic velocity through the tube exit is zero (t=0, t=0.5T). Only a small amount of vorticity is observed outside the tube in both cases. This is mainly concentrated at the edges of the tube walls, with a few pairs of small vortices also visible in the region above the tube.

Figure 6.10(b) shows the contour map when the acoustic velocity is at its maximum amplitude, directed out of the tube (t=0.25T). A significant amount of vorticity is seen outside the tube exit, observed up to the top extreme of the image, with strong vortical motions observed at the tube edges rotating in opposite directions. A jet of vortical motion is also seen moving away from the right hand corner of the tube; this may also exist on the opposite side, but would not be visible due to the limitations described above.

Figure 6.10(d) shows the contour map half an acoustic cycle later, when the acoustic velocity is at its maximum amplitude, directed into the tube (t=0.75T). As can be seen, there is significantly less vorticity outside the tube exit. Strong vortices are observed at the tube edges as before, but rotating in the opposite direction, commensurate with the change in flow direction.

Once the vorticity has been calculated, the energy transfer (representing sound absorption or sound production) associated with its interaction with the acoustical field can be ascertained. This has important implications for the study of musical instruments (especially woodwind and flue instruments), where vortex shedding has been correlated with the playing amplitude and spectral distribution, and hence the timbre of the sound produced by the instrument [37]. Although such calculations are currently being undertaken in the acoustics group at Edinburgh University, this is beyond the scope of the work presented here.

6.4 Conclusions

Previous theoretical and experimental studies by various authors have shown that at relatively high acoustic levels, significant non-linear behaviour is observed at the exit of tube terminations. In particular, the acoustic resistance (the real part of the radiation impedance), which is constant in a linear regime, was found to increase proportionally with exit velocity.

Although recent measurements of the acoustic resistance have been obtained using the two-microphone method, a new approach was proposed using PIV in conjunction with pressure measurements to acquire the necessary data. This has the advantage of providing direct velocity values rather than deriving these from pressure signals.

The procedure for measuring the acoustic resistance at the tube termination using PIV was presented. In order to check the validity and accuracy of the technique, preliminary measurements of the phase amplitude between the pressure and velocity were made for a standing wave in a closed-end tube with acoustic fields of intensities in the range 145-155dB. The mean phase amplitudes for the three different sound intensities were found to agree with theoretical results to within an error of 2.5^o.

Using an experimental configuration similar to that used by Atig [9], the magnitude of the acoustic resistance was then measured at the exit of an open tube for a range of acoustic exit velocities corresponding to intensity levels at the tube exit of 121-142dB. The results clearly showed a dependence of the acoustic resistance on the sound intensity level, as expected. Comparison with the results obtained by Atig for a sharp-ended tube using the two-microphone method showed a sim-

ilar trend, although the measurements using PIV were found to be consistently higher.

Using the PIV velocity maps obtained for the radiation impedance measurements, the vorticity of the acoustic field at the tube exit was calculated. For a sound intensity level of 130dB, a significant vortical motion was observed throughout the area adjacent to the tube termination. The vortical motions were largest when the magnitude of the flow velocity was at a maximum, directed both in and out of the tube.

The work presented in this chapter is significant, not only because it broadly confirms previous measurements of radiation impedance using indirect measurement techniques, but because it also highlights the additional benefits of using PIV. Unlike indirect techniques, where the acoustic behaviour is inferred, the full-field velocity measurements obtained using PIV provide the ability to ascertain further quantitative acoustical parameters such as energy losses directly. The mechanisms responsible for the energy losses could also be investigated by further analysis of the velocity maps.

Chapter 7

Measurement of acoustic streaming at side holes

7.1 Introduction

This chapter considers the application of PIV to the measurement of the acoustic streaming motion found at the side holes of a woodwind instrument under playing conditions. The study of side holes is closely linked to that of tube terminations, as discussed in chapter 6, where the interaction of the flow with the walls at the opening in the tube can significantly change the behaviour of acoustic fields close to the tube exit. In the case of woodwind instruments, this can lead to a change in timbre of the sound produced, as well as affecting the ease with which the instrument can be played.

After a brief recapitulation of previous experimental and theoretical work on the tone holes of woodwind instruments, pressure measurements in the vicinity of the tone holes of a Boehm flute are taken to ascertain the sound intensity levels found under normal playing conditions. The chapter then continues with

a study of the streaming motion at the side holes of three tube configurations, having similar geometries to that of a Boehm flute, using PIV and supplementary pressure measurements. Measurements obtained over a range of frequencies and intensity levels are used to obtain qualitative information about the streaming behaviour found at a single side hole and two double-hole configurations under realistic playing conditions.

7.2 Background

One of the earliest investigations of tone holes was made by Boehm [15]. Using acoustic theory in conjunction with practical trials, he calculated the tone hole positions necessary to produce an even tempered scale on the flute, which are still close to the values used today.

Later authors [12, 57, 71, 72] showed that the acoustical behaviour of a woodwind instrument can be generally represented by a transmission line, with the effects of each tone hole represented by series and shunt impedances. The values of the respective impedances varies depending on whether the holes are closed or open, and in addition, for the latter case, whether a key or finger is suspended over the hole. Using this theory, Benade [12] calculated the correction to the geometrical tube length associated with the presence of a combination of open and closed tone holes together with bore perturbations. A more extensive study was carried out by Nederveen [72], involving theoretical and mathematical calculations on the position of tone holes for a whole range of woodwind instruments.

Although this approach was reasonably accurate, deviations between theoretical results and experimental observations demonstrated a need for additional internal and external corrections to the shunt and series impedances associated with each hole. This effectively introduced local changes in inertance and compliance [71, 73]. These changes accounted for details such as the small matching volume arising from the curved surface interface between the main bore and tone hole, and the radiation impedance of the tone hole. These internal and external corrections were experimentally determined for specific practical situations by Benade and Murday [14], Coltman [22] and Keefe [58]. The corrections were theoretically determined using modal decomposition by Keefe [56, 57] and Dubos et al. [29], and a finite difference method by Nederveen et al. [73].

Extending his work with single tone holes, Keefe [58] continued on to examine the effect of internal and external interactions between the sound pressure fields at adjacent tone holes. For a tube of internal diameter $2a$, with tone holes of diameter $2b$ and interhole separation $2s$ (measured centre to centre), as illustrated in figure 7.1, he defined two important parameters linked with the internal and external interactions of the holes, an internal interaction parameter δ and an external interaction parameter, ϵ;

$$\delta = \frac{2a}{2(s-b)} \tag{7.1}$$

and

$$\epsilon \simeq \frac{1}{4}\left(\frac{b^2}{2st_e}\right) \text{ for } 2ks \ll 1\,, \tag{7.2}$$

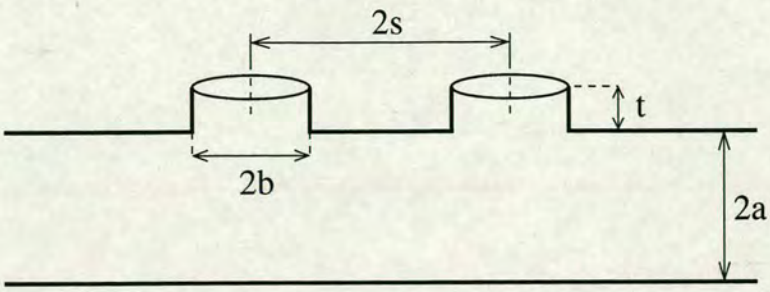

Figure 7.1: Diagram of a tube with two identical side holes of diameter $2b$, positioned on the side of a main bore of diameter $2a$. The centre-to-centre hole separation is $2s$, and the distance between the two closest edges of the tube is $2(s\text{-}b)$.

where, for low frequencies, the open hole effective length t_e for a single hole without a pad suspended above and with chimney height t, is given by

$$t_e = t + b[1.4 - 0.58(b/a)^2]. \tag{7.3}$$

Keefe found that the interactions were most significant for large diameter holes, where the separation between tone holes was small when compared to the diameter of the main bore. He observed an apparent increase in both the internal and external couplings with a pad suspended above the holes. He also showed that for a woodwind instrument under normal playing conditions, acoustic streaming and convective nonlinearities were generated due to the viscous interaction between the sound field and the inner walls and edges of the tone holes. The strength of these interactions was determined by the geometry and separation of the tone holes. These were found to have very prominent effects on the tone produced by the instrument, especially for notes in the lower register.

7.3 Investigation of acoustic streaming motion at side holes

The aim of the experimental work described below was to obtain qualitative information about the streaming behaviour in the vicinity of side holes, using a simplified experimental configuration based on the geometries of a modern Boehm flute.

A detailed investigation of all the effects associated with the behaviour of acoustic fields around tone holes is beyond the scope of this work. The preliminary investigation focused on two important effects noted by Keefe [58], namely acoustic streaming and the effects of internal and external coupling between the sound fields under playing conditions. In order to simplify the situation further, a simple cylindrical tube was chosen with holes drilled through the side. To draw some comparison with a real instrument, the geometry of the main bore and side holes were chosen to replicate that found on a modern Boehm flute. The specific aims were then threefold:

- to establish the sound field intensity found at the tone holes of a modern Boehm flute under normal playing conditions
- to investigate the acoustic streaming velocities observed for single and multiple tone hole configurations
- to investigate the effects of internal and external coupling on the sound fields by varying the hole separation

7.4 Determination of the sound playing levels of a Boehm flute

Prior to starting investigations on the acoustic streaming around side holes, the sound pressure levels in the vicinity of the tone holes of a modern Boehm flute under normal playing conditions were measured. This provided an indication of the intensity levels generated during normal playing (necessary for the experiments), as well as allowing quantitative comparison to be drawn between the results and realistic acoustical conditions. A selection of notes, spread over the lower two octaves of the instrument, were played on a standard Boehm flute by a flautist with each note sustained for a few seconds at a mezzo forte (*mf*) level. Using the long probe microphone, the pressure level was obtained at the first open hole away from the flute mouthpiece for each note. Measurements were taken both on the axis of the tone hole approximately 1cm outside the instrument, and under the key pad approximately 5mm inside the main bore of the instrument. The results are shown in table 7.1.

Note	**Frequency**	**Sound Intensity Level(dB)**	
	(Hz)	**1cm outside tone hole**	**inside the instrument**
G_4	392	120	134
B_4	494	120	134
$C\sharp_5$	554	124	137
G_5	784	121	137
B_5	988	124	146

Table 7.1: Pressure measurements taken at the first open tone hole of a modern Boehm flute for a number of notes played at a *mf* level. Values are given for the pressure levels at two positions; on the tone hole axis 1cm outside the instrument, and in the centre of the hole 5mm inside the main bore of the flute.

As can be seen, the intensity levels measured at a small distance outside the tone hole are around 120-124dB, rising to levels of 134dB and higher inside the instrument.

7.5 Experimental method

The experimental configuration used for the flow measurements around the side holes is illustrated in figure 7.2. A cylindrical perspex tube of length 500mm, internal radius 10.4mm and wall thickness 2.2mm was mounted vertically on the JBL loudspeaker in the same manner as before (see section 4.2) with slight modifications to accommodate the smaller tube diameter. The geometry of the tube was similar to that found for a Boehm flute, which has an internal radius of 9.5mm.

Three tubes were constructed with different side hole configurations; in the first tube, a hole of radius 7.5mm was drilled halfway along the length of the tube. The radius of the side hole was chosen such that its ratio to the internal radius of the main bore corresponded approximately to the ratio found on a modern Boehm flute. The other two tubes were designed to investigate the interhole interactions.

From equations 7.1 and 7.2, the internal and external coupling between the sound fields at each tone hole decreases with increasing hole separation. It was therefore decided to investigate the interaction between two closely spaced holes, where coupling of the sound fields at each hole was expected to be high, and two widely spaced holes such that the interaction was much smaller. Considering the

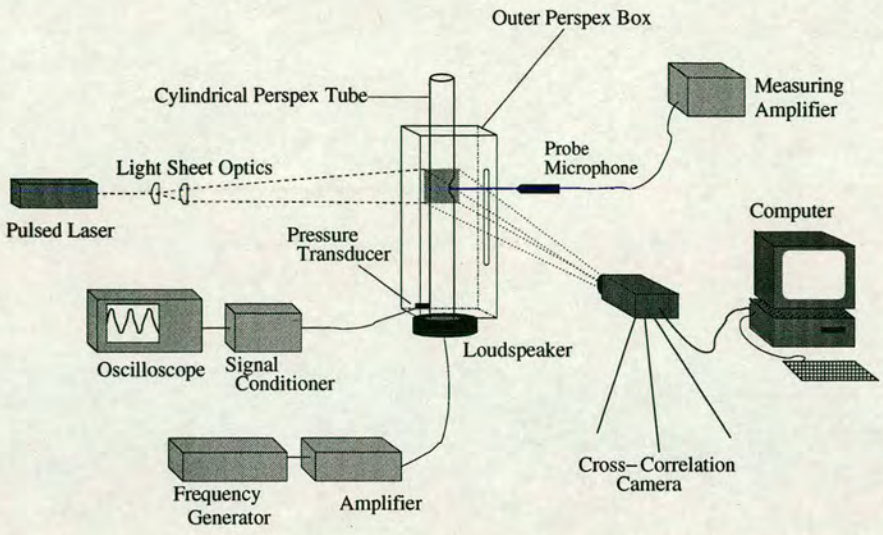

Figure 7.2: Experimental arrangement for taking PIV measurements of the acoustic field in the vicinity of side holes in a cylindrical tube.

problems encountered earlier with the observation and measurement of acoustic fields near the tube walls due to flare (see section 5.5.2), it was decided to concentrate mainly on the external coupling. Hence, in both configurations, the separation of the side holes ($2s$) was made greater than the tube diameter, the condition where internal coupling is considered to be small or negligible [58]. The external hole interactions were found by Keefe to be unimportant when ϵ was of the order of 1%, and important for values of approximately 5%, with the tone hole spacings on a Boehm flute yielding a value of ϵ=4.4%. Hence, the centre-to-centre distance of the closely spaced holes was set to correspond to a value of ϵ=5%. In order to capture both holes on the same PIV image, the maximum separation was limited to the 5cm width of the light sheet used to illuminate the region around the holes. This yielded a value for the external interaction parameter of ϵ=4%.

Two holes, both of radius 7.5mm, were machined into the side of both tubes, separated by a centre-to-centre distance, $2s$, of 27.6mm and 34.4mm respectively, and positioned symmetrically on either side of the halfway point of the main tube. The inner edge of each hole was left with sharp edges.

The internal sound pressure level at the end of the tube nearest the loudspeaker was monitored by a piezo-electrical pressure transducer mounted flush with the inner tube wall as described in section 4.5.3. The output voltage signal was viewed on an oscilloscope and the peak-to-peak amplitude measured. From this, the amplitude of the sound pressure in decibels was obtained using the calibrated sensitivity of the transducer of 0.00448mV/Pa (see section 4.5.3 and equation 2.4). The pressure transducer was positioned a distance of 3.5 cm from the end of the tube to ensure measurements were not taken exactly at the position of the pressure node. This also allowed the natural resonance frequencies of the three tubes to be ascertained; it was assumed that at frequencies corresponding to the resonance, a large pressure maximum would be found near (but not at) the pressure node due to the constructive interference of the reflected acoustic waves from the side holes and open end of the tube.

A rectangular perspex box of height 400mm and cross-sectional area of 200mm $\times$ 120mm with a flange on one end was constructed to retain the seeding particles within the region of the side holes on the tube whilst allowing the open end of the tube to protrude out of the box. This ensured that the resonance properties of the tube were not affected. The box flange was attached to the top of the loudspeaker-tube connector, in a similar manner to that described in section 6.2, such that the side holes were positioned as far away as practically allowable from the box wall in order to minimise boundary effects. The construction of the box

was such that the wall opposite the side holes was interchangeable. This allowed the use of a solid wall for the PIV measurements (required to retain the seeding), and a slotted wall to facilitate microphone access to the side holes.

The PIV apparatus was set up as described in section 4.3.3 and illustrated in figure 4.5, with the light sheet directed vertically through the tube axis and the centre of each side hole. Starting with the single-holed tube, a burning incense stick was held just inside the perspex box for a few seconds to seed the volume around the tube. A standing wave corresponding to the first resonance mode of the loudspeaker-tube combination (f=660Hz) was set up in the tube, driven by an amplified sinusoidal signal.

Once the seeding concentration was evenly distributed throughout the tube, the sound intensity was increased to a level where a mean acoustic motion was observed exiting from the side hole. Pairs of PIV images of separation 1 to 1.5ms were then taken at various intensity levels above and below the intensity corresponding to the onset of this streaming motion, and for a range of frequencies either side of the resonance frequency.

Once the PIV images had been obtained, the light sheet was removed and the wall of the perspex box opposite the side hole replaced by the slotted wall. The long probe microphone was then inserted through the slot and positioned parallel to the main axis of the hole with the probe tip located at its centre. Moving the probe horizontally using a translation stage, pressure measurements were taken at three positions; at the outer wall of the tube (referred to as a distance of x=0mm) and at distances 6mm and 12mm inside the tone hole. The sound pressure level at the base of the tube was also recorded using a pressure transducer. These

measurements were repeated for each frequency and intensity level. The acquired pairs of PIV images were cross-correlated to obtain the velocity maps, which were then validated (as described in section 3.5.5) to remove spurious vectors.

The same measurements were repeated for the tubes with double hole configurations, with sound pressure measurements taken inside both holes.

7.6 Results

In order to visualise the acoustic streaming motion observed for each tube configuration, the resulting PIV velocity maps for each tube are displayed in the form of contour maps of streaming velocity magnitude, with the streaming velocity vectors also shown. The unit of velocity magnitude in all the plots is $\mathrm{cm\,s^{-1}}$, with the highest velocities corresponding to the red-coloured regions, and the lowest velocities shown in blue. The location of the tube and the side holes are indicated in white on the left side of each map, with the loudspeaker located a distance below the bottom of the image. The results for each tube are described separately below.

7.6.1 Single side hole configuration

Figure 7.3 presents the pressure measurements taken at the end of the tube terminated by the loudspeaker and at the centre of the side hole exit (at position x=0mm) over a frequency range of 600 to 800Hz. As discussed previously, a pressure maximum is found at the base of the tube at a frequency of 660Hz, corresponding to the natural resonance of the air column up to the side hole . The

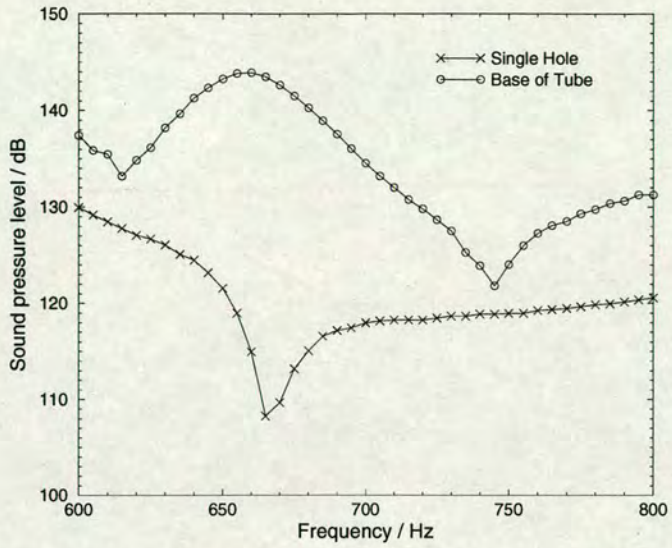

Figure 7.3: Pressure variation as a function of frequency for the tube with a single side hole. Measurements were taken by the pressure transducer at the bottom of the tube (circles) and in the centre of the hole exit level with the tube wall (crosses).

pressure inside the hole is greater at frequencies below the resonance frequency than above it. The pressure variation with increasing frequency showed the same trend both at the hole exit (x=0mm) and at distances of 6mm and 12mm inside the hole

Figure 7.4 shows the streaming velocity contour maps for the tube with the single hole at excitation frequencies at and above the resonance frequency of 660Hz. The intensity level at the base of the tube was 143.9dB at the resonance frequency. The direction of the streaming motion is clearly dependent on frequency. Figure 7.4(a) shows the velocity field at the resonant frequency. At resonance, the jet appears to originate at the top edge of the hole, directed back towards the loudspeaker. Increasing the frequency by 5Hz (figure 7.4(b)), the streaming motion becomes symmetrical, with jets produced at both the top and bottom edges of the hole. The resulting jet is directed straight out of the hole. As

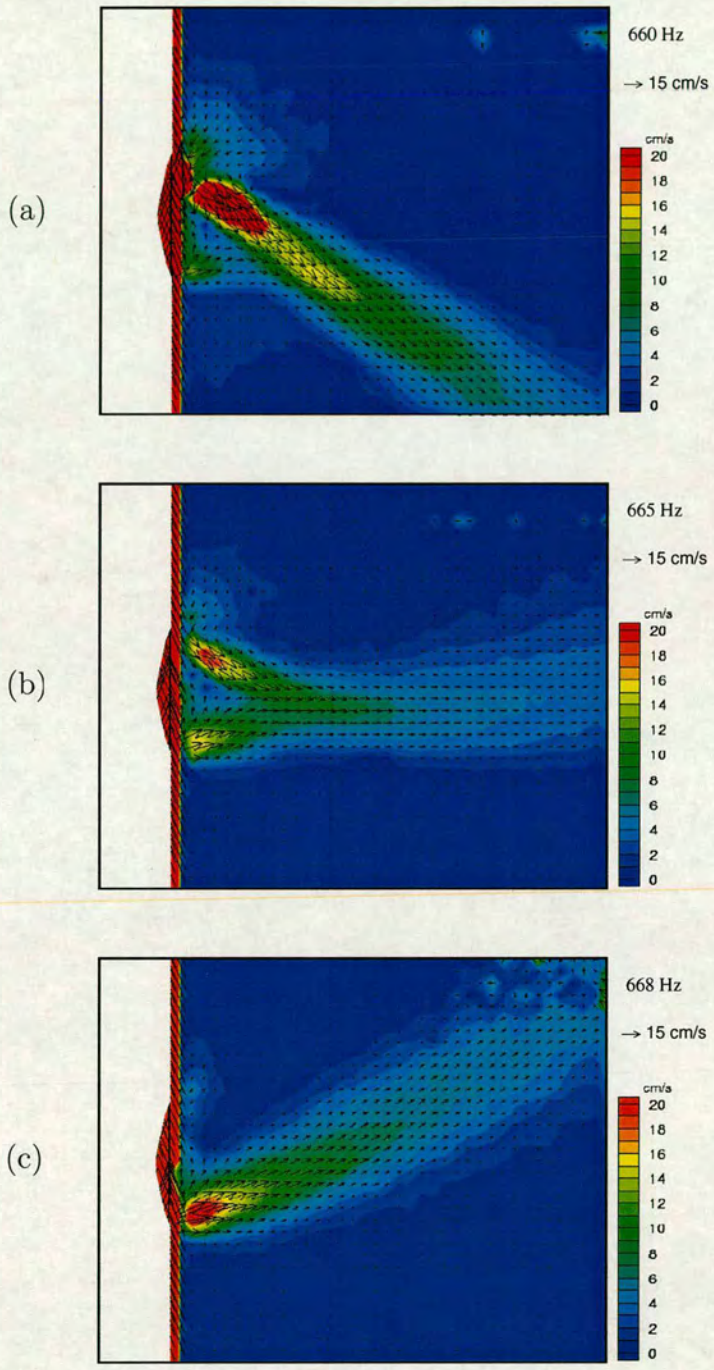

Figure 7.4: Streaming velocity contour maps for the single hole configuration at excitation frequencies of (a)660Hz (resonance) (b)665Hz and (c)668Hz.

the frequency is increased further, (figure 7.4(c)), the streaming velocity becomes stronger at the bottom edge of the hole, resulting in a jet in the same direction as the main flow.

Comparing the results in figures 7.3 and 7.4, the acoustical behaviour of the single hole appears consistent with expectations. For the case of a single side hole in a tube excited at resonance, the pressure node (velocity antinode) of the standing wave will not be positioned exactly at the open hole but a short distance downstream (i.e. away from the loudspeaker) [72]. A strong interaction is therefore likely to occur between the point of maximum acoustic velocity oscillation and the furthest edge of the hole, resulting in a strong streaming motion directed back towards the loudspeaker due to the position of the velocity antinode. As the frequency is increased above resonance, the acoustic wavelength will decrease and hence the position of the pressure node will move back upstream. When the position of the pressure node is located in the centre of the hole (figure 7.4(b)), the flow out will be symmetrical with equal interaction between the sound field and the top and bottom edges of the hole. When the pressure node moves further down the tube again, a stronger interaction is expected between the acoustic field and the bottom edge of the hole, generating a jet in the opposite direction away from the loudspeaker. As the pressure at the hole exit is lower at frequencies above resonance, the strength of the jet is also expected to be weaker, as observed.

Figure 7.5 shows the effect of varying intensity level on the acoustic behaviour at a frequency of 665Hz. The pressure intensities given for figures (a)-(d) were measured at the hole exit (x=0mm) by the probe microphone. No significant streaming motion was observed until an intensity level of 111.7dB (figure 7.5(b)),

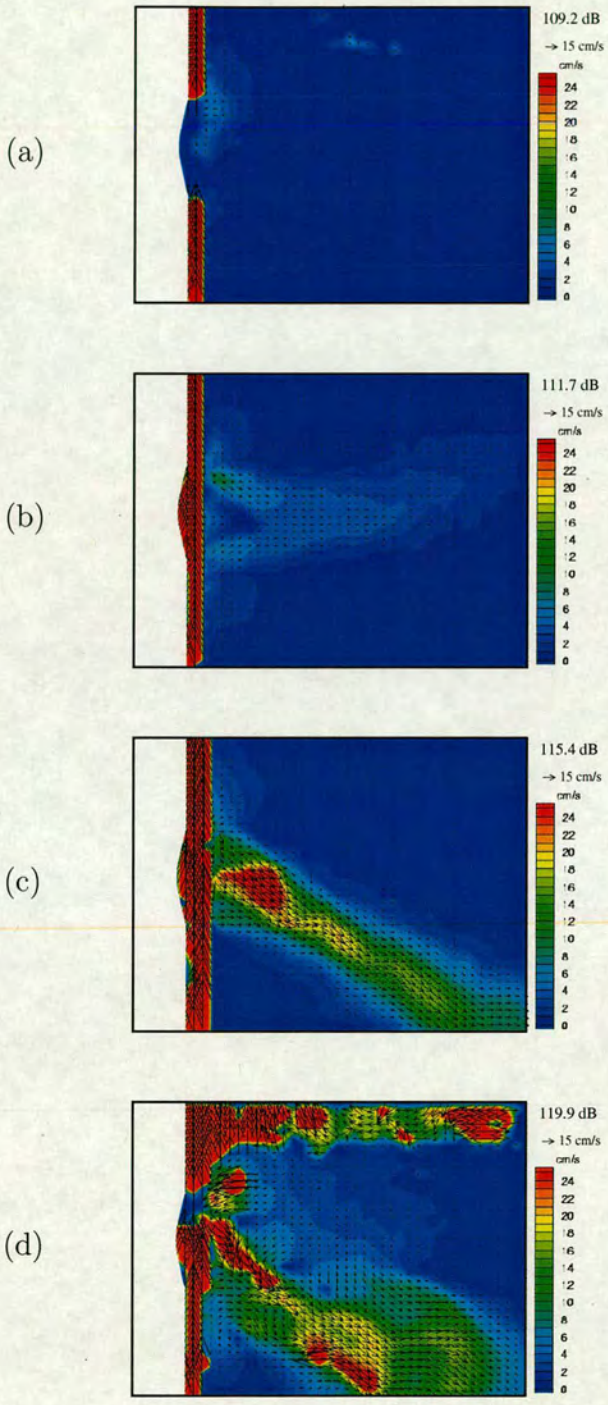

Figure 7.5: Streaming velocity contour maps for the single hole configuration shown for four different intensity levels, corresponding to pressure levels measured at the hole exit (x=0mm).

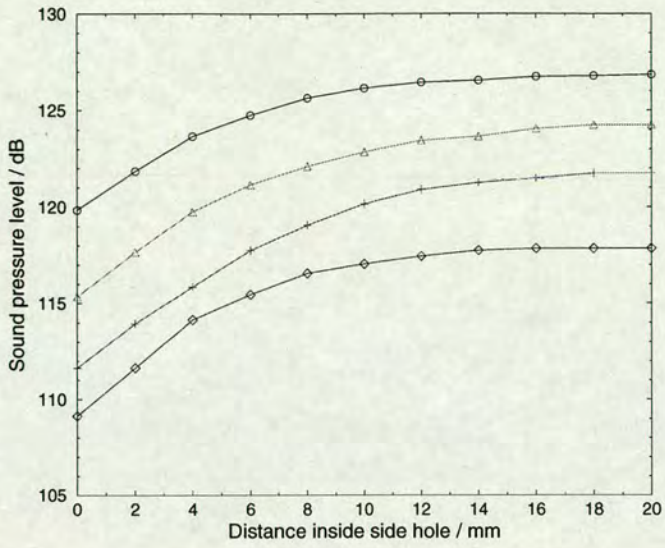

Figure 7.6: Pressure profile as a function of distance inside the centre of the hole for the case of the single-hole tube. The four intensity levels correspond to the intensity levels illustrated in figures 7.5(a)-(d).

when two small jets from the top and bottom edges of the hole coincided to form a weak jet directed straight out of the hole. As the intensity was increased, the direction of the jet became deflected towards the loudspeaker as shown in figure 7.5(c). Finally, at an intensity of 119.9dB (figure 7.5(d)), a strong jet was still observed from the top edge of the hole in the same direction, although the flow behaviour became increasingly turbulent.

The profile of the pressure intensity as a function of distance inside the hole is shown in figure 7.6 for the four intensity levels illustrated in figure 7.5. As can be seen, a large pressure gradient occurs over the first 10mm inside the tube, after which the profile is relatively flat. This response is similar for each intensity, suggesting that the presence of a side hole only significantly affects the pressure field in the half of the tube nearest the hole. This observation appears to be independent of intensity up to and including the onset of turbulent behaviour outside the tube.

7.6.2 Widely-spaced side holes configuration

Figure 7.7 shows the pressure variation with frequency for a system consisting of two widely spaced holes. Measurements were taken both at the end of the tube next to the loudspeaker, and at the centre of each side hole (at position x=0mm inside the hole). Two pressure maxima were found at the base of the tube at frequencies of 650Hz and 690Hz. It was also noted that in most cases the pressure at the lower hole was greater than that at the upper hole, except for frequencies between 668Hz and 688Hz.

The two points where the pressure at both holes is equal define the boundaries of three clear flow regimes:

1. In the first flow regime, at frequencies below 668Hz, the pressure at the exit of the lower hole is greater than that at the upper hole exit.

2. The second flow regime, between 668Hz and 688Hz, shows a reversal of this trend with the greater pressure at the upper hole exit.

3. At frequencies above 688 Hz, the pressure at the exit of the lower hole is again greater, this time by a significant margin.

The streaming velocity contour maps corresponding to a range of frequencies between the two resonance points, and encompassing the three flow regimes described above, are shown in figure 7.8. As before, the acoustic behaviour is very dependent on frequency. In the first flow regime (frequencies below 668Hz), the predominant flow is in the form of a jet from the lower hole, projected in the same direction as the main flow (figure 7.8(a)). A much smaller streaming motion is

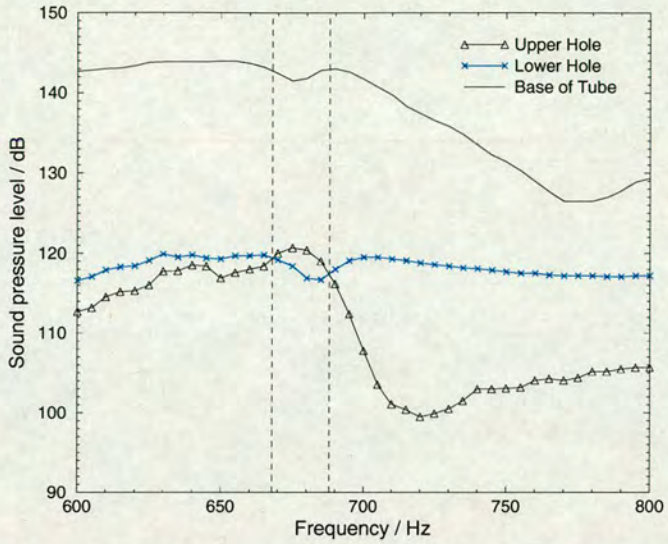

Figure 7.7: Pressure variation as a function of frequency for the tube with two side holes widely spaced apart. The vertical dotted lines indicate the separation of regimes 1,2 and 3.

observed exiting from the upper hole. The magnitude of these effects increases with frequency, as shown in figure 7.8(b).

At 668Hz (the transition between flow regimes 1 and 2, where the pressure at the exit of both holes is equal), two jets of equal magnitude are observed, directed towards each other (figure 7.8(c)). Interaction is seen between the two jets at a distance 20mm away from the tube wall. Increasing the frequency further, thus moving into the second flow regime, the lower jet is observed to become gradually weaker whilst the jet out of the upper hole increases in strength as seen in figure 7.8(d).

At 690Hz, (corresponding to the second resonance frequency, and in the third flow regime), the strong jet out of the upper hole abruptly vanishes as shown in figure 7.8(e), with just a small jet seen exiting the lower hole. At frequencies above 690Hz, a jet was again observed exiting out of the upper hole whose direction

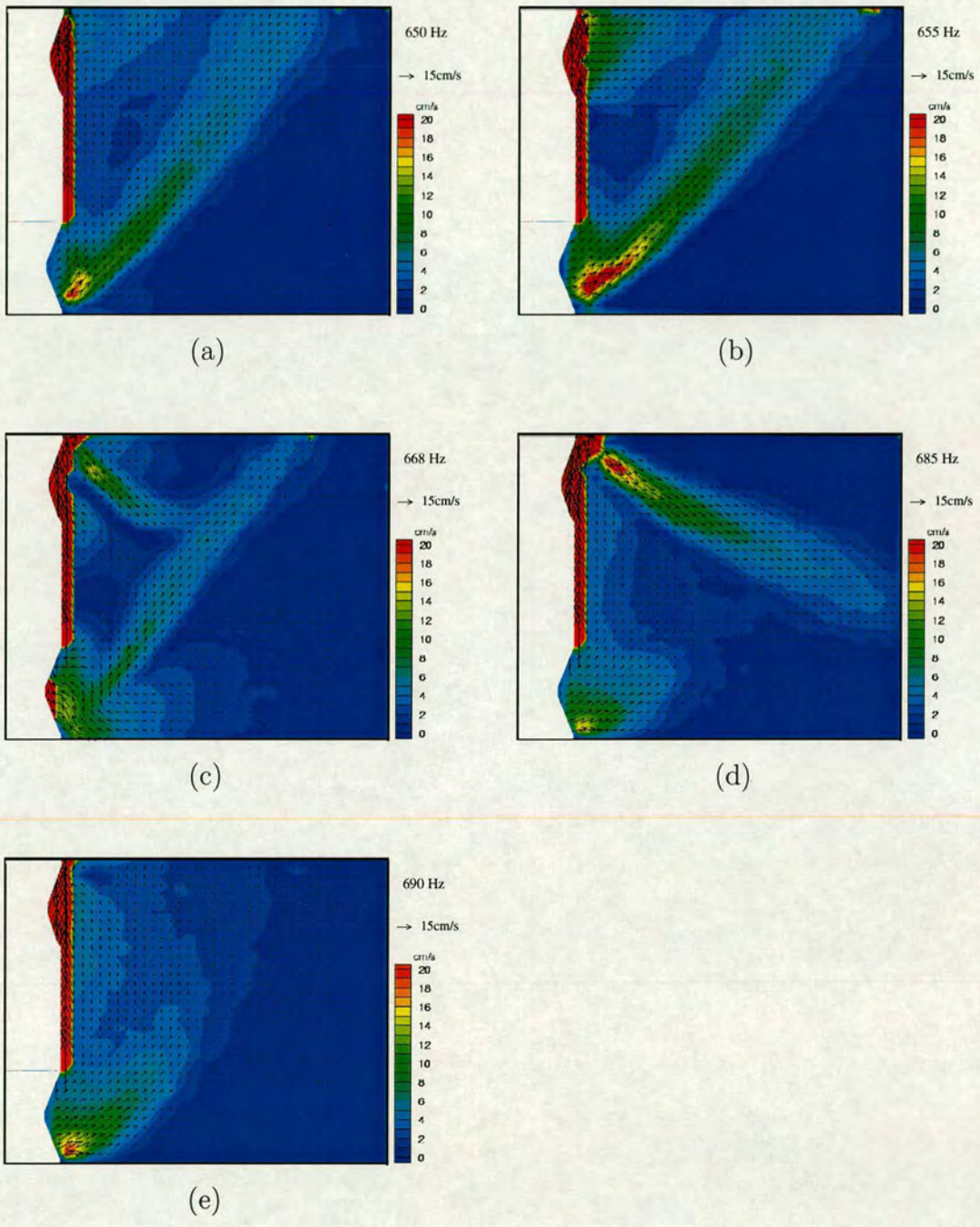

Figure 7.8: Streaming velocity contour maps for the widely spaced double-hole configuration at excitation frequencies of (a)650Hz (lower resonance frequency), (b)655Hz, (c)668Hz, (d)685Hz and (e)690Hz (upper resonance frequency).

continued to move upwards with increasing frequency until it was projected in the same direction as the main flow. The behaviour of the jet out of the lower hole remained the same.

It is clear from the results presented in figures 7.7 and 7.8 that the pressure at both holes strongly determines the behaviour of the acoustic streaming in the vicinity of both holes. Unlike the case of the single hole, the direction of the jet out of the lower hole was always observed to be travelling in the same direction as the main flow. It is clear that the acoustical situation for the case of the two holes is much more complicated than that observed for a single hole.

In order to examine the interaction between the acoustic streaming produced at each side hole further, the excitation frequency was set at 688Hz, (corresponding to the transition between the second and third flow regimes) and the intensity level varied; the results are shown in figure 7.9. Significant interaction between the two jets was not seen until an intensity level (measured at the lower hole exit at x=0mm) of around 124dB (figure 7.9(d)), when the flow behaviour between the positions of the two holes became turbulent.

Figure 7.10 shows the pressure intensity profile as a function of distance inside the hole for an excitation frequency of 690Hz (the second resonance frequency) and a range of intensity levels. A similar behaviour is observed in both the lower and upper hole for each intensity level, with a large pressure gradient occurring over the first 12mm inside the tube, and a much flatter response over the remaining distance to the internal tube wall. The form of the pressure profile over the tube diameter is comparable with the pressure variation observed for the single hole configuration. A similar response was also found at 650Hz.

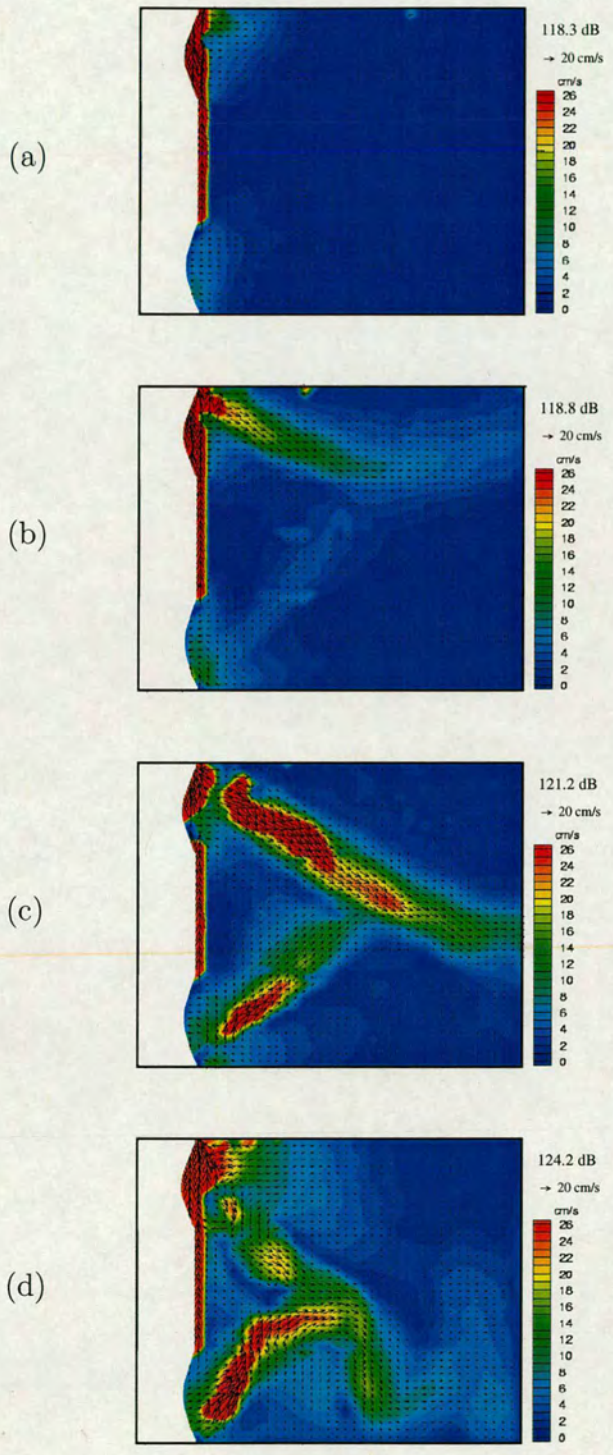

Figure 7.9: Streaming velocity contour maps for the widely spaced double-hole configuration at an excitation frequency of 688Hz. Results are shown for four different intensity levels, measured at the lower hole exit (x=0mm).

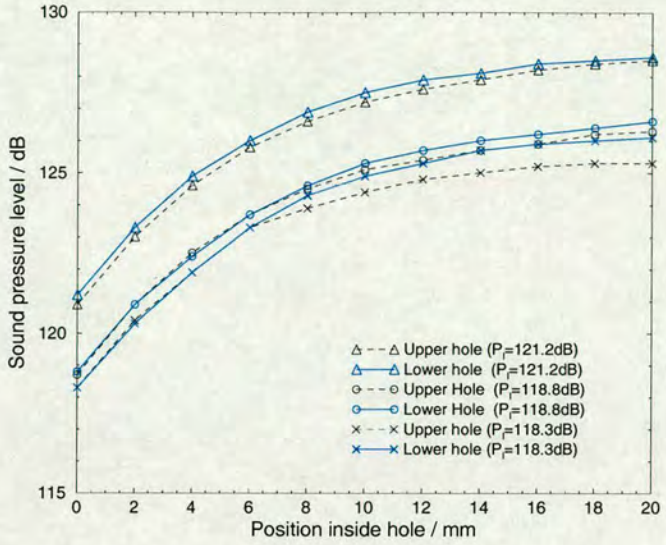

Figure 7.10: Pressure profile as a function of distance inside the centre of the lower and upper hole of the widely-spaced side hole configuration. The three intensity levels correspond to the intensity levels illustrated in figures 7.9(a)-(c), where P_l indicates the pressure at the lower hole exit (x=0mm).

7.6.3 Closely-spaced side holes configuration

For the case of the closely spaced side holes, measuring the pressure variation with frequency both at the end of the tube nearest the loudspeaker and at the centre of each side hole exit (at position x=0mm) produced similar results to those shown in figure 7.7 for the widely spaced holes. Two pressure maxima were found at the base of the tube at frequencies of 625Hz and 680Hz.

The frequency-pressure response curve encompassing the two resonance frequencies is shown in figure 7.11, with pressure measurements taken at the end of the tube near the loudspeaker and at the centre of each side hole exit (x=0mm). In accordance with observations for the widely spaced holes, the pressure at the lower hole remained higher than that at the upper hole, except for frequencies between 660Hz and 684Hz. As described for the case of the widely spaced holes, these points define the boundaries of three flow regimes, as shown on figure 7.11.

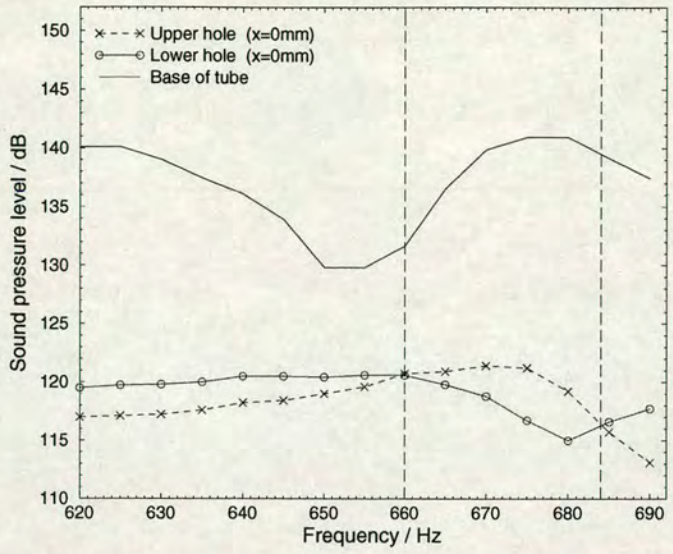

Figure 7.11: Pressure variation as a function of frequency for the tube with two side holes closely spaced apart. The vertical dotted lines indicate the boundaries of flow regimes 1,2 and 3.

In order to observe significant streaming motion out of the two holes, it was necessary to increase the intensity level measured at the base of the tube by 3dB compared to the levels required in the case of the widely spaced holes. The streaming velocity contour maps corresponding to the range of frequencies surrounding the higher resonance point and including all three flow regimes is shown in figure 7.12. In contrast to the results observed with the widely spaced holes, no significant streaming motion (in the form of a jet) was seen out of the bottom hole, even applying a higher intensity excitation signal at the base of the tube. However, the acoustic motion is still clearly dependent on frequency.

In the first flow regime (frequencies below 660Hz), strong streaming motion of equal magnitude is observed at the exit of both holes, but attenuates quickly with distance from the holes (figure 7.12(a)). At 660Hz (the transition point between regimes 1 and 2), a more rotational motion is observed outside the upper hole, whilst the streaming motion at the lower hole is seen entering the tube

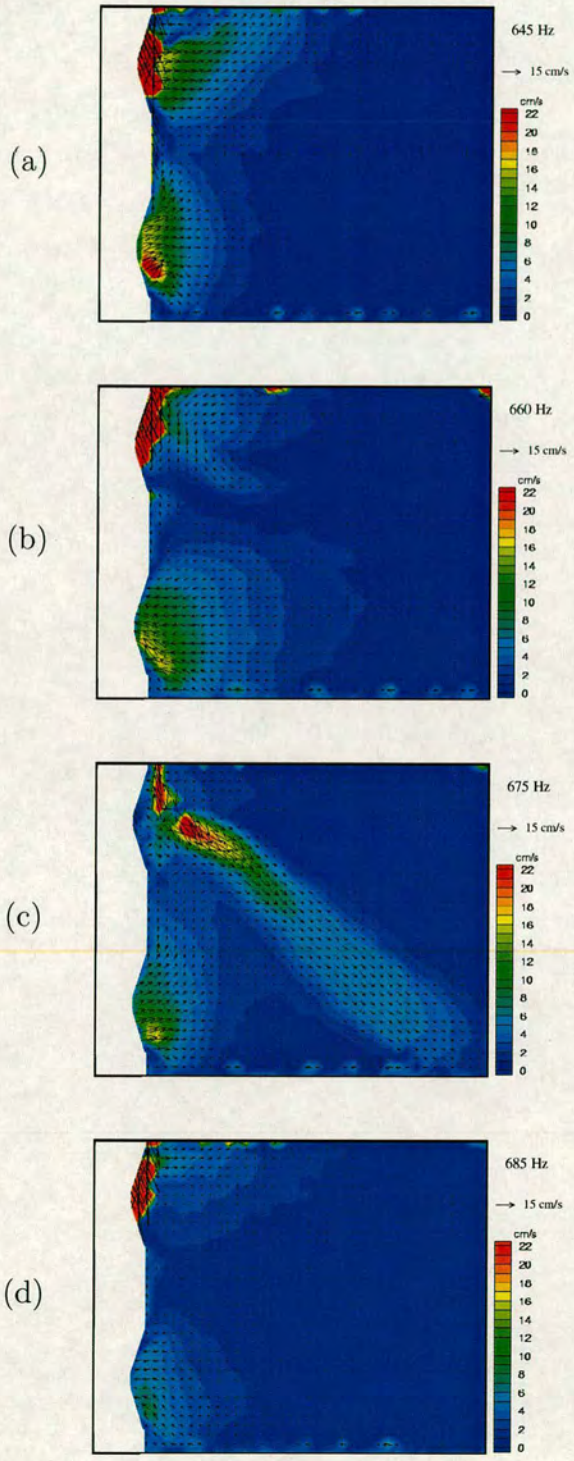

Figure 7.12: Streaming velocity contour maps for the closely spaced double-hole configuration at excitation frequencies of (a)645Hz, (b)660Hz, (c)675Hz and (d)685Hz.

(figure 7.12(b)). Increasing the frequency further into the second flow regime, the prevalent streaming motion is in the form of a jet out of the upper hole, projected back towards the loudspeaker (figure 7.12(c)). A much smaller flow is seen leaving the lower hole, directed upward along the tube wall such that it interacts with the jet near the bottom edge of the upper hole. At 685Hz, (above the second resonance frequency, and in the third flow regime), the strong jet out of the upper hole suddenly disappears, as shown in figure 7.12(d).

A more detailed picture of the acoustic behaviour at and above the higher resonance frequency of 680Hz (in the second and third flow regimes) is shown in figure 7.13. The intensity level at the base of the tube was set 3dB higher than used for the results shown in figure 7.12 to examine the acoustic behaviour more clearly.

In the second flow regime (at frequencies below 684Hz and shown in figures 7.13(a) and 7.13(b)), a strong jet is observed leaving the upper hole projected down towards the loudspeaker, whose strength increases with increasing frequency. The flow out of the lower hole travels up along the tube wall and interacts with the jet near the bottom of the upper hole. At 684Hz, the transition between flow regimes 2 and 3, the streaming motion at both holes abruptly changes as shown in figure 7.13(c); the strong jet out of the upper hole disappears and a smaller rotational motion is seen, whilst flow is only observed entering the lower hole. Increasing the frequency further, hence moving into the third flow regime, a strong jet resumes again out of the upper hole in the same direction as before (figure 7.13(d)). As the frequency is increased further (figures 7.13(e)-(i)), the direction of the jet is gradually deflected towards the horizontal position, while the direction and strength of the flow at the lower hole remains the same.

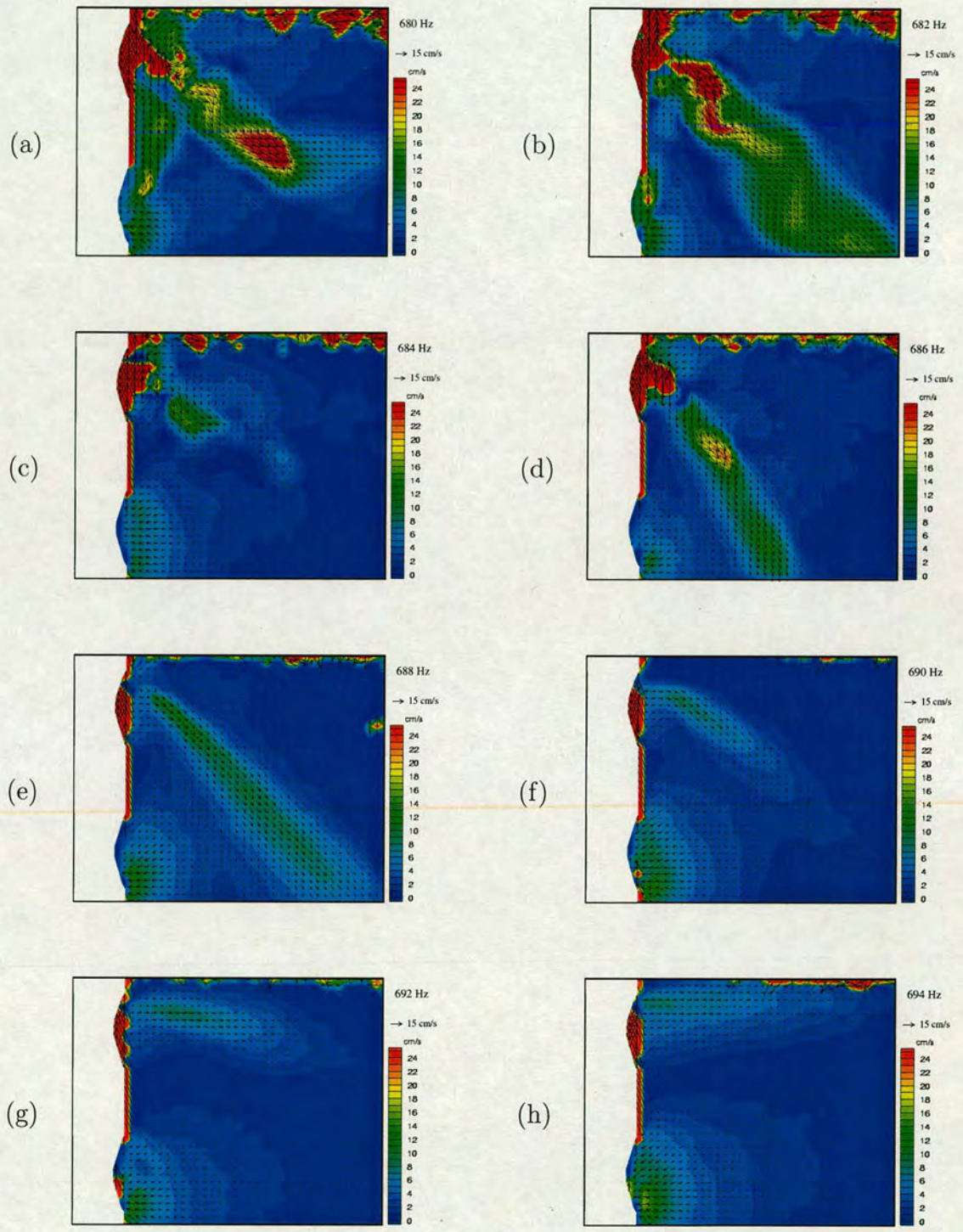

Figure 7.13: Streaming velocity contour maps for the closely spaced double-hole configuration at excitation frequencies in 2Hz steps from 680Hz to 694Hz ((a)-(h)).

As observed in figures 7.12 and 7.13, interaction between the streaming motion out of the two holes was only observed for frequencies between 675Hz and 682Hz, in the second flow regime when the pressure at the upper hole was greater than that at the lower hole. In order to quantify the intensity level when interaction occurred between the two jets, an excitation frequency of 678Hz was chosen, and the intensity level varied as before; the results are shown in figure 7.14.

As can be seen, although a small amount of interaction occurs between the two jets at an intensity level (measured at the lower hole exit) of 120dB (figure 7.14(b)), significant interaction is not observed until an intensity level of around 125dB (figure 7.14(c)), when turbulent flow behaviour in the vicinity of the upper hole is observed.

Measurements of the pressure variation as a function of distance inside the upper and lower hole with increasing intensity, at the two resonance frequencies of 625Hz and 680Hz, yielded results commensurate with those found for the single hole and widely spaced hole configurations (shown in figures 7.6 and 7.10).

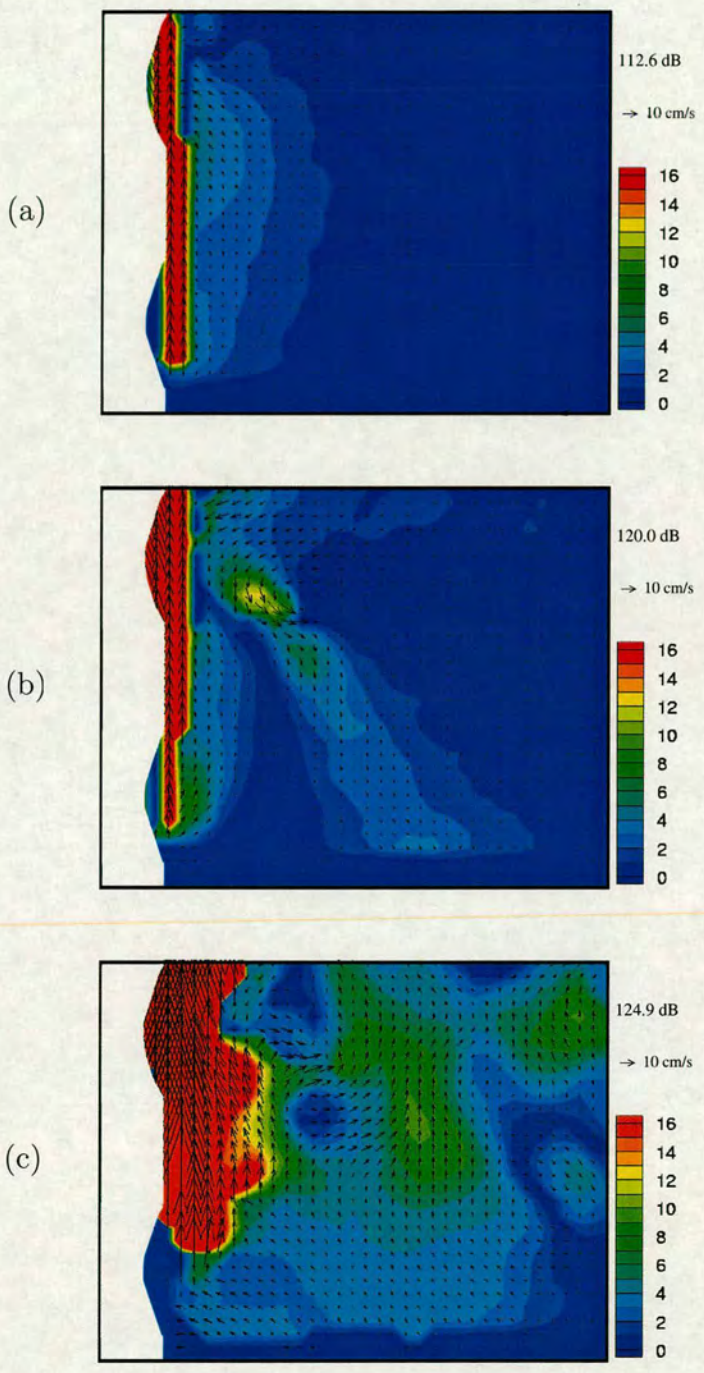

Figure 7.14: Streaming velocity contour maps for the closely spaced double-hole configuration at an excitation frequency of 678Hz. Results are shown for three different intensity levels, measured at the lower hole exit (x=0mm).

7.7 Discussion

The streaming behaviour at the single hole as a function of frequency appears to be relatively straightforward. However, it is clear from the results that the streaming motion with multiple-hole configurations is much more complex.

The observation of two pressure maxima at the base of the tube for the two double-hole configurations suggests that the tubes have two resonance frequencies. The higher frequency is presumed to correspond to the length of the air column from the base of the tube to the first open hole. The lower frequency seems likely to be associated with the length of the air column up to the second open hole. In order to check these assumptions, the theoretical resonance frequencies of the tube were calculated for the three tube configurations used. Calculations were performed to a first approximation using an approach discussed by Nederveen [72], whereby the tube and side holes are considered as a combination of series and parallel branches. Using Kirchoff's acoustic laws for a branched tube, and determining the hole impedance from its length and cross-sectional area, the effect of each hole on the side of a tube was considered and used to calculate the length of a tube without holes (often referred to as a "substitution" tube) necessary to produce the same note as the tube with holes. Knowing this tube length and assuming the end of the tube nearest the acoustic source acts to a large extent as an open end (as discussed in section 5.6), the resonance frequency can then be ascertained. The results are shown in table 7.2.

Although reasonably good agreement is found between the calculated and measured resonance frequency for the tube with the single hole, the calculated resonance frequencies for the two double-hole configurations are higher than the

Configuration	**"Substitution" tube length (mm)**	**Resonance Frequency (Hz)**	**Measured Resonance Frequencies (Hz)**
Single Hole	254.2	669.3	660
Double Hole (closely spaced)	240	709	625 / 680
Double Hole (widely spaced)	236.6	725.5	650 / 690

Table 7.2: Substitution tube length and corresponding resonance frequency for the three tube configurations, calculated to a first approximation using a method outlined by Nederveen [72], compared with the measured resonance frequencies.

two measured resonance frequencies in each case. However, the calculation does not include corrections for the additional partial reflections occurring at both holes, boundary layer effects at the walls, etc, as discussed in section 7.2. In order to completely verify the resonance frequencies would require a more complex numerical calculation, and is considered beyond the scope of this work. For the extent of this work, however, it is reasonable to assume that the resonance frequencies of the single hole, closely spaced double hole and widely spaced double hole configurations are 660Hz, 680Hz and 690Hz respectively.

The initial expectation was that the streaming motion would be predominantly emitted from the first hole away from the excitation source (the lower hole shown in each image) when excited at the natural resonance of the tube, with smaller streaming velocities observed at the second (upper) hole further away from the acoustic source; this followed observations by Keefe [58] for the steady streaming flows observed at the side holes of a clarinet air column, as well as observations by the author for similar woodwind instruments. However, the results

described above for the two double-hole configurations indicate different results. At frequencies above and below the higher resonance for the widely spaced holes of 690Hz (assumed to correspond to the natural resonance of the air column), the streaming motion out of the upper hole was observed to be more significant than the acoustic motion at the lower hole exit. Exactly at the resonance frequency of 690Hz, however, little or no motion was observed at the upper hole, with the streaming motion emitting entirely from the lower hole, but with a smaller magnitude. For the case of the closely spaced holes, a strong streaming jet was still observed out of the upper hole at the higher resonance frequency of 680Hz, but the streaming motion out of the lower hole was much less significant.

It is difficult to relate the results to those found under normal playing conditions due to excitation by acoustic source rather than jet excitation. However, it was noted by Keefe that the streaming jet out of an instrument was not felt when air was blown through the instrument, but only when the instrument was acoustically excited at resonance. The observations discussed above show that significant streaming behaviour is observed without the presence of a steady air stream such as that produced by an instrument under normal playing conditions. Discrepancies from the observations by Keefe may be due to additional coupling between the streaming motion and the steady air stream. This coupling was briefly discussed by Keefe [58], but not quantified.

Although the streaming motion out of the upper hole is similar for both double-hole configurations, the streaming out of the lower hole appears to be far more dependent on the spacing between the two holes. In particular, it is surprising that no significant streaming jet is observed out of the lower hole for the closely-spaced hole configuration. Considering the fact that no significant

external coupling is observed near the lower hole in the range of frequencies investigated, the most plausible explanation is that this is due to internal coupling between the acoustic fields at the two holes. Although this parameter was expected to be small for the closely-spaced hole configuration, Keefe comments from his observations that the internal interactions have a more significant effect on the playing behaviour of woodwind instruments than the external interactions. As the centre-to-centre spacing of the closely spaced holes is approximately 1.5mm smaller than that observed on a Boehm flute (scaled relative to the tube and hole radii) and smaller than the relative centre-to-centre spacings used by Keefe when observing the acoustic streaming motion at tone holes, it is feasible that any internal interaction present is significant enough to change the streaming motion as observed.

Comparison between the streaming velocity contour maps and the graphs of pressure variation as a function of frequency for the two double-hole configurations indicate some correspondence between the relative pressure measured at the two holes and the generation of streaming outside the hole, with the motion clearly split into three regimes (as illustrated in figures 7.7 and 7.11). At frequencies in regime 1 (when the pressure in the lower hole is greater than that in the upper hole), the streaming motion at the lower hole is comparable with or larger than the streaming motion at the upper hole. In the case of the widely spaced holes, a strong upward jet is observed exiting out of the lower hole. However, for the more closely spaced holes, this jet is replaced by a more localised streaming motion which remains near the hole exit. In flow regime 2, when the pressure in the upper hole is greater than that at the lower hole, a strong jet is observed out of the upper hole directed back towards the loudspeaker whose strength increases

with increasing frequency. At the transition frequency between flow regimes 2 and 3 where the pressure is the same at both holes (688Hz and 684Hz for the widely-spaced and closely-spaced holes respectively), this jet is observed to abruptly disappear. However, in both cases, increasing the frequency further (flow regime 3) results in the jet reappearing, with the direction of the jet deviating from its downward direction upwards with increasing frequency. This upward deviation, which is only seen for frequencies above the higher resonance frequency, is similar to that observed for the case of the single hole with increasing frequency.

Although some similarities can be seen between the streaming behaviour of the single and double-hole configurations, the presence of a second hole clearly results in inter-hole interactions which significantly affect the streaming motion outside (and presumably inside) the tube. Hence, for the centre-to-centre hole spacings investigated, the multiple hole configurations can not be considered as a direct extension of an array of single side holes.

The effect of changing the intensity produced some interesting results. For the single hole, increasing the intensity at a fixed frequency resulted in the jet being deflected downwards. For the case of the two double-hole configurations, increasing the intensity levels resulted in observable interactions between the streaming motion at both holes, although this was seen to depend on frequency. A slightly higher intensity level was required to produce similar streaming velocities outside the closely-spaced hole configuration to those found for the widely-spaced configuration. This may be correlated with an increase in interhole interactions, which have been shown to significantly affect the playing behaviour of an instrument [58]. The onset of turbulent behaviour outside the double-hole tubes was found to occur around an intensity level (measured at the lower hole exit) of between

124 and 125dB. Comparison with the pressure levels measured at the tone holes of a Boehm flute (section 7.4) suggest that turbulent behaviour is found under normal playing conditions. However, even under these conditions, investigation of the pressure profile with radial distance inside the tube shows that the pressure field in the half of the tube opposite the side-hole is not significantly affected.

The results discussed above show that a significant streaming motion is observed outside the holes of a tube with a similar geometry to that of a simplified Boehm flute when excited by an acoustic source, whose behaviour is strongly dependent on factors including frequency, intensity and hole separation. However, it is not possible to ascertain from these results whether this streaming motion is significant enough to strongly affect the acoustic field at the side holes and therefore audibly change the sound produced. A detailed investigation of the simultaneous behaviour of the streaming motion and the acoustic field, whilst possible using the technique of PIV, is beyond the scope of this work.

7.8 Summary

This chapter started by reviewing current literature on the study of tone holes and discussing recent corrections to the theoretical model. Previous studies have shown that for the case of woodwind instruments, the acoustical behaviour of the instrument is strongly influenced by factors such as the position, geometry and separation of the tone holes along the main duct, which can significantly alter the timbre and playability of the instrument.

Preliminary pressure measurements were taken in the vicinity of a Boehm flute under normal playing conditions to establish the intensity levels present under realistic conditions. Using a simple experimental configuration comparable to that of a Boehm flute, the acoustic streaming motion in the vicinity of side holes was then examined using PIV. Three different side hole configurations were used to investigate the effects of frequency, sound intensity and spacing between side holes on the streaming behaviour.

A significant streaming motion was observed out of the side holes in each tube configuration, whose behaviour was found to strongly depend on the frequency and intensity level of excitation. The streaming behaviour for the single-hole configuration was observed to be relatively uncomplicated. However, the streaming motion observed for the double-hole configurations was much more complex; it was suggested that this could be due to internal interactions between the sound fields at the two holes.

Chapter 8

Conclusions

This final chapter presents a summary of the work. Conclusions from previous chapters are reviewed, and the extent to which the aims (as detailed in the section 1.1) were fulfilled is discussed in turn. Finally, suggestions for further work are outlined.

8.1 Suitability of PIV to the investigation of acoustic fields

The first aim detailed in the introduction was to verify the suitability of PIV in investigating both the oscillatory acoustic velocity, and the mean streaming motion resulting from interaction of the acoustic field with a solid boundary.

As discussed in chapter 1, PIV has been previously used to investigate acoustic fields. However, this work was limited to the use of conventional camera systems using wet film to record particle displacements [8, 45]. Given the introduction of a digital camera and analysis system, it was felt necessary to verify the suitability of the complete digital process to the measurement of acoustic fields. A number

of aspects were considered in verifying the suitability of the digital PIV system; these are discussed below.

The main advantage of a digital PIV system is the significantly faster image acquisition rate when compared to a conventional camera. For the study of acoustic fields, this provides the ability to take images at specific points within the acoustic cycle, as demonstrated in chapter 6, and the possibility of obtaining multiple images within one cycle. The use of a digital analysis system also allows easier quantification of further acoustic parameters such as vorticity, and identification of small-scale spatial structures.

A secondary benefit of this system is that it permits real-time viewing of the flow. This improves the efficiency of the initial alignment process and allows optimisation of variable experimental parameters. This is particularly invaluable when obtaining a large quantity of data, such as demonstrated in chapter 6, where it is important to identify problems before proceeding with the acquisition and analysis of a large number of images.

Despite the above advantages, the system is not exempt from some of the problems inherent in PIV. The most obvious of these are the problems associated with flow seeding. Firstly, it is important to have seeding which will provide an accurate representation of the fluid flow. Comparison of the measured response against theoretical predictions showed good representation, with acoustic velocities within 5% of that expected from pressure measurements at the end of the closed tube. However, certain limitations were found with both types of seeding used in this study (incense smoke and neutrally buoyant bubbles). Whilst the bubbles responded well below intensity levels of 151dB and with relatively low

intensity laser beams, above this level the bubbles burst, significantly reducing the particle concentration, and hence invalidating the method. The use of incense smoke was more successful for the full range of intensity fields investigated. However the streaming motion became significantly distorted when excessively high concentrations were present.

8.2 Measurement of non-linear effects in a closed tube

The first investigation of non-linear effects was in a simple closed-tube system. The second aim of this work was therefore to demonstrate that digital PIV is capable of measuring small scale non-linear effects induced by high-intensity sound fields in a closed tube, and to compare the measured behaviour with existing theoretical predictions.

It is clear from the results presented in chapter 5 that PIV is more than capable of capturing the small non-linear effects of interest to this study. The measurements showed that non-linear effects were seen with increasing intensity, with repeatable results. Comparison with existing theoretical predictions highlighted a number of interesting discrepancies.

While the shape of the toroidal vortices became increasingly distorted with higher sound intensity levels as predicted, the form of the distortion was somewhat different. Rather than the vortices being wider at the velocity anti-node and tapering at the node, the opposite behaviour was in fact observed, both with PIV and by physical observation.

Additional analysis showed that the component of axial streaming velocity deviated from sinusoidal dependence. Although this was as expected from the theoretical model, the direction of the deviation was again in the opposite direction to that predicted. In some respects, this was not surprising given the earlier observations of the streaming motion. Positions of the velocity maxima and minima deviated towards the velocity nodes rather than the anti-nodes. It was also observed that the position of the zero velocity points was such that the spacing was unequal. Due to the significant difference in displacements when compared to the predicted deviation, further direct comparison with theoretical predictions was difficult.

8.3 Investigation of acoustic behaviour at open-ended tube terminations

The third aim of this work was to examine the acoustic behaviour at tube terminations, and establish the non-linear effects present in this configuration.

Chapter 6 began by describing the development of a new technique to obtain the radiation impedance at the open end of the tube, using PIV in conjunction with pressure measurements. This technique was firstly validated in a closed tube, where the relationship between pressure and acoustic velocity was known, with a phase amplitude measured to within 2.5 degrees. This technique was then used to examine the acoustic behaviour at the termination of an open-ended tube.

Results confirmed that the acoustic resistance, which is constant in the linear regime, increases proportionally with exit velocity for high intensity fields. This

result verifies the introduction of non-linear effects with increasing intensity and concurs with work by other authors using alternative methods [9, 25, 51].

Further non-linear effects observed using this tube configuration included the formation of a jet and vortex shedding. The presence of a jet in the centre of the flow was confirmed by a steady flow component superimposed on the sinusoidally varying exit velocity signal. Further analysis of the velocity maps to examine vorticity showed the presence of vortex shedding in the vicinity of the tube exit.

The consequence of these effects on the acoustic field is thought to be a transfer of energy between the acoustic field and vortical motion. However, study of this effect is outside the scope of work considered here.

8.4 Qualitative examination of the streaming motion at side holes

The final aim of this study was to qualitatively examine the streaming motion at side holes under realistic playing conditions.

Using a configuration similar to that of a Boehm flute, the streaming motion out of side holes was investigated with the tube excited at resonance. Several different configurations were used to examine this non-linear effect as a function of frequency, intensity and side hole spacing.

For the single-hole configuration, the behaviour was relatively straightforward. The direction of the streaming motion was observed to deflect downstream with increasing frequency. However, for the two double hole configurations used

(closely and widely spaced holes), the streaming behaviour was far more complex. Although some similarities were drawn between the single and double hole configurations, it is clear that multiple side hole configurations can not be considered as an array of single side holes.

One of the most notable observations was that whilst streaming motion was seen at both side holes, around the resonance frequency, the predominant streaming motion was observed exiting the downstream of the two side holes. This is in conflict with previous observations [58] which found that the streaming motion exited primarily from the first tone hole.

Comparison between pressure measurements at the side holes and corresponding velocity maps with the pressure measured at tone holes of a real flute suggests that the streaming motion exhibits turbulent behaviour under playing conditions. However, it is difficult to draw conclusive comparisons with a flute under playing conditions as the excitation mechanism used was a forced oscillation (loudspeaker) rather than the jet excitation present in reality.

8.5 Further work

The work in this thesis could be extended in a number of ways. These can be divided into two areas: the improvement of experimental techniques, and the specific application to musical instruments.

8.5.1 Improvement of experimental techniques

It is clear from the preliminary investigation on microphone orientation in chapter 4 that the presence of a probe in the acoustic field, especially in high intensity conditions, significantly distorts the acoustic field around the vicinity of the probe. This has important implications for investigations where PIV measurements alone are not sufficient, such as the radiation impedance work presented in chapter 6. PIV could be used to determine the velocity non-intrusively in a field where the relationship between pressure and velocity is previously known. Subsequent measurements with a probe would then give an indication of the effect of the intrusion on the absolute pressure measurement.

As discussed in chapter 4, the versatility of the PIV systems used could be enhanced by incorporating a high-speed digital camera capable of up to 10,000 frames per second. This would allow the investigation of velocities within one acoustic cycle, yielding a more accurate instantaneous velocity where unstable velocity fields exist, such as those seen in chapter 5. In addition it would allow the examination of vorticity within one acoustic cycle; this may provide a better understanding of sound production and acoustic behaviour in musical instruments.

As noted in chapter 5, one of the fundamental problems with PIV is the effect of seeding particles on the streaming motion. Further investigations should be made to establish the optimum choice of seeding particle (beyond the two mediums used in this study), and appropriate concentration levels for PIV measurements of acoustic fields. In addition, the effect of unhomogenous seeding on the measurements needs to be better understood. It is suggested that this may be achieved through comparison with numerical modelling of the acoustic behaviour inside the closed-end tube situation using a technique such as Lattice Boltzmann simulations. This technique could also be applied to an investigation of the effect of sinusoidal input signals with a higher harmonic content.

8.5.2 Specific application to musical instruments

The most obvious extension of this study is the direct application to wind instruments where the behaviour of the acoustic field in the vicinity of tone holes and terminations is still uncertain. There are several areas where the current work can be extended towards realisation of this objective; each is discussed below.

The largest difference between the experimental configuration used in this study and a real situation is the excitation method. As discussed in chapter 7, it is difficult to draw comparisons with a wind instrument without using the same mechanism for exciting the air column. It is suggested that the forced oscillation provided by the loudspeaker in this study is replaced by a controlled air jet, possibly in conjunction with an artificial lip. Similar configurations have previously been used in the study of various woodwind and brass instruments [10, 23, 26].

It is well known that the geometry of a wind instrument has a significant effect on the sound produced. While the current experimental configuration is of a relatively simplistic nature, it would be interesting to examine the effect of more realistic exit and side-hole geometries. This could include undercutting of the side-holes and addition of a chimney.

As discussed in chapter 6, the energy associated with the interaction between vortical and acoustic fields has been correlated with the spectral distribution and hence the timbre of the sound produced [37]. Although preliminary calculations have been made, a number of problems have been identified and this requires further investigation to determine the feasibility of PIV in measuring this energy transfer.

It is clear from the work presented in this thesis that Particle Image Velocimetry has significant potential in the investigation of acoustic fields. It is hoped that the work described above will provide a sound basis for further study towards the aim of a full understanding of musical instruments.

Bibliography

[1] R.J. Adrian. Image shifting technique to resolve directional ambiguity in double-pulsed velocimetry. *Appl. Optics*, 25:3855–3858, 1986.

[2] R.J. Adrian. Particle-imaging techniques for experimental fluid mechanics. *Ann. Rev. Fluid Mech.*, 23:261–304, 1991.

[3] R.J. Adrian. Dynamic ranges of velocity and spatial resolution of particle image velocimetry. *Meas. Sci. Technol.*, 8:1393–1398, 1997.

[4] R.J. Adrian and C-S. Yao. Pulsed laser technique application to liquid and gaseous flows and the scattering power of seed materials. *Appl. Opt.*, 24:44–52, 1985.

[5] E.N.Da C. Andrade. On the circulations caused by the vibration of air in a tube. *Proc. R. Soc. London A*, 134:445–469, 1931.

[6] J.M. Andres and U. Ingard. Acoustic streaming at high reynolds numbers. *J. Acoust. Soc. Am.*, 25:928–932, 1953.

[7] J.M. Andres and U. Ingard. Acoustic streaming at low reynolds numbers. *J. Acoust. Soc. Am.*, 25:932–938, 1953.

[8] M.P. Arroyo and C.A. Greated. Stereoscopic particle image velocimetry. *Meas. Sci. Technol.*, 2:1181–1186, 1991.

[9] M. Atig. Non linéarités acoustiques localisées. exemple du rayonnement d'un tube. *D.E.A. report, Académie de Nantes, Université du Maine*, 2001.

[10] J. Backus. Vibrations of the reed and air column in the clarinet. *J. Acoust. Soc. Am.*, 33:806–809, 1961.

[11] D.W. Bechert. Sound absorption caused by vorticity shedding demonstrated with a jet flow. *J. Sound Vib.*, 70:389–405, 1980.

[12] A.H. Benade. On the mathematical theory of woodwind finger holes. *J. Acoust. Soc. Am.*, 32:1591–1609, 1960.

[13] A.H. Benade. On the propagation of sound waves in a cylindrical conduit. *J. Acoust. Soc. Am.*, 44(2):616–623, 1968.

[14] A.H. Benade and J.S. Murday. Measured end corrections for woodwind toneholes. *J. Acoust. Soc. Am.*, 41:1609–1610, 1967.

[15] T. Boehm. *The flute and flute-playing.* 1871, Reprint by Dover, New York, 1964.

[16] Brüel and Kjær. *Condenser microphones and microphone preamplifiers for acoustic measurements.* Denmark, 1982.

[17] D.M. Campbell, J.A. Cosgrove, C.A. Greated, S. Jack, and D. Rockliff. Review of lda and piv applied to the measurement of sound and acoustic streaming. *Opt. Laser Technol.*, 32:629–639, 2000.

[18] D.M. Campbell and C.A. Greated. *The Musician's Guide to Acoustics.* Dent, London, 1987.

[19] Z. Carrière. Analyse ultramicroscopique des vibrations aeriennes [ultramicroscopic analysis of air vibration]. *J. phys. et radium*, 10:198, 1929.

[20] Y.S. Cheng, W.E. Bechtold, C.C. Yu, and I.F. Hung. Incense smoke: characterization and dynamics in indoor environments. *Aerosol Sci. Technol.*, 23:271–281, 1995.

[21] J.Y. Chung and D.A. Blaser. Transfer function method of measuring induct acoustic properties. i. theory. *J. Acoust. Soc. Am.*, 68:907–913, 1980.

[22] J.W. Coltman. Acoustical analysis of the boehm flute. *J. Acoust. Soc. Am.*, 65:499–506, 1979.

[23] J.S. Cullen. *A study of brass instrument acoustics using an artificial lip reed mechanism, laser doppler anemometry and other techniques.* PhD thesis, University of Edinburgh, 2000.

[24] A. Cummings and W. Eversman. High amplitude acoustic transmission through duct terminations: theory. *J. Sound Vib.*, 91:503–518, 1983.

[25] J.-P. Dalmont, C.J. Nederveen, V. Dubos, S. Ollivier, V. Méserette, and E. te Sligte. Experimental determination of the equivalent circuit of an open side hole: linear and non linear behaviour. *Acustica*, 88:567–577, 2002.

[26] J.P. Dalmont, B. Gazengel, J. Gilbert, and J. Kergomard. Some aspects of tuning and clean intonation in reed instruments. *Appl. Acoustics*, 46:19–60, 1995.

[27] T. Dewhirst. *Multiple CCD Array Digital Particle Image Velocimetry.* PhD thesis, University of Edinburgh, 1998.

[28] J.H.M. Disselhorst and L. van Wijngaarden. Flow in the exit of open pipes during acoustic resonance. *J. Fluid Mech.*, 99:293–319, 1980.

[29] V. Dubos, J. Kergomard, A. Khettabi, J.-P.Dalmont, D.H. Keefe, and C.J. Nederveen. Theory of sound propagation in a duct with a branched tube using modal decomposition. *Acustica*, 85:153–169, 1999.

[30] P.W. Duck and F.T. Smith. Steady streaming induced between oscillating cylinders. *J. Fluid Mech.*, 91:93–110, 1979.

[31] S. Duffourd, D. Marx, and P. Blanc-Benon. Détermination de la vitesse acoustique instantanée par piv dans un stack thermoacoustique. In *Proc. 6th French Conference on Acoustics* , Lille, France, pages 535–538, 2002.

[32] F. Durst, A. Melling, and J.H. Whitelaw. *Principles and practice of laser-doppler anemometry.* Academic Press, 1976.

[33] C. Eckart. Vortices and streams caused by sound waves. *Phys. Rev.*, 73(1):68–76, 1948.

[34] I. Grant (editor). *Selected Papers on Particle Image Velocimetry.* SPIE Optical Engineering Press (Milestone Series), 1994.

[35] N. Emarat. *Particle Image Velocimetry experiments on surf-zone breaking waves.* PhD thesis, University of Edinburgh, 2000.

[36] J.D. Entwistle. *Digital particle image velocimetry applied to a flow through a duct.* PhD thesis, The University of Edinburgh, 1999.

[37] B. Fabre, A. Hirschberg, and A.P.J. Wijnands. Vortex shedding in steady oscillations of a flue organ pipe. *Acustica*, 82:863–877, 1996.

[38] F.J. Fahy. Measurement of acoustic intensity using the cross-spectral density of two microphone signals. *J. Acoust. Soc. Am.*, 62:1057–1059, 1977.

[39] M. Faraday. On a peculiar class of acoustical figures; and on certain forms assumed by groups of particles upon vibrating elastic surfaces. *Philos. Trans.*, 121:299–340, 1831.

[40] N.H. Fletcher and T.D. Rossing. *The Physics of Musical Instruments.* Springer-Verlag, 1991.

[41] J. Gilbert and L. Menguy. *Private Communication.* L'Université du Maine, 2001.

[42] C. Gray, C.A. Greated, D.R. McCluskey, and W.J. Easson. An analysis of the scanning beam piv illumination system. *Meas. Sci. Technol.*, 2:717–724, 1991.

[43] V.E. Gusev and O.V. Rudenko. Nonsteady quasi-one-dimensional acoustic streaming in unbounded volumes with hydrodynamic nonlinearity. *Sov. Phys. Acoust.*, 25:493–497, 1979.

[44] V.E. Gusev and O.V. Rudenko. Evolution of nonlinear two-dimensional acoustic streaming in the field of a highly attenuated sound beam. *Sov. Phys. Acoust.*, 27:481–484, 1981.

[45] D.B. Hann. *Simultaneous measurement of acoustic fields and flow fields using optical methods.* PhD thesis, The University of Edinburgh, 1995.

[46] D.B. Hann and C.A. Greated. Measurement of acoustic particle velocity using particle image velocimetry. *Acustica*, 83:354–358, 1997.

[47] D.B. Hann and C.A. Greated. The measurement of flow velocity and acoustic particle velocity using particle-image velocimetry. *Meas. Sci. Technol.*, 8:1517–1522, 1997.

[48] T.R. Haydon. *Turbulence and vorticity generated by breaking waves.* PhD thesis, The University of Edinburgh, 1998.

[49] K.D. Hinsch. Three-dimensional particle velocimetry. *Meas. Sci. Technol.*, 6:742–753, 1995.

[50] A. Hirschberg, J. Gilbert, R. Msallam, and A.P.J. Wijnands. Shock waves in trombones. *J. Acoust. Soc. Am.*, 99:1754–1758, 1996.

[51] U. Ingard and H. Ising. Acoustic nonlinearity of an orifice. *J. Acoust. Soc. Am.*, 42:6–17, 1967.

[52] U. Ingard and S. Labate. Acoustic circulation effects and the nonlinear impedance of orifices. *J. Acoust. Soc. Am.*, 22:211–218, 1950.

[53] JEM smoke machine Co. Ltd. *Hydrosonic 2000 Instruction Manual.*

[54] R.D. Keane and R.J. Adrian. Optimization of particle image velocimeters part 1:double pulsed systems. *Meas. Sci. Technol.*, 1:1202–1215, 1990.

[55] R.D. Keane and R.J. Adrian. Theory of cross-correlation of piv images. *Appl. Sci. Res.*, 49:191–215, 1992.

[56] D.H. Keefe. Experiments on the single woodwind tone hole. *J. Acoust. Soc. Am.*, 72:688–699, 1982.

[57] D.H. Keefe. Theory of the single woodwind tone hole. *J. Acoust. Soc. Am.*, 72:676–687, 1982.

[58] D.H. Keefe. Acoustic streaming, dimensional analysis of nonlinearities, and tone hole mutual interactions in woodwinds. *J. Acoust. Soc. Am.*, 73:1804–1820, 1983.

[59] C.H. Keith and J.C. Derrick. Measurement of the particle size distribution and concentration of cigarette smoke by the "conifuge". *Journal of Colloid Science*, 15:340–356, 1960.

[60] L.E Kinsler, A.R. Frey, A.B. Coppens, and J.V. Sanders. *Fundamentals of Acoustics.* John Wiley & Sons, 3rd Edition, 1982.

[61] W. Lauterborn and A. Vogel. Modern optical techniques in fluid mechanics. *Ann. Rev. Fluid Mech.*, 16:223–244, 1984.

[62] H. Levine and J. Schwinger. On the radiation of sound from an unflanged circular pipe. *Phys. Rev.*, 73:383–406, 1948.

[63] L.N. Liebermann. The second viscosity of liquids. *Phys. Rev.*, 75(9):1415–1422, 1949.

[64] J. Lighthill. Acoustic streaming. *J. Sound Vib.*, 61(3):391–418, 1978.

[65] J.J. Markham. Second-order acoustic fields: streaming with viscosity and relaxation. *Phys. Rev.*, 86(4):497–502, 1952.

[66] H. Medwin. An acoustic streaming experiment in gases. *J. Acoust. Soc. Am.*, 26:332–341, 1953.

[67] A. Melling. Tracer particles and seeding for particle image velocimetry. *Meas. Sci. Technol.*, 8:1406–1416, 1997.

[68] L. Menguy. *Propagation acoustique non lineaire dans les guides monodimensionnels.* PhD thesis, L'Université du Maine, 2001.

[69] L. Menguy and J. Gilbert. Non-linear acoustic streaming accompanying a plane stationary wave in a guide. *Acustica*, 86:249–259, 2000.

[70] E. Meyer and E-G. Neumann. *Physical and applied acoustics.* Academic Press, New York, 1972.

[71] C.J. Nederveen. Resonance frequency of a gas in a tube with a short closed side-tube. *Acustica*, 13:65–70, 1963.

[72] C.J. Nederveen. *Acoustical aspects of woodwind instruments.* 2nd edition, Northern Illinois University Press, DeKalb, Illinois, 1998.

[73] C.J. Nederveen, J.K.M. Jansen, and R.R. van Hassel. Corrections for woodwind tone-hole corrections. *Acustica*, 84:957–966, 1998.

[74] J.I. Nogueira, A. Lecuona, P.A. Rodriguez, and U. Ruiz-Rivas. On the design of some PIV postprocessing filters. In *Proc. 7th Int. Conf. in Laser Anemometry Advances and Applications,* pages 483-490, Karlsruhe, Germany, 1997.

[75] Y. Nomura, I. Yamamura, and S. Inawashiro. On the acoustic radiation from a flanged circular pipe. *J. Phys. Soc. Japan*, 15:510–517, 1960.

[76] W.L. Nyborg. Acoustic streaming due to attenuated plane waves. *J. Acoust. Soc. Am.*, 25(1):68–75, 1953.

[77] W.L. Nyborg. *Physical Acoustics, Acoustic Streaming. W.P. Mason (ed.).* Academic Press, New York, 1965, Vol. II, part B, 265-331.

[78] M.C.A.M. Peters and A. Hirschberg. Acoustically induced periodic vortex shedding at sharp edged open channel ends: simple vortex models. *J. Sound Vib.*, 161:281–299, 1991.

[79] M.C.A.M. Peters, A. Hirschberg, A.J. Reinen, and A.P.J. Wijnands. Damping and reflection coefficient measurements for an open pipe at low mach and low helmholtz numbers. *J. Fluid. Mech.*, 256:499–534, 1993.

[80] R.L. Pratt, S.J. Elliott, and J.M. Bowsher. The measurement of the acoustic impedance of brass instruments. *Acustica*, 38:236–246, 1977.

[81] Q. Qi. The effect of compressibility on acoustic streaming near a rigid boundary for a plane travelling wave. *J. Acoust. Soc. Am.*, 94:1090–1098, 1993.

[82] Q. Qi, R.E. Johnston, and J.G. Harris. Boundary layer attenuation and acoustic streaming accompanying plane-wave propagation in a tube. *J. Acoust. Soc. Am.*, 97:1499–1509, 1995.

[83] M. Raffel, C. Willert, and J. Kompenhans. *Particle Image Velocimetry; A Practical Guide.* Springer, 1998.

[84] C.G. Rasmussen. An experimental investigation of the diffraction correction for a rayleigh-disc. *Acustica*, 14:148–156, 1964.

[85] J.W.S. Rayleigh. On the circulation of air observed in kundt's tubes and some allied acoustical problems. *Philos. Trans. R. Soc. London*, 75:1–21, 1883.

[86] J.W.S. Rayleigh. *The theory of sound : Vol. 2.* Dover Publications, 2nd edition, New York, 1896.

[87] N. Riley. Streaming from a cylinder due to an acoustic source. *J. Fluid Mech.*, 180:319–326, 1987.

[88] O.V. Rudenko and S.I. Soluyan. *Theoretical foundations of non-linear acoustics. English translation.* Plenum, New York, 1977.

[89] H. Schlichting. Berechnung ebener periodischer grenzschichtströmmungen [calculation of plane periodic boundary layer streaming]. *Phys. Zeit.*, 33:327–335, 1932.

[90] T. Schlicke. *Breaking waves and the dispersion of surface films.* PhD thesis, The University of Edinburgh, 2001.

[91] J.P. Sharpe, C.A. Greated, C. Gray, and D.M. Campbell. The measurement of acoustic streaming using particle image velocimetry. *Acustica*, 68:168–172, 1989.

[92] L.J. Sivian. Acoustic impedance of small orifices. *J. Acoust. Soc. Am.*, 7:94–101, 1935.

[93] M. Stanislas and J.C. Monnier. Practical aspects of image recording in particle image velocimetry. *Meas. Sci. Technol.*, 8:1417–1426, 1997.

[94] P. Stansell. *The lattice gas technique applied to acoustic streaming.* PhD thesis, The University of Edinburgh, 1995.

[95] J.T. Stuart. Double boundary layers in oscillatory viscous flow. *J. Fluid. Mech.*, 24:673–687, 1966.

[96] S. Tjøtta. On some non-linear effects in sound fields, with special emphasis on the generation of vorticity and the formation of streaming patterns.

part ii. streaming caused by a sound beam. *Archiv for Mathematik og Naturvidenskab*, LV:36–68, 1959.

[97] D.L. Tritton. *Physical Fluid Dynamics.* Oxford Science Publications, 2nd edition, 1988.

[98] J.C. Valière, P. Herzog, V. Valeau, and G. Tournois. Acoustic velocity measurements in air by means of laser doppler velocimetry: dynamic and frequency range limitations and signal processing improvements. *J. Sound Vib.*, 229:607–626, 2000.

[99] H.C. van de Hulst. *Light Scattering by Small Particles.* Dover, 1957.

[100] F.J.M. van der Eerden, H-E. de Bree, and H. Tijdemann. Experiments with a new acoustic particle velocity sensor in an impedance tube. *Sensors and actuators*, 69:126–133, 1998.

[101] J.F. Vignola, Y.H. Berthelot, S. Jones, and J. Jarzynski. Equation of motion of microparticles in suspension in an insonified medium. *J. Acoust. Soc. Am.*, 1:332–334, 1992.

[102] G.D. West. Circulation occurring in acoustic phenomena. *Proc. Phys. Soc. (London)*, 64:483, 1951.

[103] P.J. Westervelt. The theory of steady rotational flow generated by a sound field. *J. Acoust. Soc. Am.*, 25(1):60–67, 1953.

[104] J. Westerweel. *Digital Particle Image Velocimetry.* Delft University Press, 1993.

[105] J. Westerweel. Efficient detection of spurious vectors in particle velocimetry data. *Experiments in Fluids*, 16:236–247, 1994.

[106] J. Westerweel. Fundamentals of digital particle image velocimetry. *Meas. Sci. Technol.*, 8:1379–1392, 1997.

[107] J. Westerweel, D. Dabiri, and M. Gharib. The effect of a discrete window offset on the accuracy of cross-correlation analysis of digital piv recordings. *Experiments in Fluids.*, 23:20–28, 1997.

[108] C.E. Willert and M. Gharib. Digital particle image velocimetry. *Experiments in Fluids*, 10:181–193, 1991.

[109] L.K. Zarembo. *High-Intensity Ultrasonic Fields part III, ed. L.D.Rozenberg.* Plenum Press, New York, 1971, 135-199.

Publications

Conference Papers

D. Rockliff, D.M. Campbell, C.A. Greated. PIV experimental study on acoustic streaming in cylindrical air-filled tubes using high intensity sound fields. In *Proc. 5th CFA 2000*, pages 199-202, Lausanne, Switzerland, September 2000.

D. Rockliff, D.M. Campbell, C.A. Greated. PIV experimental study on acoustical streaming in cylindrical air-filled tubes using high intensity sound fields. In *Proc. ICSV7*, Garmisch-Partenkirchen, Germany, July 2000.

D. Rockliff, C.A. Greated. Application of PIV to the measurement of acoustic fields in woodwind instruments. In *Proc. ISMA 2001*, pages 399-402, Perugia, Italy, September 2001.

D. Rockliff, J.-P. Dalmont, D.M. Campbell. Experimental study of the velocity field at the side holes and termination of a tube. In *Proc. ICA 2001*, page 24, Rome, Italy, September 2001.

D. Rockliff, D.J. Skulina, D.M. Campbell, C.A. Greated. PIV measurement of acoustic velocities at woodwind instrument toneholes. In *Proc. IOA 2002*, Salford, UK, March 2002. (CD-ROM only)

Journal Papers

M. Campbell, J.A. Cosgrove, C.A. Greated, S. Jack and D. Rockliff. Review of LDA and PIV applied to the measurement of sound and acoustic streaming. *Optics and Laser Technology*, 32:630-639, 2000.